Investigation of Magnetohydrodynamic Fluctuation Modes in the STOR-M Tokamak

A Thesis Submitted to the College of

Graduate Studies and Research

In Partial Fulfillment of the Requirements

For Master of Science

In the Department of Physics and Engineering Physics

University of Saskatchewan

Saskatoon

By

Sayf Gamudi Elgriw

Permission to Use

In presenting this thesis in partial fulfilment of the requirements for a Postgraduate degree from the University of Saskatchewan, I agree that the Libraries of this University may make it freely available for inspection. I further agree that permission for copying of this thesis in any manner, in whole or in part, for scholarly purposes may be granted by the professor or professors who supervised my thesis work or, in their absence, by the Head of the Department or the Dean of the College in which my thesis work was done. It is understood that any copying or publication or use of this thesis or parts thereof for financial gain shall not be allowed without my written permission. It is also understood that due recognition shall be given to me and to the University of Saskatchewan in any scholarly use which may be made of any material in my thesis.

Requests for permission to copy or to make other use of material in this thesis in whole or part should be addressed to:

Head of the Department of Physics and Engineering Physics

116 Science Place

University of Saskatchewan

Saskatoon, Saskatchewan

S7N 5E2

Dedicated to my parents

Abstract

While magnetohydrodynamic (MHD) instabilities are considered one of the intriguing topics in tokamak physics, a feasibility study was conducted in the Saskatchewan Torus-Modified (STOR-M) tokamak to investigate the global MHD activities during the normal (L-mode) and improved (H-mode) confinement regimes. The experimental setup consists of 32 discrete Mirnov coils arranged into four poloidal arrays and mounted on STOR-M at even toroidal distances. The perturbed magnetic field fluctuations during STOR-M discharges were acquired and processed by the Fourier transform (FT), the wavelet analysis and the singular value decomposition (SVD) techniques. In L-mode discharges, the poloidal MHD mode numbers varied from 2 to 4 with peak frequencies in the range $20 \sim 40$ kHz. The dominant toroidal modes were reported between 1 and 2 oscillating at frequencies $15 \sim 35$ kHz. In another experiment, a noticeable MHD suppression was observed during the H-mode-like phase induced by the compact torus (CT) injection into STOR-M. However, a burst-like mode called the gong mode was triggered prior to the H-L transition, followed by coherent Mirnov oscillations. Mirnov oscillations with strong amplitude modulations were observed in the STOR-M tokamak. Correlations between Mirnov signals and soft x-ray (SXR) signals were found.

Acknowledgements

First and foremost, I would like to express my deepest gratitude to my supervisor Prof. Chijin Xiao for enlightening me with his remarkable guidance and support during my research. I would also like to thank Prof. Akira Hirose, the director of Plasma Physics Laboratory, for permitting me to use the STOR-M tokamak in this research project. A special note of thanks is made to Prof. D. Raju from the ADITYA tokamak for his insightful comments about the singular value decomposition algorithm. The technical assistance provided by David McColl and the Physics Machine Shop is greatly appreciated. Also, I am really in debt to Dr. Mykola Dreval for many valuable thoughts and discussions. Lastly, but not least, I would like to acknowledge my fellow graduate students Kurt Kreuger, Dallas Trembach, Andre Pant and Damian Rohraff for their endless help and friendship.

This research was supported by the grants from the Natural Sciences and Engineering Research Council of Canada (NSERC), Canada Research Chair (CRC) Program and through financial aid from the University of Saskatchewan Graduate Scholarship.

Table of Contents

List of Tables

List of Figures

List of Abbreviations and Symbols

Abbreviation	Definition
AC	Alternating Current
CT	Compact Torus
CWT	Continuous Wavelet Transform
DAS	Data Acquisition System
DFT	Discrete Fourier Transform
ECE	Electron Cyclotron Emission
FB	Feedback
FCC	Fourier Cross-Correlation
FCD	Fourier Coefficient Decomposition
FFT	Fast Fourier Transform
FT	Fourier Transform
H-Mode	Improved Confinement Discharge
IDFT	Inverse Discrete Fourier Transform
JET	Joint European Torus
L-Mode	Normal Confinement Discharge
MATLAB	Matrix Laboratory
MHD	Magnetohydrodynamic
OH	Ohmic Heating
PA	Principal Axis
PC	Principal Component
RF	Radio Frequency
SOL	Scrape-Off Layer
STFT	Short-Time Fourier Transform
STOR-M	Saskatchewan Torus-Modified
STOR-1M	Saskatchewan Torus-1 Modified
SV	Singular Value
SVD	Singular Value Decomposition

SXR	Soft X-Ray
TH	Turbulent Heating
USCTI	University of Saskatchewan Compact Torus Injector
VE	Vertical Equilibrium
WT	Wavelet Transform

Symbol	**Definition**
a	Minor radius
A	Cross-section
B	Magnetic field
B_r	Radial magnetic field
B_z	Axial magnetic field
$B_\perp$	Vertical magnetic field
B_θ	Poloidal magnetic field
B_ϕ	Toroidal magnetic field
c	Speed of light
C	Capacitance
C_m	Fourier cosine coefficient
d	Thickness
D	Deuterium
e	Elementary charge
e_r	Radial unit vector
e_θ	Azimuthal unit vector
E	Electric field
f	Frequency
f_b	Wavelet variance parameter
f_c	Wavelet central frequency
f_m	Frequency of poloidal mode m
f_n	Frequency of toroidal mode n
F	Force
H_α	Radiation intensity
I	Current
I_p	Plasma current
J	Current density
J_z	Axial current density
J_θ	Azimuthal current density

l_i	Internal inductance
$\ln \Lambda$	Coulomb logarithm
L	Inductance
L_p	Plasma inductance
m	Poloidal mode number
M	Number of samples
n	Toroidal mode number
n_e	Electron density
n_i	Ion density
N	Number of channels
p	Pressure
p_e	Electron pressure
p_i	Ion pressure
P	Power per unit volume
q	Safety factor
Q	Kinetic energy
r	Radial coordinate
r_L	Larmor radius
R	Major radius
R_c	Radius of magnetic field curvature
R_p	Plasma resistance
$\Re$	Collisional transfer of momentum
s	Wavelet scale
S_m	Fourier sine coefficient
t	Time
t_s	Sampling time
T_e	Electron temperature
T_i	Ion temperature
T	Tritium
v	Velocity
v_e	Electron velocity
v_i	Ion velocity
V	Voltage
V_f	Floating potential
V_p	Loop voltage
w	Window function

W	Potential energy
x	Signal
X	Reactance
X_C	Capacitive reactance
X_L	Inductive reactance
z	Axial coordinate
Z	Impedance
Z_{eff}	Effective ion charge number
$\parallel$	Parallel to magnetic field direction
$\perp$	Perpendicular to magnetic field direction
∇	Gradient operator
β_θ	Poloidal beta factor
γ	Coherence factor
Γ	Phase operator
δ	Skin depth
Δ	Shafranov parameter
ΔH	Horizontal plasma position
ϵ	Inverse aspect ratio
ε	Permittivity
η	Resistivity
θ	Azimuthal coordinate
ι	Rotational transform angle
λ_D	Debye length
μ	Permeability
ν	Collision frequency
ξ	Arbitrary displacement
ρ	Mass density
σ	Conductivity
τ	Wavelet translation
τ_E	Energy confinement time
ϕ	Toroidal coordinate
$\hat{\phi}$	Phase corrector
Φ	Magnetic flux
ψ	Wavelet function
$\hat{\psi}$	Fourier transform of wavelet function ψ
ω	Angular frequency

Chapter 1

Introduction

1.1 Energy Demand

Energy has played a major role in the development of human civilization. Energy is a vital component to sustain the industrial countries as well as to improve the economical condition of less-developed nations. A nation's energy consumption reflects industrial activity, food production, transportation, heating and cooling buildings and production of electricity. Despite this fact, the world nowadays is going through an energy crisis and likely the situation will get even worse due to the high consumption of natural energy resources. The high energy demand arises from the increased usage in the major industrialized areas of the world led by North America, Europe and Japan. Also, some rapidly industrializing nations such as China and India have increased the global consumption of energy. Some statistical studies stated that the future energy consumption will at the very least be double the present global usage.

The dilemma of an economically feasible and environmentally friendly energy resource has not yet been resolved. Some scientific studies stress on the fact that the emission of greenhouse gases is starting to have a noticeably negative impact on the environment. If the emission of greenhouse gases has to be somehow reduced in the future, this would limit the amount of energy generated from the conventional fossil fuels like coal, natural gas and oil. A further complication is that all the natural reserve of oil and natural gas will be exhausted in the near future. Nuclear power may

seem the best solution available for large-scale energy generation, however disposing of radioactive waste and the threat of nuclear proliferation compelled the politicians and scientists to look somewhere else for a global energy solution. Figure 1.1 shows the composition of the energy sources as extracted in 2007 [1]. The political and scientific communities are trying to constrain greenhouse emissions and nuclear wastes to a safe level [2].

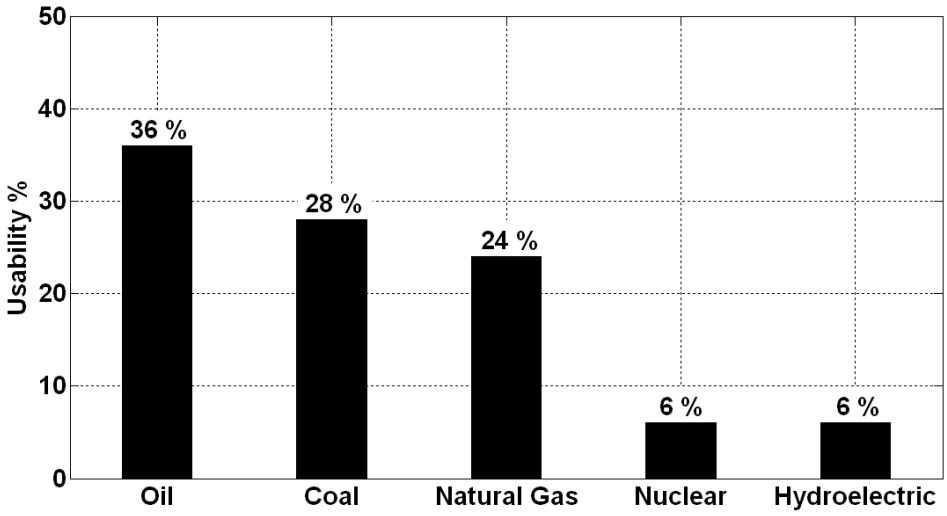

Figure 1.1: The world primary energy consumption per fuel type in 2007 [1].

To maintain the balance between the increase of energy supply and the decrease of pollution level, fusion energy has been proposed as a promising candidate for the existing energy options. It has many attractive features in terms of safety, abundance of fuel, and minimal impact on nature. Moreover, fusion has the potential to provide tremendous amount of electrical power which gives this technology a credit to be a major supplier of global energy. However, numerous technical and scientific difficulties must be subsided before promoting fusion technology for the commercial use. Therefore, the fusion research program is dedicated for resolving these problems which will be carried out for a relatively long time (i.e. 30-100 years). Table 1.1 lists energy reserves of some primary fuels. The table clearly indicates that the reserve of the fusion energy is practically unlimited. However, in the meantime, the global energy will still be majorally provided by natural fossil fuels [3].

Resource	**Energy Reserve** ($\times 10^9$ Joules)	**Availability** (years)
Coal	10^{14}	300
Oil	1.2×10^{13}	40
Natural Gas	1.4×10^{13}	50
U^{235} (Fission Reactors)	10^{13}	30
U^{238}, Th^{232} (Breeder Reactors)	10^{16}	30,000
Lithium (D-T Fusion Reactors):		
On Land	10^{16}	30,000
In Oceans	10^{19}	3×10^7

Table 1.1: Energy reserves of some primary fuels [4].

1.2 Fusion Energy

When two light atomic nuclei fuse to form heavier ones, the sum of the masses of nuclei after the fusion reaction is smaller than the sum before the reaction by Δm. According to the relativity theory, the amount of energy Δmc^2 (c is the speed of light) is released by the fusion reaction. The following fundamental nuclear reactions may be used as a source of fusion energy [5]:

$$\begin{aligned}
&\mathrm{D} + \mathrm{D} \rightarrow \mathrm{T}\ (1.01\ \mathrm{MeV}) + p\ (3.03\ \mathrm{MeV}) \\
&\mathrm{D} + \mathrm{D} \rightarrow \mathrm{He}^3\ (0.82\ \mathrm{MeV}) + n\ (2.45\ \mathrm{MeV}) \\
&\mathrm{T} + \mathrm{D} \rightarrow \mathrm{He}^4\ (3.52\ \mathrm{MeV}) + n\ (14.06\ \mathrm{MeV}) \\
&\mathrm{D} + \mathrm{He}^3 \rightarrow \mathrm{He}^4\ (3.67\ \mathrm{MeV}) + p\ (14.67\ \mathrm{MeV})
\end{aligned} \tag{1.1}$$

where D is deuterium, T is tritium, p is proton, He is helium and n is neutron. Although the D-D reaction seems more desirable due to the abundant supply of deuterium (0.015% of hydrogen in seawater $\approx 1.35 \times 10^9$ km^3), the D-T reaction with a large fusion probability at a lower temperature is easier to realize. Since the energy released by the chemical reaction of $H_2 + \frac{1}{2}O_2 \rightarrow H_2O$ is about 2.96 eV, the energy released by the fusion reaction exceeds the chemical reaction by one million times. The binding energy per nucleon is much smaller in very light nuclides compared to the

binding energy of nuclides with atomic mass number around 60. For this reason, a tremendous amount of energy can be released when the light nuclei are fused.

Although the first fusion explosion was successfully released from a hydrogen bomb in 1951, the controlled fusion research itself is still in development. The first attempt to control fusion reactions was conducted using energetic proton and deuterium beams which collide with a light nucleus. The beams lose their energy by the ionization process or elastic collisions and the probability of nuclear fusion is cutoff to a negligible degree. In fully ionized hydrogen, deuterium and tritium plasmas, the ionization process does not occur. If the plasma is confined adiabatically, the elastic collisions will have a minimal effect on the average energy. Using this approach, the hot D-T and D-D plasmas have to be well confined so that ions can reach higher velocities to overcome their mutual Coulomb repulsion forces and initiate fusion reactions.

The occurrence of a fusion reaction depends on the cross-section of the target nucleus which is denoted by σ. For a D-T reaction, the probability of the D nucleus to make a successful collision with the T nucleus is a function of the kinetic energy (Q) of D. The cross-section of the D-T reaction at $Q = 100$ keV is about 5×10^{-28} m^2. The probability of a fusion reaction per unit time in case the D nucleus has a velocity v and collides with the T nuclei with density of n_{T} is given by $n_{\mathrm{T}}\sigma v$. When the plasma has a Maxwellian ion temperature distribution T_i, it is important to average σv over the velocity distribution. The fitting equation of $\langle\sigma v\rangle$, in the unit of m^3/s, for a D-T reaction as a function of T_i (keV) is given by [6]:

$$\langle\sigma v\rangle = \frac{3.7 \times 10^{-18}}{\left(\frac{T_i}{37} + \frac{5.45}{3+T_i(1+\frac{T_i}{37.5})^{2.8}}\right) T_i^{\frac{2}{3}}} e^{\left(-\frac{20}{T_i^{\frac{1}{3}}}\right)} \tag{1.2}$$

Figure 1.2 depicts the relationship between the averaged fusion rate $\langle\sigma v\rangle$ and ion temperature T_i. The diagram indicates that the fusion rate becomes appreciably large when T_i reaches 10 keV and reaches a peak value at about 80 keV. Fuels at such high temperatures are ionized and therefore are called plasmas.

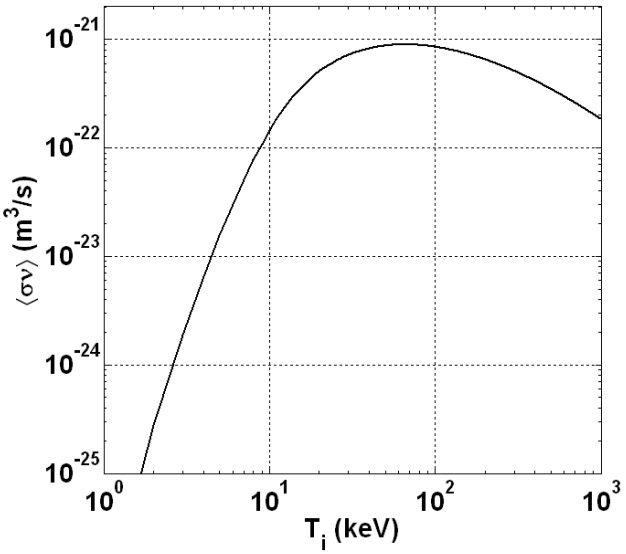

Figure 1.2: The dependence of the fusion reaction rate $\langle \sigma v \rangle$ on the ion temperature T_i for a D-T reaction.

1.3 Fusion Power Plant

In order to utilize any fusion reactor for commercial use, the gain of net output fusion power has to be larger than the total input power used to heat and to confine the fuel in the reactor. Figure 1.3 shows an example of an electric plant powered by a D-T fusion reactor. The 14 MeV fast neutrons produced by fusion reactions in the hot plasma penetrate the first wall. The fast neutrons are moderated by a lithium blanket surrounding the plasma which converts the kinetic energy of the neutrons to heat. The tritium is bred in the lithium blanket through the following reactions [7]:

$$\begin{aligned} \mathrm{Li}^6 + n &\rightarrow \mathrm{T} + \mathrm{He}^4 + 4.8\ \mathrm{MeV} \\ \mathrm{Li}^7 + n\ (2.5\ \mathrm{MeV}) &\rightarrow \mathrm{T} + \mathrm{He}^4 + n \end{aligned} \tag{1.3}$$

The lithium blanket passes the heat to a heat exchanger which converts the coolant into steam that is required for generating electric power. The electric power is generated using a conventional turbine connected to generator. A portion of the generated electric power is used for operating the heating system for the reactor. Alpha particles or He ions also contribute to the plasma heating process through Coulomb collisions. The total heating power P_{heat} is the sum of the alpha particles heating

power P_α and the external heating power system P_{ext}. The necessary net heating power to maintain the plasma in steady state operation must be equal to the loss of energy in the fusion reactor. In addition, plasma has to be confined long enough so a significant fraction of fuel undergoes fusion before escaping the reactor. The duration of energy confined in plasma is gauged by the total energy confinement time τ_E which is defined by [8]:

$$\tau_E = \frac{\frac{3}{2}n(T_e + T_i)}{P_L + P_R} \simeq \frac{3nT}{P_L + P_R} \tag{1.4}$$

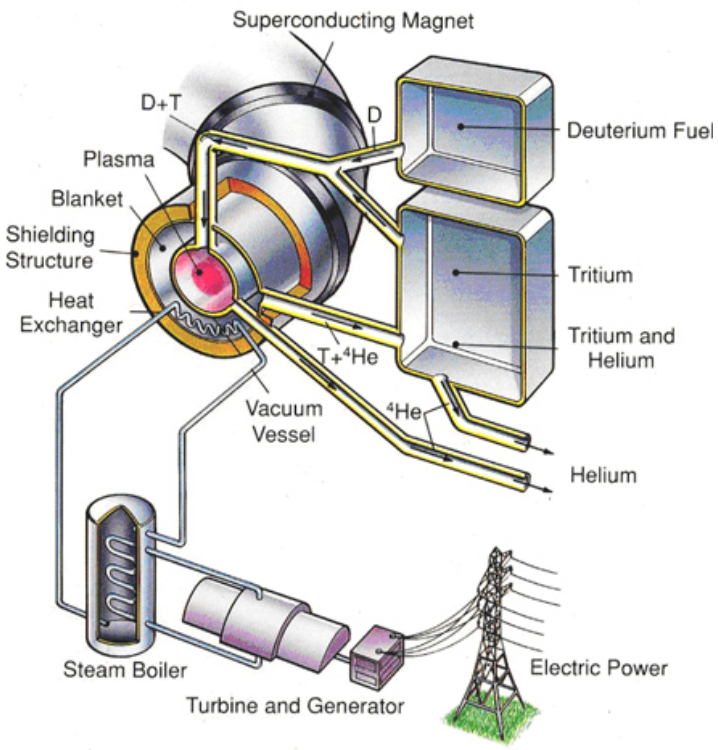

Figure 1.3: A schematic sketch of a fusion power plant [9].

where the thermal energy of plasma per unit volume is given by $\frac{3}{2}n(T_e + T_i)$. The transport of this thermal energy is dominated by convective losses and thermal conduction. The term P_L denotes the total power loss in the plasma per unit volume. Another important power loss is P_R which denotes the radiation loss due to bremsstrahlung of electrons and impurities in the plasma. The required heating input power P_{heat} to sustain the thermal energy of the plasma must be equal to $P_L + P_R$. In D-T reactions, the sum of kinetic energies $Q_\alpha = 3.52$ MeV of alpha particles and $Q_n = 14.06$

MeV of neutrons is $Q = 17.58$ MeV per reaction. The distribution of the energy between alpha particles and neutrons in the fusion reaction can be calculated based on the energy and momentum conservation and the result is determined by the mass ratio ($Q_n : Q_\alpha = m_\alpha : m_n = 0.8 : 0.2$). For equally mixed D-T plasma (i.e. $n_{\mathrm{D}} = n_{\mathrm{T}} = \frac{n}{2}$), the number of reactions per unit time per unit volume is $\left(\frac{n}{2}\right)^2 \langle \sigma v \rangle$ and the fusion power density P can be obtained from:

$$P = \left(\frac{n}{2}\right)^2 \langle \sigma v \rangle Q \tag{1.5}$$

When the fusion powers carried by the neutron and alpha particles are labeled by P_n and P_α, then $P_n = 0.8\ P$ and $P_\alpha = 0.2\ P$. The available heating power for the plasma can be found from:

$$(0.8\eta_{\mathrm{el}}\gamma\eta_{\mathrm{heat}} + 0.2)P = \eta P \tag{1.6}$$

where η_{el} is the thermal-to-electric conversion efficiency, γ is a numerical factor (less than unity), η_{heat} is the heating efficiency, and $\eta = 0.8\eta_{\mathrm{el}}\gamma\eta_{\mathrm{heat}} + 0.2$. In order to achieve a net energy gain, the following condition must be met:

$$P_{\mathrm{heat}} = P_L + P_R = \frac{3nT}{\tau_E} < \eta P \tag{1.7}$$

Recalling Equation 1.5, the above condition leads to:

$$\frac{3nT}{\tau_E} < \eta \frac{Q}{4} n^2 \langle \sigma v \rangle \tag{1.8}$$

or

$$n\tau_E > \frac{12T}{\eta Q \langle \sigma v \rangle} \tag{1.9}$$

The ignition condition for equally mixed D-T plasma corresponding to the case $\eta = 0.2$ is called the Lawson criterion [10]. The break-even or the critical condition ($\eta = 1$) implies that when the total heating power P_{heat} reaches an equal value of the total fusion power P. Figure 1.4 shows

required plasma parameters in a D-T plasma for both ignition and break-even states. The lower the η value (less efficient energy conversion), the more stringent plasma conditions are. Another key parameter called fusion triple product $nT_i\tau_E$ is used to indicate how close the plasma is to the ignition state in commercial reactors [11]:

$$nT_i\tau_E > 5 \times 10^{21} \text{ keV} \cdot \text{s/m}^3 \tag{1.10}$$

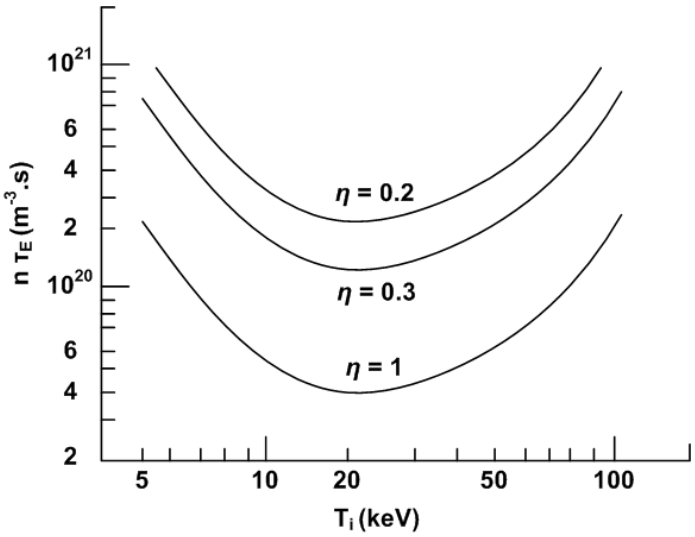

Figure 1.4: The ignition condition ($\eta = 0.2$) and the break-even condition ($\eta = 1$) for a D-T fusion plasma [6].

Clearly, the fusion triple product is considered the main figure of merits in a fusion device. The triple product has to be increased to the required values before proposing the tokamak reactor as a new source of energy. Another operational issue in tokamaks relates to multifarious instabilities that occur in the tokamak plasma. The plasma is generally confined in tokamaks using a complex configuration of magnetic fields. Since the behavior of the plasma in the electric and magnetic fields is governed by fluid and electromagnetic equations, the instabilities in plasma is also termed magnetohydrodynamic (MHD) instabilities. MHD instabilities are deemed as a major cause for the energy loss in the plasma since they tend to shorten the energy confinement time and to reduce the temperature and density. It is important to study MHD instabilities in tokamak plasmas. Tokamaks are usually equipped with numerous diagnostic tools including Mirnov pick-up coils, electron cy-

clotron emission (ECE) diagnostics, interferometers, polarimeters and soft x-ray (SXR) cameras to monitor plasma perturbations that are usually associated with MHD instabilities in tokamaks.
In the Saskatchewan Torus-Modified (STOR-M) tokamak, a set of magnetic coils called discrete Mirnov coils were assembled and placed at multiple poloidal and toroidal locations. Also, a new SXR system consisting of horizontal and vertical photodiode arrays has been mounted recently on the STOR-M tokamak. The combination of Mirnov coils and SXR cameras is employed for studying MHD instabilities in STOR-M. The valuable information regarding MHD instabilities were retrieved by using various signal processing techniques such as the singular value decomposition algorithm, wavelets and some other Fourier-based techniques. These techniques have the ability to extract the spatial structures and temporal evolutions of signal harmonics (MHD modes) from the raw data.

1.4 Research Motivations and Objectives

The main activities and motivations of this thesis work are outlined below:

1. Assembling 32 discrete Mirnov coils and arranging them into four poloidal sets.

2. Calibrating the Mirnov coils and assuring the impedance matching of the setup.

3. Mounting the coils on STOR-M tokamak at four different toroidal locations separated by 90°.

4. Investigating and monitoring the MHD instabilities in STOR-M tokamak during normal tokamak operation or with compact torus injection.

5. Studying MHD features by analyzing the recorded data using some signal processing techniques like Fourier, wavelets and singular value decomposition via MATLAB (Matrix Laboratory) built-in scripts.

1.5 Thesis Outline

An introduction to the global energy demand, fusion reactions and fusion-based power plants was highlighted in this chapter. The remainder of this thesis is outlined below:

- Chapter 2 details the principles of plasma confinement and equilibrium in tokamaks. A brief description of STOR-M tokamak, compact torus injector and some magnetic diagnostics is presented.

- Chapter 3 explains MHD theory and magnetic topology in a tokamak plasma as well as experimental observations of MHD instabilities in tokamaks.

- Chapter 4 presents the mathematical basis of the signal processing techniques used in this research, followed by their applications in plasma diagnostics.

- Chapter 5 describes the apparatus layout and installation of the conventional Mirnov $m = 2$ and $m = 3$ coils, discrete Mirnov coils and SXR system in the STOR-M tokamak.

- Chapter 6 discusses the recent results of the numerical analyses that were carried out on MHD modes simulations. The recent experimental results obtained during STOR-M normal confinement discharge (L-mode) and compact torus injection experiment are discussed.

- Chapter 7 summarizes the major findings of this research and suggests some ideas for possible future work.

Chapter 2

Tokamak

2.1 Introduction

Tokamaks are designed to generate plasma using several heating methods (ohmic heating (OH), radio frequency (RF) heating, etc.) and to confine it by a combination of external and self-induced magnetic fields. The plasma species (i.e. electrons and ions) have a trend to drift away from their original guiding centers toward the outer wall of the vacuum chamber, which causes plasma loss. Confining the plasma with a nested helical magnetic field is required to avoid the guiding center drifts. This chapter highlights tokamak equilibrium in the major radius direction. A brief introduction to STOR-M tokamak, compact torus injector and some STOR-M diagnostics is presented as well.

2.2 Magnetic Confinement

One of the most effective techniques of plasma confinement involves the use of solenoid magnetic fields. If a particle of charge q and mass m is placed in a magnetic field B, the particle motion is determined by the Lorentz force [12]:

$$m\frac{d\mathbf{v}}{dt} = q(\mathbf{v} \times \mathbf{B}) \tag{2.1}$$

In case of a uniform straight B field produced by a helical electrical current, electrons and ions will move depending on the initial particle velocity, with both parallel and perpendicular components with respect to the B field lines, in spiral motion with a cyclotron frequency defined by [13]:

$$\omega_c = \frac{|q|B}{m} \tag{2.2}$$

The orbital radius of the particle about its guiding center is commonly known as the Larmor radius:

$$r_L = \frac{v_\perp}{\omega_c} = \frac{mv_\perp}{|q|B} \tag{2.3}$$

where $v_\perp$ is the velocity component of the particle in the plane perpendicular to the magnetic field. This uniform, straight magnetic field confines charged particles within the Larmor radius in the perpendicular direction. However, the particles are free to move along the field lines. If the solenoid is bent to a toroid, the field lines will close on themselves. This pure toroidal magnetic field may seem sufficient to confine the particles perfectly in the direction perpendicular to the magnetic field. However, this simple toroidal magnetic field is not enough to confine the plasma properly. In fact, the magnetic field in any toroidal device is stronger at smaller radii than it is at larger radii.

From Equation 2.3, it is clear that as the particles rotate around the magnetic field lines, they will have slightly narrower orbits at smaller major radial locations with larger B than at larger major radial locations with smaller B, causing them to drift. A simple toroidal magnetic field causes two types of particle drifts, the curvature and gradient drifts, which are given by [14]:

$$\mathbf{v}_R = \frac{mv_\parallel^2}{qB^2}\frac{\mathbf{R}_c \times \mathbf{B}}{R_c^2} \qquad \text{Curvature Drift} \tag{2.4}$$

$$\mathbf{v}_{\nabla B} = \pm\frac{1}{2}v_\perp r_L \frac{\mathbf{B} \times \nabla B}{B^2} \qquad \text{Gradient Drift} \tag{2.5}$$

where R_c is the radius of magnetic field curvature, $v_\parallel$ and $v_\perp$ are parallel and perpendicular components of particle velocity relative to the magnetic field. Since the drift direction depends on the

sign of the charge, the electrons and ions will drift in the opposite vertical directions. As a result, a charge separation between electrons and ions occurs as shown in Figure 2.1. This charge separation creates electric field which leads to another type of drift called $\mathbf{E} \times \mathbf{B}$ drift:

$$\mathbf{v}_{\mathbf{E}\times\mathbf{B}} = \frac{\mathbf{E} \times \mathbf{B}}{B^2} \tag{2.6}$$

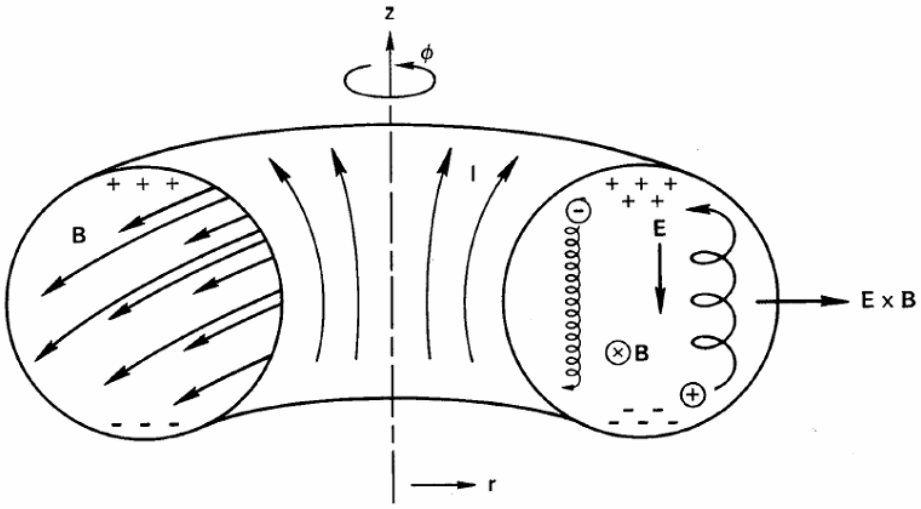

Figure 2.1: Particle motion in a toroidal field [14].

The last drift negatively affects the plasma confinement since all the particles drift toward the outer wall. This problem can be solved by superimposing an additional poloidal magnetic field B_θ on the toroidal field B_ϕ to form nested helical magnetic lines. The helical magnetic field guides the electrons and ions along its magnetic field lines, so the positive charge drifting upwards will eventually go down along the helical magnetic field line and the charge separation is neutralized (see also Figure 2.3).

2.3 Tokamak Equilibrium

The idea of the tokamak was originally conceived by the two Russian physicists *Igor Tamm* and *Andrei Sakharov* back in the 1950's [15]. The term "Tokamak" is an acronym of a Russian phrase

(**To**roidal'naya **ka**mera s **ma**gnitnymi **k**atushkami) which means "toroidal chamber with magnetic coils". A tokamak is a donut-shaped device that uses magnetic fields to confine the plasma. A central solenoid is used to drive the toroidal plasma current. The plasma torus is regarded as a single secondary winding of a transformer. As shown in Figure 2.2, a current flowing in the primary transformer winding induces a plasma current by transformer actions (with either iron or air core). The induced toroidal plasma current I_p generates a poloidal magnetic field B_θ. In addition, an external toroidal magnetic field B_ϕ is induced by the toroidal field coils, which is perpendicular to B_θ. The resultant magnetic field $\mathbf{B} = \mathbf{B}_\phi + \mathbf{B}_\theta$ has a helical structure shown in Figure 2.3. Naturally, the plasma has a tendency to expand radially outward to increase its inductance [16]:

$$L = \mu_0 R \left[\ln\left(\frac{8R}{a}\right) - 2 + \frac{l_i}{2} \right] \tag{2.7}$$

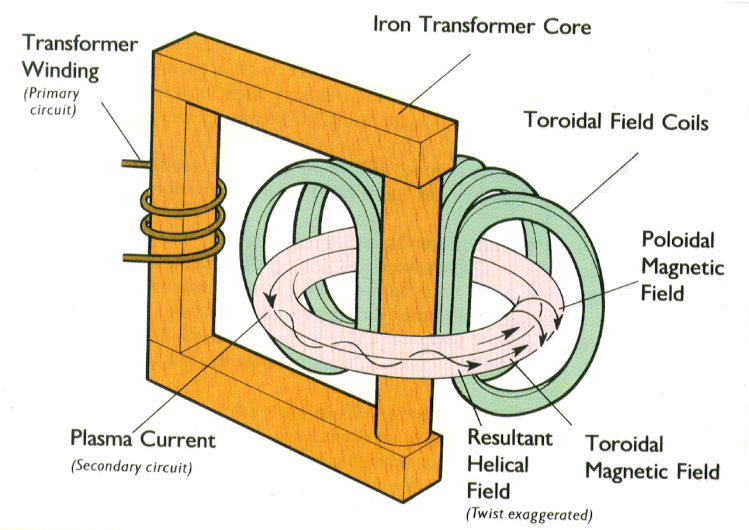

Figure 2.2: A schematic drawing of a tokamak reactor.

where R is the major radius of the plasma, a is the minor radius, $\mu_0 = 4\pi \times 10^{-7}$ H/m is the vacuum permeability and l_i is the internal inductance parameter which is defined, for a straight cylinder approximation suitable for large aspect ratio $\frac{R}{a}$ tokamaks (thin plasma column), by:

$$l_i = \frac{\langle B_\theta^2 \rangle}{B_\theta^2(a)} = \frac{2\pi \int_0^a B_\theta^2(r) r dr}{\pi a^2 B_\theta^2(a)} \tag{2.8}$$

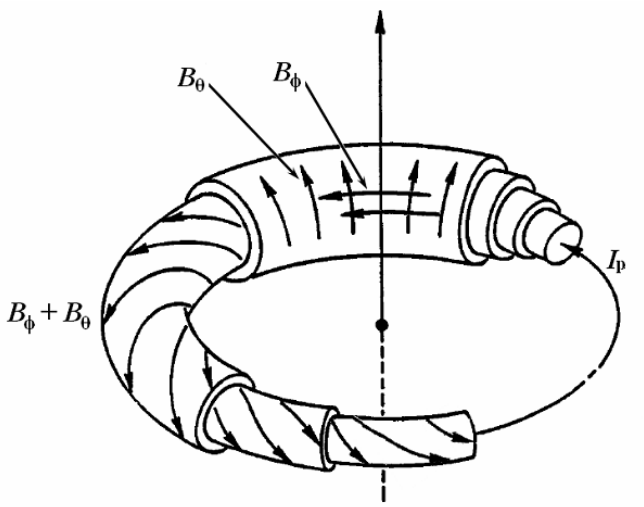

Figure 2.3: The resultant helical magnetic field in a tokamak [17].

where $B_\theta(r)$ and $B_\theta(a)$ are the poloidal magnetic field as a function of distance r from the center of the plasma column and at the edge of the plasma column $r = a$. The internal inductance parameter depends on the plasma current distribution: $l_i = \frac{1}{2}$ for uniform toroidal current J_ϕ and $l_i = 0$ for skin current. The radial force due to the self-inductance is given by:

$$\begin{aligned} F_1 &= \frac{\partial}{\partial R}\left(\frac{1}{2}LI_p^2\right) \\ &= \frac{1}{2}\mu_0 I_p^2\left[\ln\left(\frac{8R}{a}\right) - 1 + \frac{l_i}{2}\right] \end{aligned} \tag{2.9}$$

The confined plasma in a toroidal chamber also tends to expand radially due to the ballooning force:

$$F_2 = \frac{\partial}{\partial R}\left(2\pi^2 R a^2 \langle p\rangle\right) = 2\pi^2 a^2 \langle p\rangle \tag{2.10}$$

where $\langle p\rangle$ is the average plasma pressure:

$$\langle p\rangle = \frac{2\pi}{\pi a^2}\int_0^a p(r) r dr \tag{2.11}$$

Moreover, the radial force that accompanies the plasma diamagnetism and paramagnetism, due to

the self transformer action, is:

$$F_3 = -\frac{\partial}{\partial R}\left[\left(\frac{B_\theta^2(a)}{2\mu_0} - \langle p\rangle\right) 2\pi^2 R a^2\right]$$
$$= -2\pi^2 a^2 \frac{B_\theta^2(a)}{2\mu_0}(1-\beta_\theta) \tag{2.12}$$

where $B_\theta(a) = \frac{\mu_0 I_p}{2\pi a}$ is the poloidal magnetic field at the plasma edge ($r = a$) and the poloidal beta factor β_θ is defined by:

$$\beta_\theta = \frac{\langle p\rangle}{B_\theta^2(a)/2\mu_0} \tag{2.13}$$

Therefore, an additional vertical magnetic field $B_\perp$ must be applied to a tokamak discharge to counterbalance the total expanding force $F_1 + F_2 + F_3$ and to prevent the plasma column from moving along the major radius R direction (the equilibrium condition in the minor radius a direction will be discussed later in Section 3.4). This vertical magnetic field exerts a Lorentz force radially inward $2\pi R I_p B_\perp$ which counterbalances the outward expansion force. The required vertical magnetic field is:

$$B_\perp = \frac{\mu_0 I_p}{4\pi R}\left[\ln\left(\frac{8R}{a}\right) + \beta_\theta + \frac{l_i}{2} - \frac{3}{2}\right] \tag{2.14}$$

In addition to the main vertical field proportional to the plasma current, a small variation of the vertical field is needed to account for the variation of plasma parameters. In the STOR-M tokamak, the vertical field consists of the following parts: the image current induced by the transformer, the pre-programmed vertical field proportional to the primary OH windings, and the feedback vertical field based on the measured plasma horizontal position ΔH.

2.4 STOR-M Tokamak

STOR-M is the only research tokamak in Canada at the present time. It is an improved version of the previous Saskatchewan Torus-1 Modified (STOR-1M) tokamak [18]. The construction was completed in 1987 and its toroidal magnetic field system was upgraded in 1994 [19]. STOR-

M contributed to the tokamak research with several recognized experiments including turbulent heating (TH) current pulse [20], plasma biasing [21], alternating current (AC) operation [22], and both tangential and vertical compact torus injection [23, 24]. Some of those experiments were conducted to achieve highly confined plasma during the ohmic discharge. Additionally, a compact torus injector has been used in STOR-M as a novel means to fuel tokamaks and to enhance bootstrap current through density profile optimization [25]. So far, over 200,000 shots have been logged for various experiments. Table 2.1 lists some key parameters of STOR-M.

Parameter	**Value**
Toroidal Magnetic Field (B_ϕ)	$\leqslant$ 1 Tesla
Vertical Magnetic Field ($B_\perp$)	60 Gauss
Plasma Current (I_p)	30-40 kA
Loop Voltage (V_p)	3 V
Average Electron Density ($\langle n_e \rangle$)	10^{18}-10^{19} m^{-3}
Average Electron Temperature ($\langle T_e \rangle$)	150 eV
Average Ion Temperature ($\langle T_i \rangle$)	50 eV
Energy Confinement Time (τ_E)	2 ms
Discharge Duration	40 ms
Minor Radius (a)	12.5 cm
Major Radius (R)	46 cm

Table 2.1: List of STOR-M main parameters.

The STOR-M tokamak consists of a donut-shaped vacuum chamber and limiter made of stainless steel (304L alloy). The vacuum chamber has two circular stainless steel elbows attached on one end to stainless steel bellows to form the two halves of the vacuum chamber. Bellows are used to reduce the mechanical stress. The chamber is equipped with fourteen ports, nine horizontal, four vertical and one tangential designated for pumping, the compact torus injector, diagnostics and a gas feed. Evacuating the chamber is preformed by using a large turbo-molecular pump with a pumping capacity up to 1000 L/sec [26] backed by a rotary pump to achieve a base pressure of 1 $\times$ 10^{-7} Torr. For the STOR-M tokamak, the vacuum chamber is filled with ultra pure Hydrogen (99.999%) through a PV-10 piezoelectric valve [27] to attain the typical operating pressure about

1.8×10^{-4} Torr maintained by a Veeco automatic pressure controller [28].

The toroidal ohmic plasma current is formed by an iron core transformer with inductive magnetic flux capacity of ± 0.1 Wb. The ohmic discharge system consists of three parts. A negatively biased magnetic flux is induced by a bias bank (450 V, 20 mF). A fast bank (450 V, 200 mF) is triggered for initial ionization and current ramp-up. A slow bank (100 V, 10 F) is used to sustain the plasma current plateau. As explained earlier, the position of the plasma column is controlled by a vertical magnetic field to counterbalance the expanding force along the major radius direction and this field is provided by the image current and the pre-programmed vertical field. An active feedback (FB) position control system maintains the balance for plasma based on the position signals. Figure 2.4 shows a vertical cross-section of STOR-M tokamak along with locations of the OH primary coils (8 turns), the vertical equilibrium (VE) coils and FB coils.

2.5 Compact Torus Injector

Compact torus (CT) injection is considered a promising candidate for tokamak central fueling. CT fueling involves injecting a self-contained compact plasma torus at a high velocity. A CT is formed in a magnetized plasma gun and subsequently accelerated using a rail gun. An accelerated CT is able to penetrate into the plasma core and deposit fuel there. The kinetic energy density of CT exceeds the magnetic energy density in the target plasma.

University of Saskatchewan Compact Torus Injector (USCTI) was installed on STOR-M in 1995. Its main objective is to investigate the feasibility of CT injection as a fueling technique in future tokamak reactors. The main advantage of using the USCTI is its ability to fire CT from different injection angles relative to the STOR-M toroidal field. The USCTI is a coaxial plasma gun and acceleration of CT is provided by the Lorentz force $\mathbf{J} \times \mathbf{B}$ in the acceleration region. As it is shown in Figure 2.5, the USCTI has two sets of identical capacitor banks of 20 kV and 20 μF which are used for consecutive formation and acceleration discharges with a time delay of several microseconds. The plasma gun consists of formation, compression, acceleration and focusing sections in a

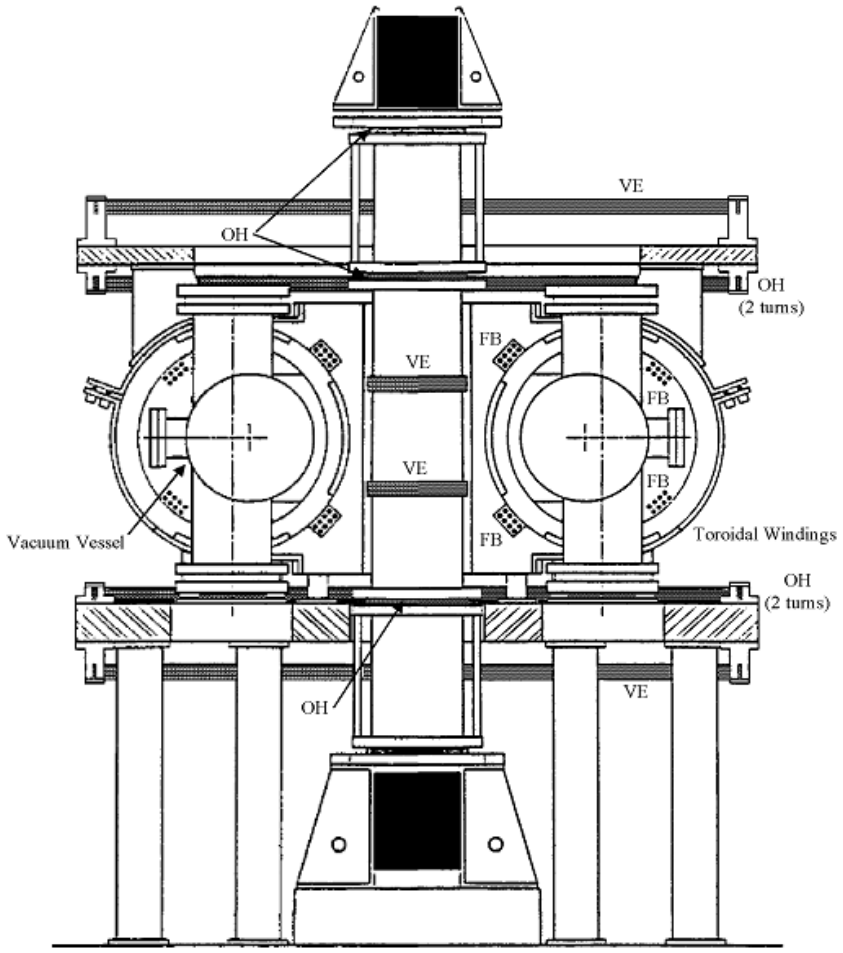

Figure 2.4: Vertical cross-section of the STOR-M tokamak.

coaxial configuration. The outer and inner electrode radii are 5 cm and 1.78 cm, respectively. An internal solenoid is used to produce a quasi-steady state bias magnetic flux ($\Phi_{\text{bias}} = 1.8$ mWb) for CT formation.

The CT is formed by injecting a pure hydrogen gas (99.999%) into the circular gap between the inner and outer electrodes through four fast electromagnetic valves evenly distributed around the outer formation electrode. After the CT is formed through gas breakdown, it enters the compression section with a length of 91 mm and compression ratio of 1.46. The CT radius changes from 74 mm to 50 mm. The acceleration section is 60 cm long. A cone is used at the exit of the acceleration section to further compress the CT to a smaller size. The surfaces of the electrodes are coated with tungsten or chromium to minimize the impurity level in the CT. The electrodes are regularly baked

to a temperature of 70° using electrical heating tapes.

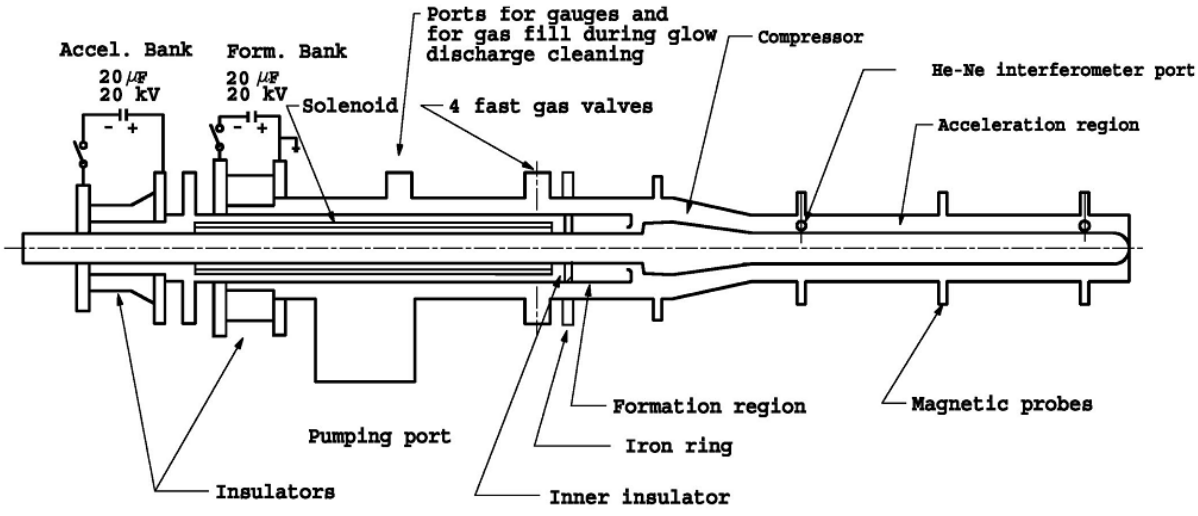

Figure 2.5: Layout of the USCTI device.

There are four diagnostic ports along the acceleration section at axial locations 0, 22, 43, and 65 cm which are designated for mounting magnetic probes to measure the strength of CT magnetic fields at the outer walls in both poloidal and toroidal directions. Two of these ports are located in the outer acceleration electrode and they are used to detect CT density using a He-Ne laser interferometer. A CT deposits its fuel in a tokamak through magnetic reconnection [29]. Table 2.2 lists the main CT parameters at the exit of the acceleration region.

Parameter	**Value**
Radius	5 cm
Length	$\sim$ 15 cm
Density (n_{CT})	1-4 $\times$ 10^{21} m^{-3}
Electron Temperature	$\leqslant$ 10 eV
Magnetic Field	$\sim$ 0.2 T
Velocity (v_{CT})	150 km/s
Mass	$\leqslant$ 1 μg

Table 2.2: The main parameters of an USCTI compact torus [24].

2.6 Magnetic Measurements in STOR-M

Tokamaks are usually equipped with a set of diagnostic instruments for measuring specific plasma parameters during the tokamak discharge. It is desirable to measure these parameters with high precision. Some of the diagnostics are operated passively by installing them at the cooler edge of the plasma in the shadow of the limiter known as the scrape-off layer (SOL). This passive configuration is required to avoid disturbing the plasma that may lead to degrading plasma confinement. Also, the diagnostics can be a source of impurities if they make a direct contact with the hot plasma. The direct contact with the hot plasma may also damage the probes or even evaporate them. Therefore, non-invasive techniques are needed to measure plasma parameters [30]. In the STOR-M tokamak, a standard set of diagnostics is routinely used for monitoring plasma and machine parameters during the operation. Table 2.3 contains a list of main diagnostics in the STOR-M tokamak.

Diagnostic	**Plasma Parameter**
Rogowski Coils	Plasma Current (I_p) and Toroidal Field (B_ϕ)
Voltage Pick-Up Loop	Loop Voltage (V_p)
Microwave Interferometer (4 mm)	Electron Density (n_e)
Position Sensing Coils	Plasma Position (ΔH)
Mirnov Coils	MHD Magnetic Fluctuations ($\tilde{B}$)
Microwave Scattering (2 mm)	Density Fluctuations ($\tilde{n}$)
Diamagnetic Coils	Diamagnetic/Paramgnetic Flux ($\Phi_{d,p}$)
Gundestrup Probe	Flow Measurements ($M_{\parallel,\perp}$)
Langmuir Probes	Electron Density (n_e) and Temperature (T_e)
SXR Cameras	Perturbed Electron Density ($\tilde{n}_e$) and Temperature ($\tilde{T}_e$)

Table 2.3: List of STOR-M diagnostics.

The locations of diagnostics on STOR-M are shown in Figure 2.6. In this section, the technical and theoretical concepts of some magnetic instruments used in STOR-M are discussed concisely. The apparatus of Mirnov coils and SXR system will be explained in more detail later in Chapter 5.

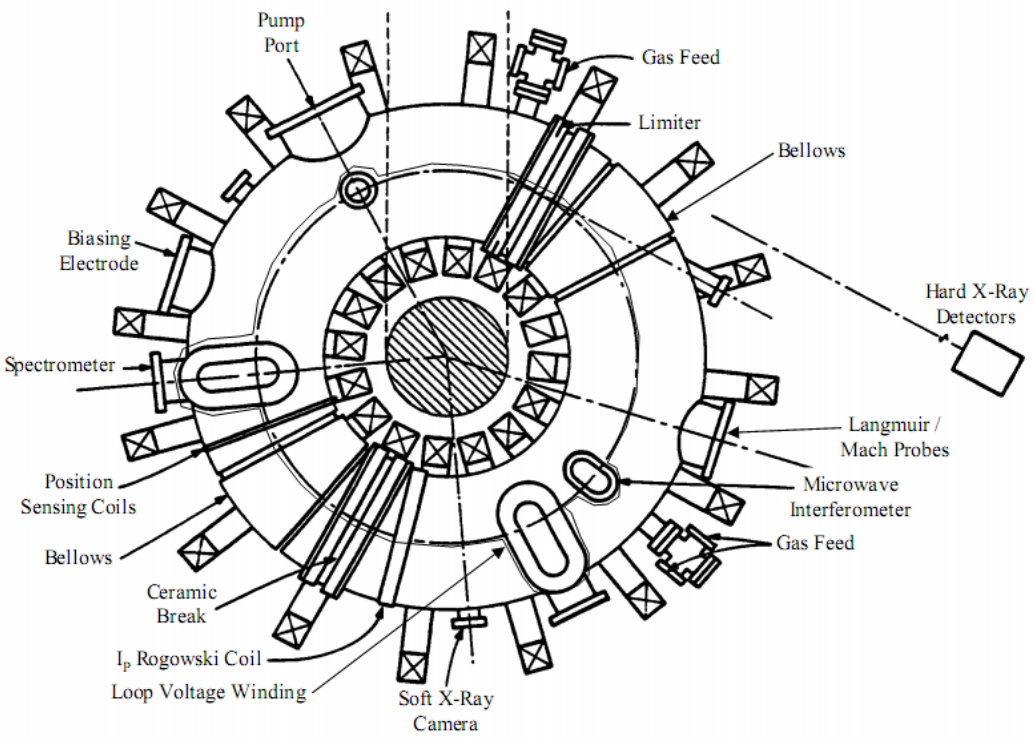

Figure 2.6: Diagnostics locations on the STOR-M tokamak.

2.6.1 Rogowski Coils

A Rogowski coil is normally used for measuring electric currents in various field windings and within the plasma itself. It is constructed from a torus-shaped solenoidal coil, shown in Figure 2.7, with a uniform cross-section A and winding density n (turns/m). If an electric current I passes through the center of the coil, a perpendicular magnetic field B_θ is induced according to Ampere's law [31]:

$$\oint_l \mathbf{B}_\theta \cdot d\mathbf{l} = \mu I \tag{2.15}$$

where $d\mathbf{l}$ is the line element along the solenoidal axis and μ is the magnetic permeability of the medium in the solenoid. Recalling Faraday's law, the total magnetic flux linkage Φ can be written as an integral over winding density n:

$$\Phi = n \oint_l \int_A dA \mathbf{B}_\theta \cdot d\mathbf{l} \tag{2.16}$$

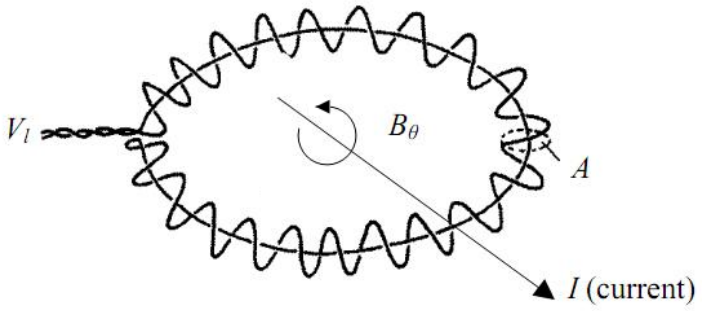

Figure 2.7: Typical Rogowski coil [32].

Using Equation 2.15, the magnetic flux can be also expressed in terms of I as:

$$\Phi = nA\mu I \tag{2.17}$$

The voltage induced by the Rogowski coil (V) can be directly obtained from the time rate of the magnetic flux $V = \dot{\Phi} = nA\mu\dot{I}$, which in turn can be integrated to calculate the enclosed current (I) of the coil:

$$I = \frac{1}{nA\mu}\int V dt \tag{2.18}$$

The main advantage of the Rogowski coil is that it can be made with an open end for more flexibility, allowing it to be wrapped around any conductor without disturbing it. Since the Rogowski coil has an air core rather than an iron core, the coil has a low inductance and can respond to rapidly changing currents. Also, because the coil has no iron core to saturate, the output voltage is highly linear even when subjected to large currents like the plasma currents in tokamaks.

2.6.2 Voltage Pick-Up Loop

As shown in Figure 2.8, plasma loop voltage can be easily measured by placing a single turn loop on the top of the vacuum chamber parallel to the toroidal plasma current. The triaxial cable is used to reduce the electromagnetic noise. A voltage divider is used to match the range of the data acquisition system and for impedance matching. The measured voltage (V_p) consists of resistive

and inductive components of the loop voltage which is expressed by:

$$V_p = I_p R_p + \frac{d}{dt}\left(I_p L_p\right) \tag{2.19}$$

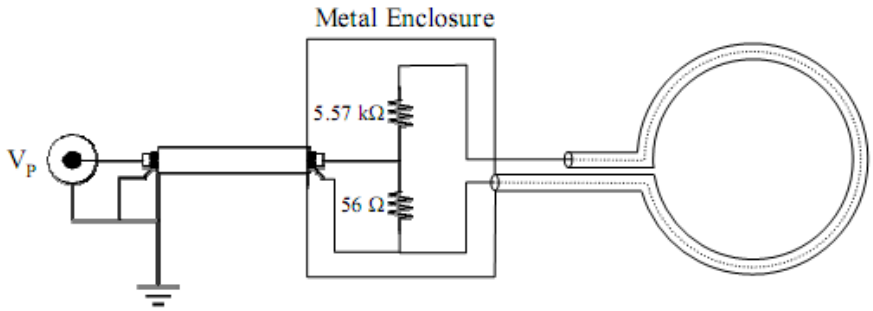

Figure 2.8: Voltage pick-up loop circuit [33].

where I_p is the plasma current, R_p is the plasma resistance and L_p is the plasma inductance. The plasma resistance and inductance are respectively given by [34]:

$$R_p = \eta \frac{2\pi R}{\pi a^2} \tag{2.20}$$

$$L_p = \mu_0 R \left[\ln\left(\frac{8R}{a}\right) - 2 + \frac{l_i}{2}\right] \tag{2.21}$$

where R is the major radius, a is the minor radius, l_i is the internal inductance which has been defined by Equation 2.8 and η is the plasma resistivity. Using the fully ionized plasma approximation, the plasma current and loop voltage can be used to estimate the so-called Spitzer resistivity η ($\Omega \cdot$ m) for average electron temperature T_e [35]:

$$\eta = 1.65 \times 10^{-9} \frac{Z_{\text{eff}} \ln \Lambda}{T_e^{\frac{3}{2}}} \tag{2.22}$$

Spitzer resistivity has a strong dependance on electron temperature T_e (keV) and effective ion charge number Z_{eff}. The Coulomb logarithm $\ln \Lambda$, which accounts for the multiple small angle

collisions inside the plasma, can be calculated from Debye length $\lambda_D = \sqrt{\frac{\varepsilon_0 T_e}{n_e e^2}}$ as:

$$\ln \Lambda = \ln \left(12\pi n_e \lambda_D^3\right) \tag{2.23}$$

or, alternatively, can be set to 15 [36]. Another important application for the voltage pick-up loop surrounding the iron core is measuring the transformer core flux Φ_{OH} since the flux can be calculated directly by integrating loop voltage V_{core} using a gated integrator, so that:

$$\Phi_{\text{OH}} = \int V_{\text{core}} dt \tag{2.24}$$

2.6.3 Position Sensing Coils

Controlling the plasma column in tokamaks is a vital task to maintain the quality of plasma during the ohmic discharges. Most tokamak devices are equipped with a set of magnetic coils called position sensing coils which detect the accurate location of the plasma column position in the vacuum chamber. The coils configuration shown in Figure 2.9 consists of six magnetic probes mounted outside the vacuum vessel. Four of the probes are designated for measuring the poloidal magnetic field B_θ at the same toroidal location, but poloidally separated by 90°. The other two probes are installed at the poloidal angles $\pm 90°$ to detect the radial magnetic field B_r.

Although the position sensing coils are designed to measure the desirable magnetic field induced by the plasma current, they also pick up some unwanted magnetic fields such as that produced by the toroidal field coils. A compensation circuit is required to eliminate the unwanted signal pick-up due to imperfect alignment of probes. In order to eliminate, or at least to minimize, these unwanted magnetic fields, Rogowski coils are used to determine the current waveforms which produce the unwanted magnetic fields. These waveforms are then added with the appropriate amplitude and polarity to the position output signals to cancel the unwanted magnetic field contribution. To accomplish this, the gains are adjusted in the absence of the plasma, while all other fields are present, until the coil signals are as close to zero as possible.

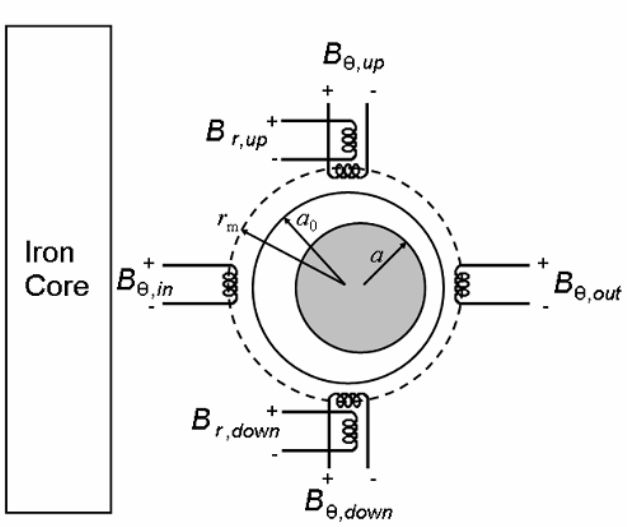

Figure 2.9: Plasma position sensing coils [37].

Experimentally, measuring the exact location of ΔH is not straightforward. In fact, approximations must be considered to simplify the mathematical forms of B_θ and B_r involved in ΔH calculations. Using the approximation of a tokamak device with a thin wall discharge chamber having toroidal gaps, the poloidal and radial components of the magnetic field at radius r_m from the vacuum chamber center can be expressed as [38]:

$$B_\theta = \frac{\mu_0 I_p}{2\pi r_m} - \frac{\mu_0 I_p}{4\pi r_m}\left[\ln\left(\frac{a}{r_m}\right) + 1 - \left(\Delta + \frac{1}{2}\right)\left(\frac{a^2}{r_m^2} + 1\right) - \frac{2R\Delta H}{r_m^2}\right]\cos\theta \tag{2.25}$$

$$B_r = -\frac{\mu_0 I_p}{4\pi r_m}\left[\ln\left(\frac{a}{r_m}\right) + \left(\Delta + \frac{1}{2}\right)\left(\frac{a^2}{r_m^2} - 1\right) + \frac{2R\Delta H}{r_m^2}\right]\sin\theta \tag{2.26}$$

where Δ is the Shafranov parameter which is defined by:

$$\Delta = \beta_\theta + \frac{l_i}{2} - 1 \tag{2.27}$$

The plasma position signal ΔH and the factor $\beta_\theta + \frac{l_i}{2}$ can be estimated by solving Equations 2.25

and 2.26 for $B_\theta(\theta = 0, \pi)$ and $B_r\left(\theta = \frac{\pi}{2}, \frac{3\pi}{2}\right)$ which give [39]:

$$\Delta H = \frac{a}{4R_0}\left[\left(\frac{r_m^2}{a^2} - 1\right) - 2\ln\left(\frac{a}{r_m}\right)\right] + \frac{\pi r_m^2}{2\mu_0 I_p}\left[\langle B_\theta\rangle\left(1 - \frac{a^2}{r_m^2}\right) - \langle B_r\rangle\left(1 + \frac{a^2}{r_m^2}\right)\right] \quad (2.28)$$

$$\beta_\theta + \frac{l_i}{2} = 1 + \ln\left(\frac{a}{r_m}\right) + \frac{\pi R_0}{\mu_0 I_p}\left[\langle B_\theta\rangle + \langle B_r\rangle\right] \quad (2.29)$$

Here, R_0 is the major radius of the vacuum vessel, $\langle B_\theta\rangle \equiv B_\theta(\theta = 0) - B_\theta(\theta = \pi)$ and $\langle B_r\rangle \equiv B_r\left(\theta = \frac{\pi}{2}\right) - B_r\left(\theta = \frac{3\pi}{2}\right)$. The determination of the horizontal plasma displacement by this technique is commonly used in most tokamaks because of its simplicity.

2.6.4 Diamagnetic Coils

For any tokamak plasma in equilibrium, the change in total toroidal flux, from both diamagnetism and paramagnetism, can be written as [40]:

$$\Delta\Phi_\phi = \frac{\mu_0^2 I_p^2}{8\pi B_\phi}\left(1 - \beta_{\theta\perp}\right) \quad (2.30)$$

where the transverse poloidal beta $\beta_{\theta\perp}$

$$\beta_{\theta\perp} = \frac{16\pi^2}{\mu_0 I_p^2}\int_0^a nT_\perp r dr \quad (2.31)$$

is expressed in terms of the transverse plasma temperature $T_\perp = T_{e\perp} + T_{i\perp}$ (Joules). The plasma current induces either a diamagnetic flux Φ_d or paramagnetic flux Φ_p. In the diamagnetic case, the axial magnetic field is reduced inside the plasma compared with its constant value at the plasma edge, $\langle B_\phi^2\rangle < B_\phi^2(a)$. The paramagnetic case corresponds to $\langle B_\phi^2\rangle > B_\phi^2(a)$. The distinction can be made based on the value of the poloidal beta parameter β_θ which is given by Equation 2.13:

$$\beta_\theta = \frac{\langle p\rangle}{B_\theta^2(a)/2\mu_0}\begin{cases} > 1 & \text{Diamagnetic} \\ < 1 & \text{Paramagnetic} \end{cases} \quad (2.32)$$

To measure the plasma diamagnetic flux, a single turn loop, shown in Figure 2.10, produces a voltage (V_L) which corresponds to the desired diamagnetic flux component as well as some unwanted flux components:

$$V_L = -\frac{d\Phi_d}{dt} - \frac{d\Phi_{\phi_e}}{dt} - \frac{d\Phi_\theta}{dt} - \frac{d\Phi_{\text{vib}}}{dt} - \frac{d\Phi_T}{dt} \tag{2.33}$$

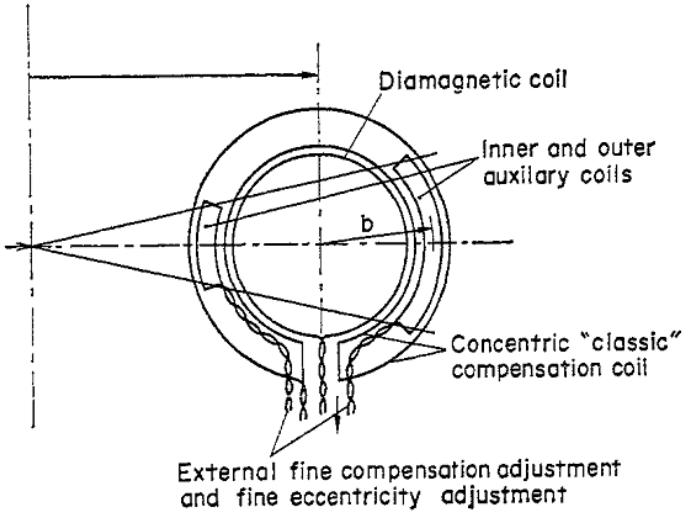

Figure 2.10: Diamagnetic coil and compensation coils [41].

where Φ_{ϕ_e} is the toroidal magnetic flux externally applied in the tokamak, Φ_θ is the strayed poloidal magnetic flux, Φ_{vib} is the vibrational flux and Φ_T is the thermal expansion flux. Compensation coils are required to eliminate the unwanted flux components. To exclude Φ_{ϕ_e} and Φ_θ from the output signal, non-enclosed primary compensation windings, mounted around the main diamagnetic coil, are designed to undetect the diamagnetic flux. The voltage induced by this coil

$$V_C = -\frac{d\Phi_{\phi_e}}{dt} - \frac{d\Phi_\theta}{dt} \tag{2.34}$$

is subtracted from the diamagnetic loop signal to remove the contribution of the external toroidal flux and poloidal flux. For the vibrational flux, mechanically isolating the diamagnetic coil from the vacuum chamber is needed to minimize vibrational noise-to-signal ratio. The expected signal

from the diamagnetic loop, after signal compensation, is readily determined by:

$$V_d = \frac{d\Delta\Phi_d}{dt} = \frac{\mu_0^2}{8\pi}\frac{d}{dt}\left(\frac{I_p^2\left(1-\beta_\theta\right)}{B_\phi(a)}\right) \tag{2.35}$$

Since the diamagnetic flux is significantly small compared to the total magnetic flux presented in a tokamak, the electronics employed for the diamagnetic measurements have to be extremely responsive to the low signal input.

Chapter 3

Magnetohydrodynamics Theory

3.1 Introduction

MHD theory is important in plasma physics. On one hand, MHD theory facilitates the general understanding of plasma behavior in tokamaks, for the plasma can be well modeled as a conductive fluid. On the other hand, the vast majority of plasma degradations and disruptions are attributed to MHD instabilities. The basics of MHD theory, MHD equilibria and magnetic surfaces in tokamaks are explained in this chapter along with a brief theoretical and experimental aspects of MHD instabilities.

3.2 Theoretical Background

Magneto-hydro-dynamics literally means magnetic fluid dynamics. It is a theoretical model developed to solve macroscopic dynamical problems that are imposed by the movement of charged particles in electrically neutral fluid and their interaction with the surrounding magnetic fields. In return, the electric currents produce magnetic field which causes a relative drift between the two fluids of opposite charge density which permeate each other.

This is a brief introduction to the concepts of the ideal MHD theory. In the ideal MHD theory, the effects of dissipation in all forms are negligible, these include resistivity, thermal conductivity,

and viscosity. The electron and ion fluids are separately treated as an ideal MHD fluid. The two fluids interact only through the electric and magnetic fields they induce. These fields in turn react to changes in the charge densities and currents represented by the two fluids. Externally applied fields may also be present.

The macroscopic element of each fluid is assumed to contain an arbitrarily large number of charged particles, but it is small compared to the spatial scale over which macroscopic thermodynamic or field quantity varies. The picture is meaningful if this scale is large compared to the mean-free path between particle collisions, and the Larmor radius of each particle about magnetic field lines. This is the ideal two-fluid model of plasma dynamics.

Because of the incomparable mass of electron to that of an individual ion, the contribution of the electrons to fluid inertia may be neglected. With a few additional assumptions, the system can be treated as a single fluid which responds to the Lorentz magnetic force. This is the ideal MHD model of plasma dynamics, a simplified form of the two-fluid model [42].

3.3 MHD Equations

In a single-fluid model of a fully ionized plasma, the derivation of MHD equations can be limited to the case of a hydrogen plasma, in which the ions and electrons have respective charges $\pm e$. By this assumption, charge neutrality is at least approximately satisfied, so that $n_i \approx n_e \approx n$, but the possibility of a small non-vanishing charge density will be allowed. The final equations, however, apply just as well to the case of a plasma in which the ions are multiply charged with Ze in which case the charge neutrality condition will be $n_e \approx Zn_i$. The assumption of approximate charge neutrality will be valid whenever the spatial scale lengths of the phenomena of interest greatly exceed the Debye length λ_D. The masses of the electron and ion are denoted by m and M, respectively.

The MHD model treats the plasma as a single fluid with mass density [43]

$$\rho = n_i M + n_e m \approx n\,(M + m) \approx nM \tag{3.1}$$

charge density

$$\sigma = (n_i - n_e)\, e \tag{3.2}$$

mass velocity

$$\mathbf{v} = \frac{(n_i M \mathbf{v}_i + n_e m \mathbf{v}_e)}{\rho} \approx \frac{(M\mathbf{v}_i + m\mathbf{v}_e)}{(M+m)} \approx \mathbf{v}_i + \left(\frac{m}{M}\right)\mathbf{v}_e \tag{3.3}$$

and current density:

$$\mathbf{J} = e(n_i \mathbf{v}_i - n_e \mathbf{v}_e) \approx ne(\mathbf{v}_i - \mathbf{v}_e) \tag{3.4}$$

These may be solved to obtain expressions for the ion and electron mass velocities ($\mathbf{v}_i$ and $\mathbf{v}_e$) in terms of **v** and **J**:

$$\mathbf{v}_i \approx \mathbf{v} + \frac{m}{M}\frac{\mathbf{J}}{ne} \tag{3.5}$$

$$\mathbf{v}_e \approx \mathbf{v} - \frac{\mathbf{J}}{ne} \tag{3.6}$$

where the terms that are unambiguously small in $\frac{m}{M}$ have been dropped. The single-fluid MHD equations can be derived by taking various linear combinations of the individual ion and electron equations. In particular, the two individual continuity equations

$$\frac{\partial n_{e,i}}{\partial t} + \nabla \cdot (n_{e,i}\mathbf{v}_{e,i}) = 0 \tag{3.7}$$

are multiplied by the ion and electron masses M and m, and added together to produce a mass continuity equation:

$$\frac{\partial \rho}{\partial t} + \nabla \cdot (\rho \mathbf{v}) = 0 \tag{3.8}$$

The individual continuity equations can be subtracted from one another to produce the charge continuity equation:

$$\frac{\partial \sigma}{\partial t} + \nabla \cdot \mathbf{J} = 0 \tag{3.9}$$

In a similar way, the two individual momentum balance equations or the individual fluid equations

of motion [44]

$$Mn_i\frac{d\mathbf{v}_i}{dt} = en_i(\mathbf{E}+\mathbf{v}_i\times\mathbf{B}) - \nabla p_i + \Re_{ie} \tag{3.10}$$

$$mn_e\frac{d\mathbf{v}_e}{dt} = -en_e(\mathbf{E}+\mathbf{v}_e\times\mathbf{B}) - \nabla p_e + \Re_{ei} \tag{3.11}$$

(where $\Re_{ie}$ and $\Re_{ei}$ describe collisional transfer of momentum between the two species) can be added together to produce the combined single-fluid equation of motion:

$$\rho\frac{d\mathbf{v}}{dt} = \rho\left(\frac{\partial\mathbf{v}}{\partial t}+\mathbf{v}\cdot\nabla\mathbf{v}\right) = \sigma\mathbf{E}+\mathbf{J}\times\mathbf{B}-\nabla p \tag{3.12}$$

where $p = p_e + p_i$ is the total pressure, $(\mathbf{v}\cdot\nabla\mathbf{v})$ is the convective derivative term and the collision terms cancel each other ($\Re_{ie} = -\Re_{ei}$). Although Equations 3.10, 3.11 and 3.12 have taken the electron and ion pressures (p_e and p_i, respectively) as isotropic quantities, this is not essential to the MHD model. Indeed, there are important cases where the electron pressure is isotropic, whereas the ion pressure, because of the large ion Larmor radius, must be taken as a tensor.

To obtain a second single-fluid equation from the two individual fluid equations of motion, two approximations must be considered. First, the momentum transfer from ions to electrons must be expressed in terms of the velocity difference and the resistivity η:

$$\Re_{ei} = mn\langle\nu_{ei}\rangle(\mathbf{v}_i-\mathbf{v}_e) = mn\left(\frac{\eta ne^2}{m}\right)(\mathbf{v}_i-\mathbf{v}_e) = \eta ne\mathbf{J} \tag{3.13}$$

where $\langle\nu_{ei}\rangle$ is defined as the collision frequency of electrons on ions averaged over the electron velocity distribution. Second, the electron inertia $\frac{d\mathbf{v}_e}{dt}$ can be neglected. This will be valid for sufficiently slow phenomena where electrons have the time to reach dynamical equilibrium in regard to their motion along the magnetic field, so that $\omega \ll \omega_{ce}$, where ω is the characteristic frequency of electron motion and ω_{ce} is the electron cyclotron frequency. With these two approximations, the

single-fluid electron equation of motion (Equation 3.11) can be written as:

$$\mathbf{E} + \mathbf{v}_e \times \mathbf{B} = \eta \mathbf{J} - \frac{\nabla p_e}{ne} \tag{3.14}$$

Eliminating $\mathbf{v}_e$ in Equation 3.14 using Equation 3.6 yields:

$$\mathbf{E} + \mathbf{v} \times \mathbf{B} = \eta \mathbf{J} + \frac{\mathbf{J} \times \mathbf{B} - \nabla p_e}{ne} \tag{3.15}$$

The latter equation is usually called the generalized Ohm's law for plasma. If it is important to retain the distinction between resistivity perpendicular and parallel to a magnetic field, then the scalar η can be replaced by a diagonal tensor with diagonal elements $\eta_\perp$, $\eta_\perp$ and $\eta_\parallel$ for the case where the magnetic field is in the axial direction z.

To provide a complete set of MHD equations, an equation of state must be included to describe how the plasma pressure p varies with time. The adiabatic law is often assumed as:

$$p = C\rho^\gamma \quad \Longrightarrow \quad \frac{d}{dt}\left(\frac{p}{\rho^\gamma}\right) = 0 \tag{3.16}$$

where C is a constant and $\gamma = \frac{2+N}{N}$ for an ideal gas with N degrees of freedom. However, the isothermal law, $p = n(T_e + T_i)$ with $T_{e,i} =$ constant, provides an alternative model that is sometimes more appropriate. The system of MHD equations are closed by including the four Maxwell's equations [45]:

$$\nabla \times \mathbf{B} = \mu_0 \mathbf{J} + \epsilon_0 \mu_0 \frac{\partial \mathbf{E}}{\partial t} \qquad \text{Ampere's Law} \tag{3.17}$$

$$\nabla \times \mathbf{E} = -\frac{\partial \mathbf{B}}{\partial t} \qquad \text{Faraday's Law} \tag{3.18}$$

$$\nabla \cdot \mathbf{B} = 0 \qquad \text{Gauss' Law (Magnetism)} \tag{3.19}$$

$$\nabla \cdot \mathbf{E} = \frac{\sigma}{\epsilon_0} \qquad \text{Gauss' Law (Electricity)} \tag{3.20}$$

where an external plasma polarization current is assumed, so the vacuum form for the permittivity ϵ

is used. Usually, both the displacement current $\epsilon_0 \frac{\partial \mathbf{E}}{\partial t}$ and charge density σ can be ignored in plasma physics.

3.4 MHD Equilibria

In magnetostatic plasma configuration, where the pressure is isotropic, Equation 3.12 can written as a force balance equation between the magnetic and pressure forces [46]:

$$\nabla p = \mathbf{J} \times \mathbf{B} \tag{3.21}$$

where both **v** and **E** are absent due to the static equilibrium and the negligible resistivity η. Substituting Ampere's law (Equation 3.17) into Equation 3.21 provides:

$$\nabla p = \frac{1}{\mu_0} (\nabla \times \mathbf{B}) \times \mathbf{B} \tag{3.22}$$

Using the following vector identity:

$$\nabla(\mathbf{A} \cdot \mathbf{B}) = \mathbf{A} \times (\nabla \times \mathbf{B}) + \mathbf{B} \times (\nabla \times \mathbf{A}) + (\mathbf{B} \cdot \nabla)\mathbf{A} + (\mathbf{A} \cdot \nabla)\mathbf{B} \tag{3.23}$$

the force balance equation can be reduced to:

$$\nabla p = \frac{1}{\mu_0} \left[(\mathbf{B} \cdot \nabla)\mathbf{B} - \nabla \left(\frac{B^2}{2} \right) \right] \tag{3.24}$$

Rearranging the above equation yields:

$$\nabla \left(p + \frac{B^2}{2\mu_0} \right) = \frac{1}{\mu_0} (\mathbf{B} \cdot \nabla)\mathbf{B} \tag{3.25}$$

Equation 3.25 is known as the pressure balance condition which is given in terms of the gradient of magnetic pressure $\frac{B^2}{2\mu_0}$ and the plasma pressure p. It is a nonlinear differential equation for **B** and

has to be solved together with the constraint $\nabla \cdot \mathbf{B} = 0$. The curvature term $(\mathbf{B} \cdot \nabla)\mathbf{B}$ on the right hand side comes from bending of the magnetic field that counterbalances the pressure gradient term by producing a perpendicular magnetic force.

One example of an equilibrium of this type is the cylindrical plasma with a magnetic field $B_z(r)$ directed along the axis of the cylinder (shown in Figure 3.1). In this cylindrical configuration (r, θ, z), the plasma current with radius a carries an axial current $J_z(r)$ with radial dependence. The axial current creates an azimuthal magnetic field $B_\theta(r)$ which combines with $B_z(r)$ to produce a total magnetic field $\mathbf{B} = \mathbf{B}_\theta + \mathbf{B}_z$ with helical structure. In equilibrium, the radial component of Equation 3.25 is given by [47]:

$$\frac{\partial}{\partial r}\left(p + \frac{B_\theta^2}{2\mu_0} + \frac{B_z^2}{2\mu_0}\right) = -\frac{1}{\mu_0}\frac{B_\theta^2}{r} \tag{3.26}$$

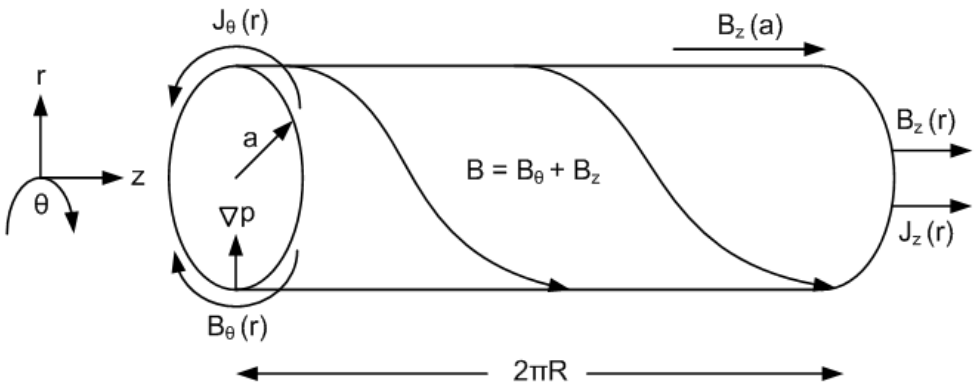

Figure 3.1: MHD equilibrium in a cylindrical plasma column.

The curvature term acts only in the azimuthal direction (θ):

$$(\mathbf{B} \cdot \nabla \mathbf{B})_r = \frac{B_\theta}{r}\frac{\partial}{\partial \theta}(B_\theta \mathbf{e}_\theta) = -\frac{B_\theta^2}{r}\mathbf{e}_r \tag{3.27}$$

where the vector identity

$$\frac{\partial \mathbf{e}_\theta}{\partial \theta} = -\mathbf{e}_r \tag{3.28}$$

has been used. The axial magnetic field B_z is absent in the curvature term because it is assumed to be straight. Rearranging Equation 3.26 leads to:

$$\frac{\partial}{\partial r}\left(p + \frac{B_z^2}{2\mu_0}\right) = -\frac{1}{2\mu_0}\frac{1}{r^2}\frac{\partial}{\partial r}(rB_\theta)^2 \tag{3.29}$$

or

$$\frac{\partial p}{\partial r} = J_\theta B_z - J_z B_\theta = -\frac{1}{\mu_0}\frac{\partial}{\partial r}\frac{B_z^2}{2} - \frac{1}{\mu_0}\frac{B_\theta}{r}\frac{\partial}{\partial r}rB_\theta \tag{3.30}$$

The equilibrium condition in the plasma column can be obtained by multiplying Equation 3.30 by r^2 and integrating over the plasma cross-section:

$$\langle p \rangle = \frac{1}{2\mu_0}\left[B_\theta^2(a) + B_z^2(a) - \langle B_z^2 \rangle\right] \tag{3.31}$$

where $\langle p \rangle$ and $\langle B_z^2 \rangle$ are given by:

$$\langle p \rangle = \frac{2\pi}{\pi a^2}\int_0^a p(r) r dr \tag{3.32}$$

$$\langle B_z^2 \rangle = \frac{2\pi}{\pi a^2}\int_0^a B_z^2(r) r dr \tag{3.33}$$

Equation 3.31 describes the force balance condition in the minor radius direction. It remains valid even when the straight discharge is weakly bent into a torus as in tokamaks. In tokamaks, the toroidal magnetic field is much larger than the poloidal field ($B_\phi \gg B_\theta$). More importantly, since the tokamak is characterized by a curvature radius R, an equilibrium condition in the major radius direction is required to maintain the balance with expansion forces that act in that direction (see Section 2.3).

3.5 Magnetic Surfaces

The topology of magnetic field lines plays a significant role in characterizing magnetic surfaces in a toroidal equilibrium configuration such as in tokamaks. Such equilibria are usually determined

by the magnetic surfaces nested around a magnetic axis. A field line running along a surface either encloses onto itself after a finite integer number of toroidal rotations around the major axis of the torus involving another integer number of poloidal rotations around the minor torus axis, or continues indefinitely filling the entire surface ergodically. The rotation of magnetic field lines inside the toroidal device is usually described by a parameter called the rotational transform angle ι [48]:

$$\iota(r) = \frac{RB_\theta(r)}{rB_\phi(r)} \tag{3.34}$$

which depends linearly on the azimuthal and toroidal magnetic field. Alternatively, the ι factor can be written as a function of two oscillation modes m and n for rational ι values:

$$\iota = \frac{n}{m} \tag{3.35}$$

where m is the poloidal mode number and n is the toroidal mode number. In tokamak physics, there is another useful quantity that characterizes the magnetic field line twist called the safety factor q which is the inverse of ι [49]:

$$q(r) = \iota^{-1}(r) = \frac{rB_\phi(r)}{RB_\theta(r)} \tag{3.36}$$

or

$$q = \frac{m}{n} \tag{3.37}$$

A contour plot can be drawn on each plasma cross-section at a fixed toroidal angle. On each cross-section, the points with a chosen q-value on such a cross-section form a closed (or open) line. A series of such lines on cross-sections at all toroidal angles form a surface termed a magnetic surface. The spatial structure of magnetic surfaces is well defined based on the values of q. For instance, by considering the case of a magnetic surface with $q = \frac{3}{2}$ as shown in Figure 3.2, the rotational configuration of the q-factor can be interpreted as the magnetic field line that starts from the point 1 rotates poloidally by $\theta = \frac{2\pi}{3}$ and toroidally by $\phi = \pi$ before it passes through the point 2. This magnetic line travels 3 times along the toroidal direction accompanied by 2 rotations in the poloidal

direction before it encloses onto itself at the point 7 which is the original starting point. The radial dependance of q indicates how the field line twist varies between different surfaces with constant radii r. This shear of the magnetic field can be derived from the q-factor as:

$$s(r) = \frac{d\ln q}{d\ln r} = \frac{r}{q}\frac{dq}{dr} \tag{3.38}$$

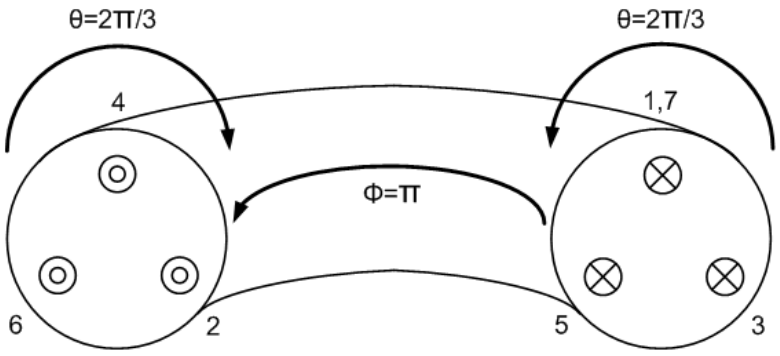

Figure 3.2: The rotational configuration of the q-factor at a rational value of $\frac{3}{2}$.

In general, q-values fall into two categories involving rational or irrational magnetic surfaces. For a magnetic surface with an irrational q-value, the magnetic lines cover a magnetic surface ergodically, so that $\iota = \lim_{m\to\infty}\frac{n}{m}$. For a surface with a rational q-value, the magnetic field lines enclose onto themselves to form a non-ergodic magnetic surface with spatial structures that are resembled by mapping the corresponding poloidal and toroidal mode numbers.

In a tokamak equilibrium, the magnetic surfaces are uniformly nested around a single magnetic axis, as shown in Figure 3.3(a). The nested magnetic surfaces are considered a particular class of MHD equilibria where the plasma pressure ∇p is balanced by the magnetic force $\mathbf{J} \times \mathbf{B}$. However, as illustrated in Figure 3.3(b), generic magnetic perturbations in tokamaks may cause the magnetic surfaces with rational values of q to break up into thin helical filaments called magnetic islands. The structure of each island rotates m toroidal and n poloidal turns around its own magnetic axis before it closes on itself [50]. The rational surfaces are also known as resonant surfaces due to the resonant interaction between the perturbations caused by (m, n) magnetic islands and the perturbed magnetic fields in tokamaks. This resonant interaction in turn creates magnetic oscillations with

patterns similar to standing waves [51].

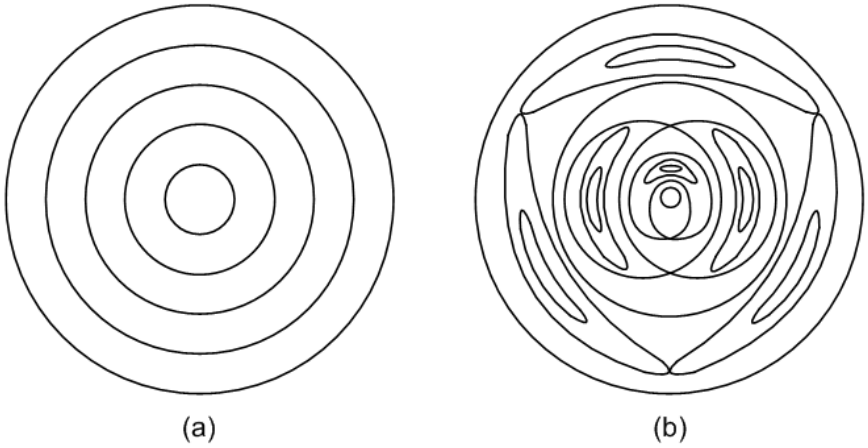

Figure 3.3: A schematic cross-section of (a) nested magnetic surfaces and (b) magnetic islands located on $q = 1$, $q = 2$ and $q = 3$ surfaces [50].

3.6 MHD Instabilities

The occurrence of MHD instabilities in tokamaks remains one of the most intensively studied topics in tokamak physics. MHD instabilities are considered dangerous phenomena because they may cause destruction of magnetic surfaces and termination of plasma discharge. However, these instabilities can be exploited to achieve quasi-stationary discharge conditions as they limit the impurity and helium ash accumulation in the plasma. MHD instabilities are well known for their macroscopic nature, for they are characterized by large spatial scales and short time scales.

From the energy principle perspective, the equilibrium of ideal MHD modes can be regarded as unstable if the perturbation works toward lowering the potential energy. The resistive MHD modes participate as well in the destabilizing process if the resistivity η is significant enough in MHD equations. Estimation of the change in potential energy can be done by introducing an arbitrary displacement $\boldsymbol{\xi}$ which is an eigenfunction describing the amount of shift in the magnetic field lines:

$$\boldsymbol{\xi} = \mathrm{Re}\left(\boldsymbol{\xi}_0 e^{i(m\theta - n\phi - \omega t)}\right) = \boldsymbol{\xi}_0 \cos(m\theta - n\phi - \omega t) \tag{3.39}$$

where ω is the angular frequency of MHD mode that grows and/or decays at rate of $i\omega$. From the linearized momentum equation, the force rising from the displacement $\boldsymbol{\xi}$ is written as [50]:

$$\mathbf{F}(\boldsymbol{\xi}) = \rho\frac{\partial^2\boldsymbol{\xi}}{\partial t^2} = \tilde{\mathbf{J}} \times \mathbf{B}_0 + \mathbf{J}_0 \times \tilde{\mathbf{B}} - \nabla\tilde{p} \tag{3.40}$$

where the indices 0 and $\sim$ describe the stable and perturbed quantities, respectively. The change in the plasma potential energy is related to the force $\mathbf{F}(\boldsymbol{\xi})$ through:

$$\Delta W = -\frac{1}{2}\int \boldsymbol{\xi}\cdot\mathbf{F}(\boldsymbol{\xi})dV = \frac{1}{2}\int\left(\frac{\tilde{B}^2}{\mu_0} + \gamma p_0(\nabla\cdot\boldsymbol{\xi})^2 + (\boldsymbol{\xi}\cdot\nabla p_0)\nabla\cdot\boldsymbol{\xi} - \mathbf{J}_0\cdot(\tilde{\mathbf{B}}\times\boldsymbol{\xi})\right)dV \tag{3.41}$$

which is integrated over the volume element dV and γ is the adiabatic index. The change in the potential energy that occurs in both the plasma and the vacuum due to the displacement ξ is readable from:

$$\Delta W = \Delta W_{\text{vacuum}} + \Delta W_{\text{plasma}} \tag{3.42}$$

where

$$\Delta W_{\text{vacuum}} = \int\left(\frac{B^2}{2\mu_0}\right)dV \tag{3.43}$$

is the energy change corresponding to the magnetic field B in vacuum. Generally, the plasma is regarded as a stable medium if the change in system energy is positive $\Delta W > 0$. The plasma is unstable if $\Delta W < 0$. From Equation 3.41, it seems that MHD instabilities can be triggered by two different sources of free energy, namely, the pressure of the plasma and the current flowing in the plasma [52]. Therefore, MHD instabilities are classified relative to their driven source into two types: pressure-driven instabilities which are proportional to the pressure gradient term ∇p_0, and current-driven instabilities correspond to the current source J_0.

Some examples of screw-type MHD instabilities that may occur in plasma are shown in Figure 3.4, where the sausage or flute instability is a typical pressure-driven instability and the kink mode is a current-driven instability. In tokamaks, the plasma is usually vulnerable to the screw-type of MHD instabilities due to the helical nature of the confining magnetic field. Therefore, a stability condition

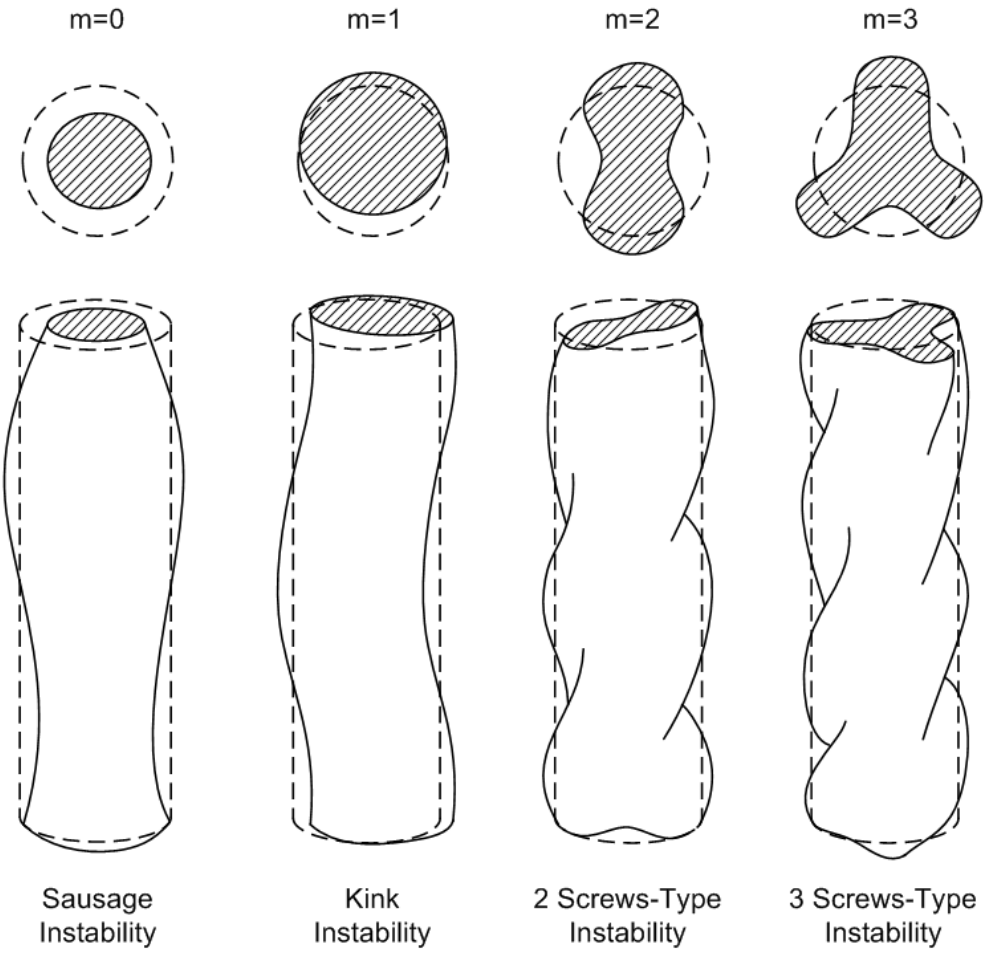

Figure 3.4: The perturbed plasma column for different values of the oscillation mode m [53].

has to be set to persist the occurrence of MHD perturbations. In practice, the safety factor q in a tokamak typically varies from about unity at the center of the plasma ($r = 0$) to three or higher at the plasma edge ($r = a$). The stability margin of screw-type MHD instabilities can be derived from the Shafranov-Kruskal criterion for a toroidal plasma cylinder [53]:

$$B_\phi > \frac{R}{a} B_\theta(a) = \frac{B_\phi}{q(a)} \tag{3.44}$$

so that:

$$q(a) = \frac{aB_\phi}{RB_\theta} > 1 \tag{3.45}$$

which describes the region of stability with respect to a screw-type perturbation. However, the

maximum plasma current allowed in a tokamak is also limited by $q(a) > 2$ or $q = 2$ MHD barrier, and unless the plasma current is ramped sufficiently, it is difficult to cross the barrier without causing a major plasma disruption [54]. Therefore, in tokamaks, the maximum plasma current is imposed by the condition $q(a) \geqslant 2$, or:

$$I_p \leqslant \frac{1}{\mu_0}\frac{\pi a^2}{R}B_\phi \tag{3.46}$$

which in turn limits the OH power. The magnetic perturbation $\tilde{\mathbf{B}}$ caused by the propagation of magnetic island at rotational frequency f on the rational magnetic surface (m, n) can be conveniently expressed by [55]:

$$\tilde{\mathbf{B}} = \tilde{\mathbf{B}}_0 e^{i(m\theta - n\phi - 2\pi f t)} \tag{3.47}$$

where $\tilde{\mathbf{B}}_0$ is the amplitude of the perturbed magnetic field.

3.7 MHD Observation in Tokamaks

MHD instabilities have been successfully observed in many experiments that were carried out in various tokamaks. The detection and interpretation of the MHD fluctuations occurring in tokamak plasma is a challenging task for plasma diagnostics. The information on these fluctuations has been retrieved mainly from the measurement of oscillating magnetic fields detected with coils situated outside the plasma (i.e. Mirnov oscillations) and the analysis of SXR signals coming from the plasma interior. Analysis of these SXR signals led to the discovery of sawtooth oscillations.

3.7.1 Mirnov Oscillations

The first systematic study of the magnetic fluctuations of the discharge plasma current has been conducted by *Mirnov* and *Semenov* in the T-3 tokamak [56]. The magnetic oscillations, or Mirnov oscillations, are fluctuations in the magnetic field of the discharge current (particularly the current near plasma boundary) which can be detected outside the plasma ring. A concept which

has proved to be of great significance for the stability of plasma in the toroidal magnetic field is that of resonance oscillations. These are oscillations where the helix of the perturbation exactly matches the helix of the confining magnetic field. The perturbed helix is described by the poloidal and toroidal mode numbers m and n.

Using the windings configuration in Figure 3.5, the magnetic island located on the surface $q = 2$ is monitored from four different poloidal angles. In this particular snapshot, the upper and lower windings act like a Rogowski coil as they detect the minimal magnetic field induced by the magnetic island which in turn generates an enclosed electric current in the helical windings labeled by I^{-}_{hel}. However, the two windings located inboard and outboard of the plasma periphery are observing the maxima of the magnetic field since they are exposed to the strong magnetic regime in the magnetic island, hence they induce a helical current with positive amplitude of I^{+}_{hel}.

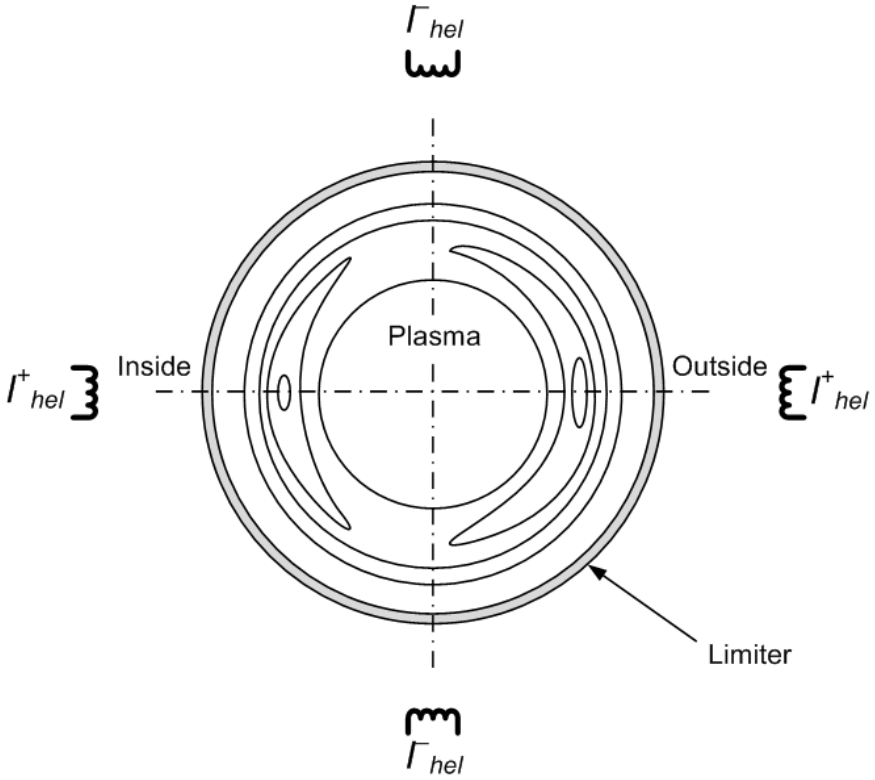

Figure 3.5: The experimental observation of a magnetic island located on the $q = 2$ profile [57].

While the magnetic island rotates half of a cycle, either clockwise or counterclockwise, the mag-

netic field passing through the vertical solenoids changes from minima to maxima and back to minima creating an amplitude oscillation in a sinusoidal waveform, so that the enclosed current alternates as $I^{-}_{\text{hel}} \rightarrow 0 \rightarrow I^{+}_{\text{hel}} \rightarrow 0 \rightarrow I^{-}_{\text{hel}}$. Although the horizontal solenoids produce the same voltage output as the vertical ones in terms of amplitude and frequency, the signals are shifted in phase by $\pm 180^{\circ}$ (for a symmetric magnetic island and identical windings) due to the monitoring of the same physical quantity from different angles [57].

3.7.2 Sawtooth Oscillations

The information concerning fluctuations in the interior of a tokamak plasma can be obtained from studying the continuous SXR emission from the plasma discharge. This radiation is produced by the thermal part of the plasma electrons and consists mainly of the bremsstrahlung and recombination radiation of partially ionized impurities. The radiation intensity will therefore sensitively depend on the electron density n_e, temperature T_e and on the concentration of impurities. In particular, perturbations in the electron density $\tilde{n}_e$ or temperature $\tilde{T}_e$ will appear in the SXR signals as sawtooth oscillations. Experimentally, sawtooth oscillations were first observed in the Princeton ST tokamak using the experimental setup shown in Figure 3.6 [58].

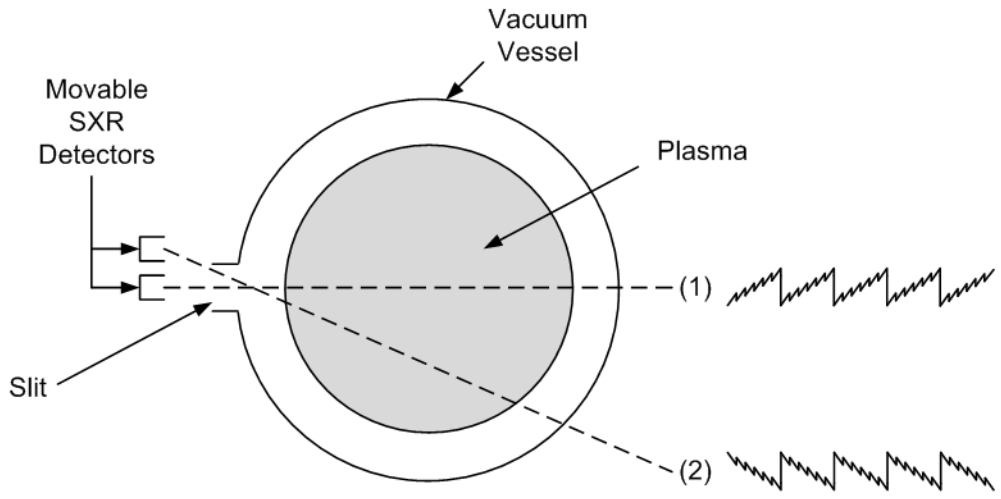

Figure 3.6: The observation of sawtooth oscillations by the SXR diagnostic. A schematic drawing of the experimental setup and the SXR signal along chords (1) and (2) [59].

The first indication of the origin of the sawtooth oscillations phenomenon comes from the sinusoidal precursor oscillation, which is sometimes superimposed on the rise phase of the sawtooth on chord (1) as shown in Figure 3.6. While the main sawtooth signal is symmetric ($m = 0$, $n = 0$), the precursor oscillation corresponds to a localized helical ($m = 1$, $n = 1$) distortion of the central plasma region, which gives rise to an oscillating signal owing to diamagnetic effects and plasma rotation. This leads to the interpretation of the sawtooth collapse (or crash phase) in terms of the internal kink instability. Since the internal kink mode is confined in a region inside the $q = 1$ surface, the injected heat flux appears just outside this surface from where it propagates further outward. This explains the inverted signal along the eccentric chord (2) shown in Figure 3.6 [60].

Chapter 4

Signal Processing Techniques

4.1 Introduction

MHD instabilities in tokamaks may simultaneously occur at different rational surfaces and rotate at either the same or different angular frequencies. Plasma diagnostics (i.e. Mirnov coils and SXR cameras) collect the spatial and temporal information of MHD perturbations at the same time. Therefore, the first step for an accurate interpretation of the output signals of plasma diagnostics is to choose proper data processing techniques. Fourier transform is considered the universal method for time to frequency domain conversion. However, due to the limitation of Fourier transform for handling non-stationary signals, alternative techniques must be utilized. For more comprehensive signal analysis, some Fourier-based techniques combined with the singular value decomposition algorithm are used for decomposing the signals that contain multiple harmonics into a thread of tempo-spatial harmonic bases.

4.2 Fourier Transform

Since the introduction of Fourier transform (FT) by *Joseph Fourier* in the early 1800's, it has been proven that FT is one of the best-known integral transforms. It has found uses in many applications and has led to the development of many other transforms. Today, FT is a fundamental

and powerful tool for signal processing. Its importance has been enhanced by the development of efficient algorithms for computing the discrete version of the FT.

In essence, FT decomposes a waveform into an infinite sum of harmonic oscillations or sinusoids at definite frequencies equal to integer multiples of the fundamental frequency (lowest non-zero frequency in the series), so FT allows an aperiodic function to be expressed as an integral sum over a continuous range of frequencies. It has the ability to distinguish the different frequency sinusoids and their respective amplitudes. If $x(t)$ represents a continuous function of a quantity in the time domain, then $x(t)$ can be mathematically expressed by an equivalent Fourier integral [61]:

$$x(t) = \int_{-\infty}^{\infty} X(f) e^{i2\pi ft} df \tag{4.1}$$

The determination of $X(f)$ represents the central problem of Fourier analysis. The function $X(f)$ is known as the FT of $x(t)$ in the frequency domain:

$$X(f) = \int_{-\infty}^{\infty} x(t) e^{-i2\pi ft} dt \tag{4.2}$$

When the independent variable t represents time in seconds, the transform variable f represents frequency in hertz. The FT is often written in terms of angular frequency $\omega = 2\pi f$ whose unit is radians per second. The substitution of $f = \frac{\omega}{2\pi}$ into the Equations 4.1 and 4.2 produces the following convention:

$$X(\omega) = \int_{-\infty}^{\infty} x(t) e^{-i\omega t} dt \qquad \text{Fourier Transform} \tag{4.3}$$

$$x(t) = \frac{1}{2\pi} \int_{-\infty}^{\infty} X(\omega) e^{i\omega t} d\omega \qquad \text{Inverse Transform} \tag{4.4}$$

This definition results in a lack of symmetry since a factor $\left(\frac{1}{2\pi}\right)$ appears in the inverse transform while it is absent in the FT itself. Symmetry in this respect may be achieved if a definition is chosen which incorporates a factor $\left(\frac{1}{\sqrt{2\pi}}\right)$ in both the transform and the inverse transform, and in

mathematics texts such a convention is common [62]:

$$X(\omega) = \frac{1}{\sqrt{2\pi}} \int_{-\infty}^{\infty} x(t) e^{-i\omega t} dt \qquad \text{Fourier Transform} \tag{4.5}$$

$$x(t) = \frac{1}{\sqrt{2\pi}} \int_{-\infty}^{\infty} X(\omega) e^{i\omega t} d\omega \qquad \text{Inverse Transform} \tag{4.6}$$

which yields a unitary transform ($x(t) \cdot X(\omega) = X(\omega) \cdot x(t) = 1$). For a real-valued function $x(t)$, FT of $x(t)$ (Equation 4.5) can be simplified into more convenient form using Euler's formula $e^{-i\omega t} = \cos(\omega t) - i \sin(\omega t)$ [63]:

$$X(\omega) = \frac{1}{\sqrt{2\pi}} \int_{-\infty}^{\infty} x(t) \cos(\omega t) dt - \frac{i}{\sqrt{2\pi}} \int_{-\infty}^{\infty} x(t) \sin(\omega t) dt \tag{4.7}$$

where the function $x(t)$ is expressed by:

$$x(t) = \frac{1}{\sqrt{2\pi}} \int_{-\infty}^{\infty} X(\omega) \cos(\omega t) d\omega + \frac{i}{\sqrt{2\pi}} \int_{-\infty}^{\infty} X(\omega) \sin(\omega t) d\omega \tag{4.8}$$

For an even function $x(t)$, the sine term in Equation 4.7 vanishes because of the symmetric integration over the interval $(-\infty, \infty)$, and the cosine term

$$X(\omega) = \sqrt{\frac{2}{\pi}} \int_{0}^{\infty} x(t) \cos(\omega t) dt \tag{4.9}$$

gives the Fourier cosine transform of $x(t)$ which can be inverted by:

$$x(t) = \sqrt{\frac{2}{\pi}} \int_{0}^{\infty} X(\omega) \cos(\omega t) d\omega \tag{4.10}$$

In similar manner, the Fourier sine transform for an odd function $x(t)$ can be obtained by setting the cosine term in Equation 4.7 to zero due to the symmetric integration around the origin:

$$X(\omega) = \sqrt{\frac{2}{\pi}} \int_{0}^{\infty} x(t) \sin(\omega t) dt \tag{4.11}$$

and the inverse sine transform is written as:

$$x(t) = \sqrt{\frac{2}{\pi}} \int_0^\infty X(\omega) \sin(\omega t) d\omega \tag{4.12}$$

The imaginary units and the negative sign in Equations 4.11 and 4.12 are omitted for more commonly seen formulae. Since digitizers used in experiments record only discrete data, numerical FT computation for discrete data points $x(t_n)$ has been developed. Correspondingly, the components of $X(\omega_k)$ (the FT of $x(t_n)$) are computed at discrete values ω_k. Therefore, for a signal $x(t_n)$ with total number of samples M and sampling time t_s, the discrete Fourier transform (DFT) can be defined as [64]:

$$X(\omega_k) = \sum_{n=0}^{M-1} x(t_n) e^{-i\frac{2\pi}{M}kn}, \quad k = 0, 1, 2, \cdots, M-1 \tag{4.13}$$

and its inverse (the IDFT) is given by:

$$x(t_n) = \frac{1}{M} \sum_{k=0}^{M-1} X(\omega_k) e^{i\frac{2\pi}{M}kn}, \quad n = 0, 1, 2, \cdots, M-1 \tag{4.14}$$

The DFT given in Equation 4.13 indicates that M complex multiplications are needed to produce one output. In order to compute M outputs, a total of approximately M^2 complex multiplications are required. A 1024-point DFT requires more than one million complex multiplications and additions. The number of DFT computations was drastically reduced when the fast Fourier transform (FFT) was introduced by *James Cooley* and *John Tukey* [65]. The FFT algorithm takes the advantage of the fact that many computations are redundant in the DFT due to the periodic nature of the twiddle factor $e^{-i\frac{2\pi}{M}}$. The ratio of computing cost in terms of the number of multiplications is approximately:

$$\frac{\text{FFT}}{\text{DFT}} = \frac{\log_2 M}{2M} \tag{4.15}$$

which equals $\frac{10}{2048}$ when M is 1024. However, the FFT algorithm is more complicated to implement than the DFT because it becomes lengthy when M is not a power of 2. This restriction on M can be overcome by appending zeros at the end of the sequence to make M become a power of 2 without

changing the spectrum of the signal. An example of how DFT converts a basic sinusoidal wave from time domain to frequency domain using FFT algorithm is shown in Figure 4.1.

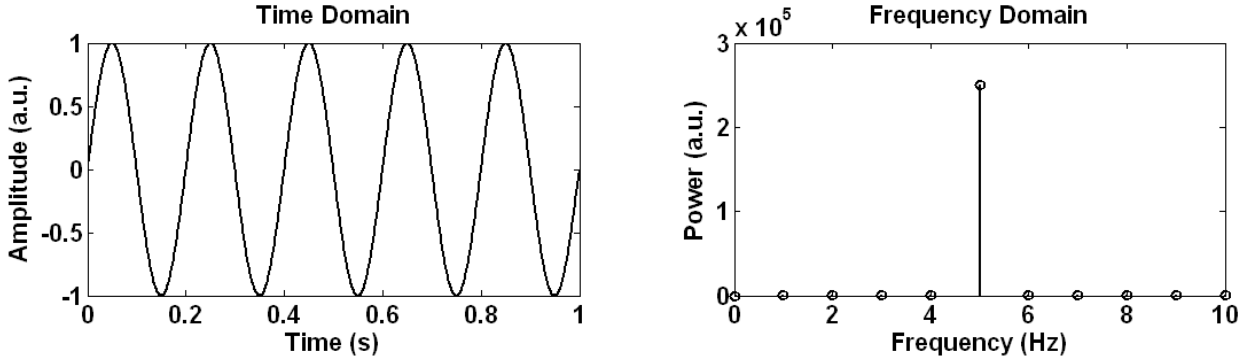

Figure 4.1: DFT was performed using FFT on a sinusoidal signal with amplitude $a = 1$, frequency $f = 5$ Hz, sampling time $t_s = 0.001$ s and $M = 1001$ sample points.

4.3 Time-Frequency Analysis

Although Fourier analysis is useful for transforming time domain signals, it is particularly poor in handling transient or non-stationary signals. The disadvantage of FT is clearly shown in Figure 4.2 as Fourier analysis produced identical power spectra for two non-identical chirp waves. The first wave is a linear up-chirping wave oscillating at incremental frequency $f_{\text{initial}} = 10$ Hz to final frequency $f_{\text{final}} = 40$ Hz, while the second wave is a linear down-chirping wave oscillating decrementally from $f_{\text{initial}} = 40$ Hz to $f_{\text{final}} = 10$ Hz.

Constructing a simultaneous time-frequency spectrum for non-stationary signal requires applying FT for a short-time window. By moving the analysis window along the signal, the variations of the signal spectrum can be tracked and captured as a function of time. Some numerical methods, namely short-time Fourier transform and wavelet transform, are based on the short-time window approach, hence they are employed for time-frequency representation analysis. A brief discussion on time-resolved frequency analysis is presented in this section.

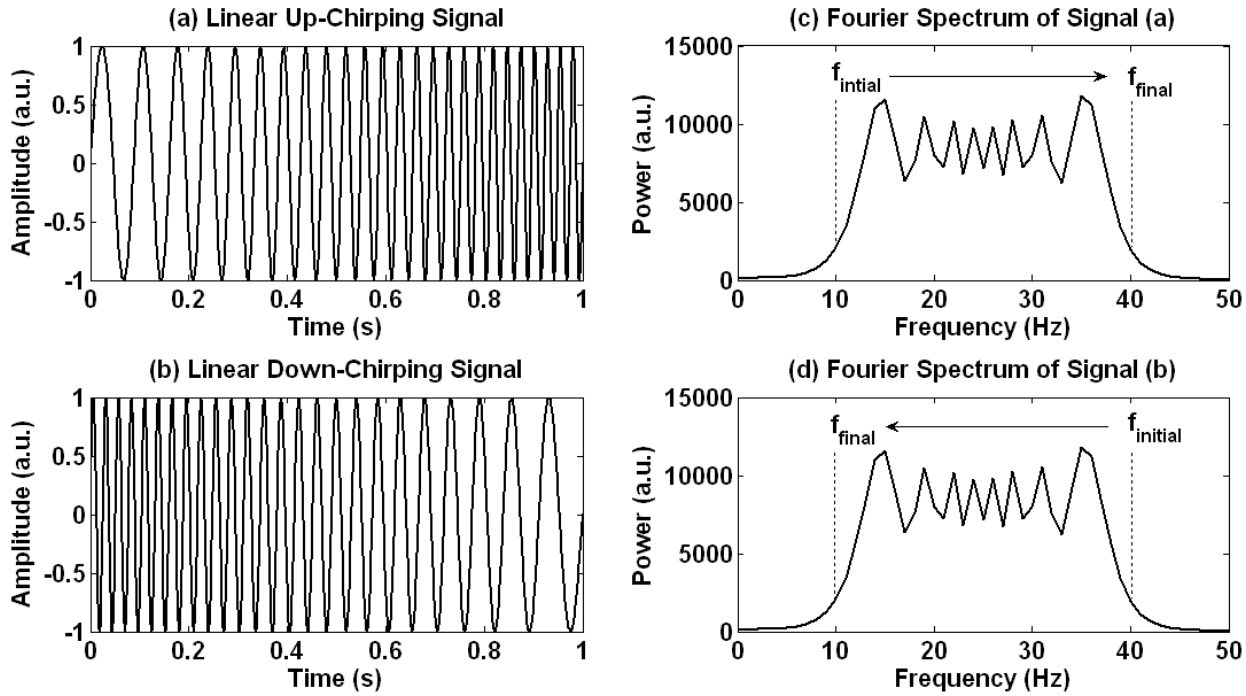

Figure 4.2: The drawback of Fourier analysis is that two different linear chirp signals (a) and (b) produce similar Fourier spectra (c) and (d).

4.3.1 Short-Time Fourier Transform

The short-time Fourier transform (STFT), or Gabor transform, is an intuitive powerful technique used for analyzing non-stationary signals by performing a time-dependent spectral analysis. A non-stationary signal is divided into a sequence of overlapped time segments (using windowing methods) in which the signal may be considered as quasi-stationary over a limited time window. This time window is swept along the signal and a time-indexed spectrum is computed using FT. The accumulation of such a spectra indicates how the spectrum is varying in time. The STFT of a continuous time signal $x(t)$ is defined by [66]:

$$\text{STFT}\{x(t)\} = X(\tau, \omega) = \int_{-\infty}^{\infty} x(t) w(t-\tau) e^{-i\omega t} dt \tag{4.16}$$

where $w(t)$ is a square integrable short-time window called the window function, which has a fixed width and is shifted along the time axis by a factor τ. The default window function that is

customarily used for computing STFT is a Hamming window centered at the zero. The Hamming window is numerically evaluated by the following equation for M number of samples [67]:

$$w(n) = 0.54 - 0.46\cos\left(\frac{2\pi n}{M-1}\right), \quad 0 \leqslant n \leqslant M-1 \tag{4.17}$$

where the window length is M.

The STFT is essentially the FT of the signal $x(t)$, a complex-valued function representing the phase and magnitude of the signal over the time and frequency plane. The localized time-frequency information can be obtained by taking the squared magnitude of $X(\tau, \omega)$ which produces the spectrogram of the signal $x(t)$:

$$\text{Spectrogram}\{x(t)\} = |X(\tau, \omega)|^2 \tag{4.18}$$

In Figure 4.3, the left diagram shows a sinusoidal wave constructed by superimposing four disjoint sinusoids which oscillate at frequencies $f_1 = 10$ Hz ($0 \leqslant$ t $<$ 0.25 s), $f_2 = 20$ Hz (0.25 s $\leqslant$ t $<$ 0.5 s), $f_3 = 30$ Hz (0.5 s $\leqslant$ t $<$ 0.75 s) and $f_4 = 40$ Hz (0.75 s $\leqslant$ t $\leqslant$ 1 s), respectively. The total number of data points is 1001. The corresponding spectrogram (shown in the right diagram) is computed by slicing up the signal into several 128-point time segments each separated by a 1 point interval to ensure smooth overlapping along the time axis.

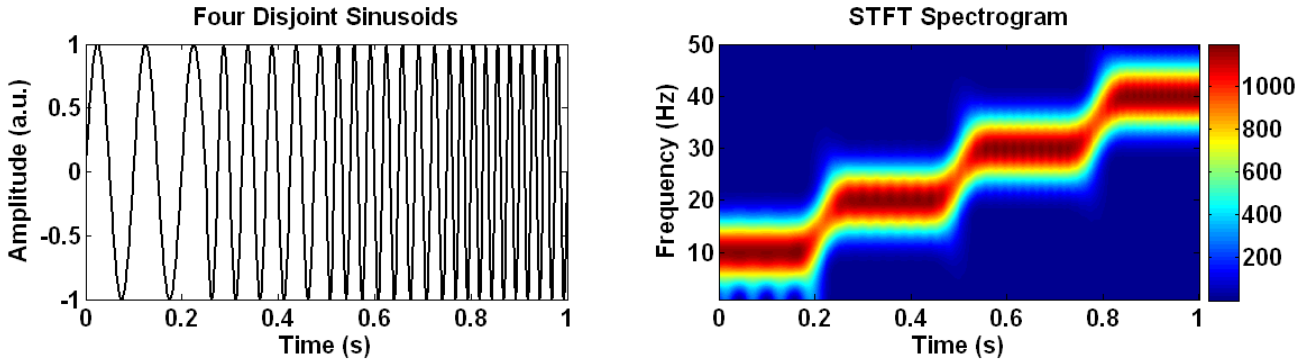

Figure 4.3: STFT power spectrum for a sinusoidal wave oscillates at four frequencies at different time windows. The spectrogram was constructed by overlapping 128-point short-time windows.

The time-frequency joint representation using STFT has an intrinsic drawback. The given time resolution Δt and frequency resolution Δf are limited in a way similar to the Heisenberg uncertainty

principle [68]:

$$\Delta t \Delta \omega \geqslant \frac{1}{2} \quad \text{or} \quad \Delta t \Delta f \geqslant \frac{1}{4\pi} \quad \text{for} \quad \omega = 2\pi f \tag{4.19}$$

Therefore, it is a practical challenge to determine the convenient window size to use for any given signal. A better solution to this time-frequency trade-off is to deploy the wavelet analysis which has the flexibility to vary the window size for the best resolution in both time and frequency. The resolution problems of STFT are clearly seen in Figure 4.4 as the sinusoidal signal is analyzed by two improper window sizes, 32-point and 512-point.

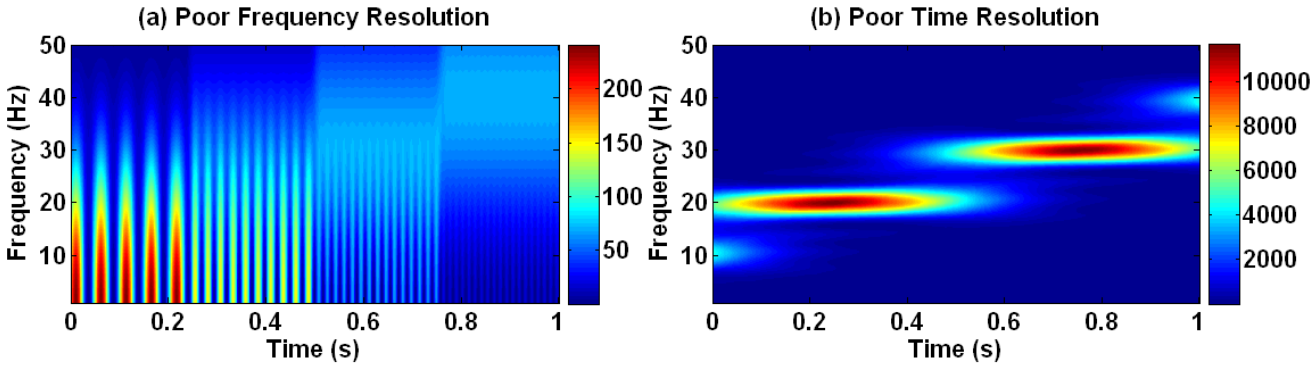

Figure 4.4: Resolution issues of STFT analysis. (a) A spectrogram of a signal indexed by a 32-point window has a good time resolution but poor frequency resolution. (b) Scanning with a 512-point window provides fine frequency resolution and poor time resolution.

4.3.2 Wavelet Transform

The fundamental idea behind the wavelet transform (WT) is based on an approach called the multiresolution analysis which provides a better solution to overcome the resolution deficiency of STFT. The WT analysis uses a fully scalable modulated window shifted along the signal, and for every time point the spectrum is calculated. This process is repeated multiple times with a slightly shorter (or longer) window for every new cycle. In the end the result will be a collection of time-frequency representations of the signal, all with different resolutions which leads to the concept of multiresolution analysis. The WT analysis described earlier is known as the continuous wavelet transform (CWT). The wavelet coefficients for a one-dimensional signal $x(t)$ are rigorously

calculated from [69]:

$$\text{CWT}\{x(t)\}(s,\tau) = \langle x(t), \psi_{s,\tau} \rangle = \int_{-\infty}^{\infty} x(t)\psi_{s,\tau}^{*}(t)dt \tag{4.20}$$

where the asterisk (*) denotes complex conjugate. The wavelet coefficients are generated from a mother wavelet $\psi(t)$ under the control of two continuous real factors $s > 0$ (scale or dilation) and τ (time or translation) which determine values on the frequency and time axes, respectively. The family of wavelet functions $\psi_{s,\tau}(t)$ (sometimes called child wavelets) is defined as translations and re-scales of the mother wavelet $\psi(t)$:

$$\psi_{s,\tau}(t) = \frac{1}{\sqrt{s}}\psi\left(\frac{t-\tau}{s}\right) \tag{4.21}$$

There is a wide variety of choices for mother wavelets. The choice of a particular mother wavelet is utterly dictated by the application of interest. For the electromagnetic signals analysis, it is preferable to choose a complex-valued mother wavelet with a simple relationship between scale and frequency. This criteria is well satisfied by the Morlet wavelet. Theoretically, the Morlet wavelet $\psi_{\text{Morlet}}(t)$, which is a modulated Gaussian function, is defined by [70]:

$$\psi_{\text{Morlet}}(t) = \frac{1}{\sqrt{\pi f_b}} e^{i2\pi f_c t - \left(\frac{t^2}{f_b}\right)} \tag{4.22}$$

which depends on the variance (or bandwidth) parameter f_b and the wavelet central frequency f_c. Although the central frequency of the Morlet wavelet has full control on time and frequency resolutions, the admissibility condition of the Morlet wavelet is verified only if $f_c > 0.8$, in Hz when the wavelet duration is in seconds, to avoid problems at low f_c (high time resolution) [71]. The waveform of the Morlet wavelet, with $f_c = 1$ Hz and unitary bandwidth f_b, is displayed in Figure 4.5 in both time and frequency domains. The FT of the Morlet wavelet $\hat{\psi}_{\text{Morlet}}(f)$ can be computed analytically from:

$$\hat{\psi}_{\text{Morlet}}(f) = e^{-\pi^2 f_b (f-f_c)^2} \tag{4.23}$$

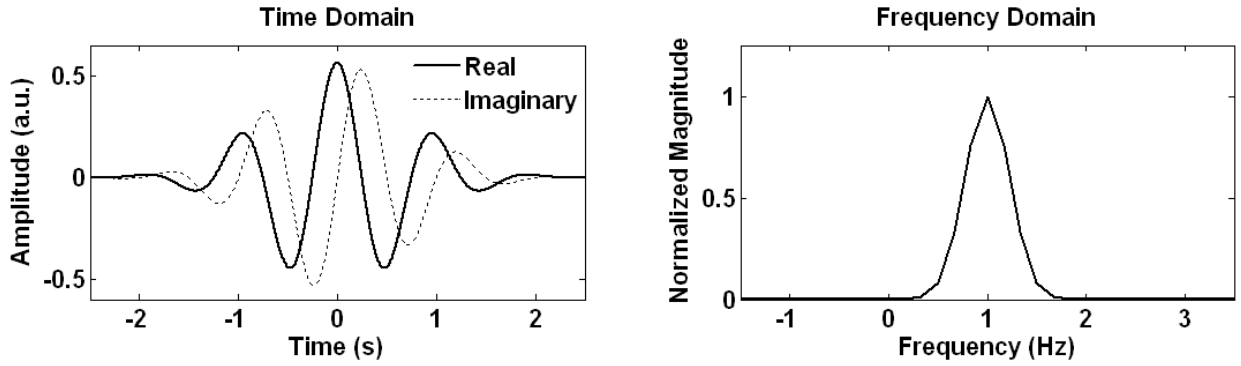

Figure 4.5: The Morlet wavelet in the time and frequency domains with a central frequency of 1 Hz and unitary variance.

Figure 4.6 shows the wavelet analysis of the same sinusoidal wave that has been analyzed earlier by STFT. The wavelet spectrum is obtained by the Morlet wavelet with central frequency 1 Hz, bandwidth parameter 10 and scales s within the range 20 (for the highest frequency 50 Hz) and 1000 (for the lowest frequency 1 Hz). The corresponding pseudo-frequencies f are related to their scaling factors s through the following relation:

$$f = \frac{f_c}{s \cdot t_s} \tag{4.24}$$

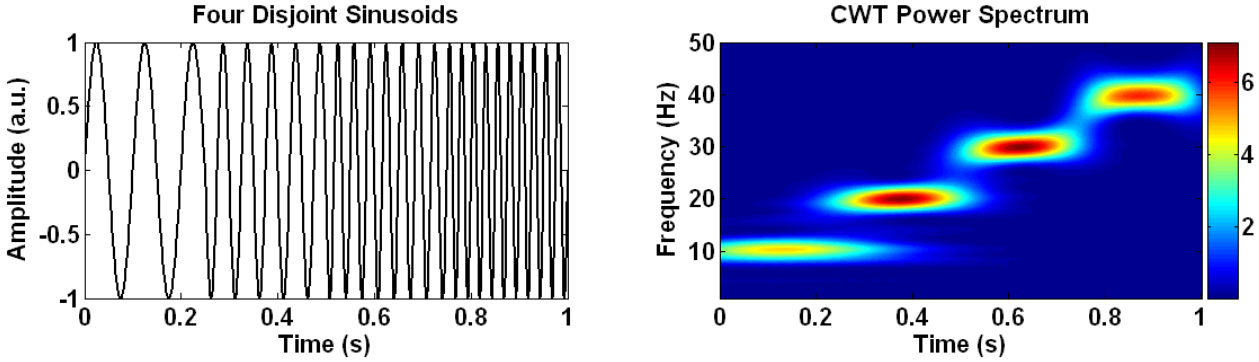

Figure 4.6: Multiresolution power spectrum of four disjoint sinusoids using the Morlet wavelet.

where t_s is the sampling period. Equation 4.24 allows the scale-frequency conversion for any frequency bandwidth $f > 0$. The scales in wavelet analysis are similar to the scales used in maps. High scales (low frequencies) correspond to a non-detailed global view of the signal, whereas

the low scales (high frequencies) provide more detailed information about the signal. In practical applications, low scales do not last the entire duration of the signal as they appear from time to time as short bursts, unlike the high scales which usually last for the entire duration of the signal [72].

4.4 Fourier Cross-Correlation Analysis

The Fourier cross-correlation (FCC) analysis requires a correlation function that is a function of either one signal (auto) or between two signals (cross). This correlation function allows the extraction of phase lag and phase correlation. The method integrates one signal (the reference signal) and another signal shifted in phase. For two functions $x_1(t)$ and $x_2(t)$ that represent signals emitted from any perturbed physical quantity monitored from different spatial points, the resultant cross-power spectrum $P_{12}(f)$ can be computed from their respective FTs $X_1(f)$ and $X_2(f)$ as [73]:

$$P_{12}(f) = \frac{1}{n}\sum_{i=1}^{n} X_{1_i}^{*}(f) X_{2_i}(f) \tag{4.25}$$

where the above spectrum is estimated by means of $X_{1_i}(f)$ and $X_{2_i}(f)$ after breaking the signals $x_1(t)$ and $x_2(t)$ into n number of realizations with equal size as follows:

$$x_1(t) = \frac{1}{n}\sum_{i=1}^{n} x_{1_i}(t) \tag{4.26}$$

$$x_2(t) = \frac{1}{n}\sum_{i=1}^{n} x_{2_i}(t) \tag{4.27}$$

Hence, the corresponding FTs $X_1(f)$ and $X_2(f)$ are readily calculated from:

$$X_1(f) = \frac{1}{n}\sum_{i=1}^{n} X_{1_i}(f) \tag{4.28}$$

$$X_2(f) = \frac{1}{n}\sum_{i=1}^{n} X_{2_i}(f) \tag{4.29}$$

Since $P_{12}(f)$ is in general complex, it can be expressed in terms of its real and imaginary parts:

$$P_{12}(f) = C_{12}(f) + iQ_{12}(f) \tag{4.30}$$

where $C_{12}(f)$ is the co-spectrum and $Q_{12}(f)$ is the quad-spectrum. Alternatively, $P_{12}(f)$ may be expressed in terms of its absolute value and phase:

$$P_{12}(f) = |P_{12}(f)|e^{i\theta_{12}(f)} \tag{4.31}$$

where $|P_{12}(f)|$ is the cross-amplitude spectrum and $\theta_{12}(f)$ is the phase spectrum:

$$\theta_{12}(f) = \frac{1}{n}\sum_{i=1}^{n}(\theta_{2_i}(f) - \theta_{1_i}(f)) = \tan^{-1}\left(\frac{Q_{12}(f)}{C_{12}(f)}\right) \tag{4.32}$$

The value of the phase spectrum for each realization at any frequency f is equal to the phase of $X_{2_i}(f)$ (denoted by $\theta_{2_i}(f)$) minus the phase of $X_{1_i}(f)$ (denoted by $\theta_{1_i}(f)$). The minus sign appears because of the complex conjugate in Equation 4.25. If $x_1(t)$ and $x_2(t)$ carry a mutual harmonic $m(f)$, the value of the cross-harmonic number can be determined by knowing the angular separation between the two signals at constant radius [74]:

$$m(f) = \frac{\theta_{12}(f)}{\Delta\theta} \tag{4.33}$$

where $\Delta\theta$ is the physical angle between $x_1(t)$ and $x_2(t)$ in radians. The auto-power spectra for $x_1(t)$ and $x_2(t)$ are respectively given by:

$$P_{11}(f) = \frac{1}{n}\sum_{i=1}^{n} X_{1_i}^*(f)X_{1_i}(f) \tag{4.34}$$

$$P_{22}(f) = \frac{1}{n}\sum_{i=1}^{n} X_{2_i}^*(f)X_{2_i}(f) \tag{4.35}$$

The auto-power spectra are real and positive, and are a measure of the power of a signal per unit bandwidth basis. Another function is the coherence spectrum which is defined in terms of the ratio of cross to auto-amplitude as follows:

$$\gamma_{12}(f) = \frac{|P_{12}(f)|}{\sqrt{P_{11}(f)P_{22}(f)}} \tag{4.36}$$

$\gamma_{12}(f)$ is simply a cross-amplitude spectrum that is normalized by the auto-power spectra of both $x_1(t)$ and $x_2(t)$. More meaningful is the interpretation of the coherence $\gamma_{12}(f)$ as the degree of cross-correlation between $x_1(t)$ and $x_2(t)$ at each frequency. While the phase information is lost in $\gamma_{12}(f)$, it is of course given by the phase spectrum $\theta_{12}(f)$ (Equation 4.32). If $\gamma_{12}(f)$ is zero at a particular frequency, then $x_1(t)$ and $x_2(t)$ are incoherent at that frequency. If on the other hand $\gamma_{12}(f) = 1$, $x_1(t)$ and $x_2(t)$ are coherent. For intermediate values, $0 < \gamma_{12}(f) < 1$, $x_1(t)$ and $x_2(t)$ are said to be partially coherent.

4.5 Fourier Coefficient Decomposition

The Fourier coefficient decomposition (FCD) is a technique based on the computations of Fourier sine and cosine coefficients for sampled finite data sets. Because of the finite duration and the discrete nature of the data, much can be gained by reformulating the Fourier sine and cosine transforms given in Equations 4.9 and 4.11 to the Fourier series. If the function $x(t)$ represents any quantity that varies with time, then $x(t)$ can be decomposed into an infinite sum of harmonic components m at multiples of the fundamental angular frequency ω. $x(t)$ may be expressed mathematically by Fourier series expansion as [75]:

$$x(t) = \frac{C_0}{2} + \sum_{m=1}^{\infty} [C_m \cos(m\omega t) + S_m \sin(m\omega t)] \tag{4.37}$$

The coefficients C_0, C_m and S_m represent the amplitudes of the m^{th} harmonic. The Fourier coefficients can be evaluated by performing the following integration over an arbitrary periodic interval

$(-p, p)$:

$$
\begin{aligned}
C_0 &= \frac{1}{p}\int_{-p}^{p} x(t)dt \\
C_m &= \frac{1}{p}\int_{-p}^{p} x(t)\cos\frac{m\pi t}{p}dt \\
S_m &= \frac{1}{p}\int_{-p}^{p} x(t)\sin\frac{m\pi t}{p}dt
\end{aligned}
\tag{4.38}
$$

where C_0 is the cosine coefficient at $m = 0$ (also referred to as the mean value or DC level), while both C_m and S_m are the cosine and sine coefficients of $m \geqslant 1$. The sine coefficient S_0 at $m = 0$ is zero as $\sin(0) = 0$, and the substitution for ω by $\frac{2\pi}{2p}$ has been used. However, for an aperiodic function $x(t)$, the corresponding Fourier series can be reduced to half-ranged expansion within the interval (0, p). In the case when $x(t)$ is an even function, all the sine coefficients S_m are zeros. When $x(t)$ is an odd function, the cosine coefficients C_m are given by zeros. Furthermore, if the periodic extension of $x(t)$ happens to be neither even nor odd, then the Fourier coefficients can be expressed by:

$$
\begin{aligned}
C_0 &= \frac{2}{p}\int_{0}^{p} x(t)dt \\
C_m &= \frac{2}{p}\int_{0}^{p} x(t)\cos\frac{m\pi t}{p}dt \\
S_m &= \frac{2}{p}\int_{0}^{p} x(t)\sin\frac{m\pi t}{p}dt
\end{aligned}
\tag{4.39}
$$

which provide the sine and cosine series of $x(t)$ over the region of interest (0, p). For more practical use of FCD analysis, if any discrete signal $x(\theta, t)$ carries spatial harmonics m and is observed from

N equidistant angles, then the Fourier coefficients in Equation 4.39 can be altered to [76]:

$$
\begin{aligned}
C_0(t) &= \frac{2}{N}\sum_{i=1}^{N} x(\theta_i, t) \\
C_m(t) &= \frac{2}{N}\sum_{i=1}^{N} x(\theta_i, t)\cos m\theta_i \\
S_m(t) &= \frac{2}{N}\sum_{i=1}^{N} x(\theta_i, t)\sin m\theta_i
\end{aligned} \tag{4.40}
$$

where $x(\theta_i, t)$ is the signal recorded at the angular location $\theta_i = i\left(\frac{2\pi}{N}\right)$. Equation 4.37 can be re-written as:

$$
x(\theta, t) = \frac{C_0(t)}{2} + \sum_{m=1}^{N/2} \left[C_m(t)\cos(m\theta) + S_m(t)\sin(m\theta)\right] \tag{4.41}
$$

Further mathematical manipulation yields:

$$
x(\theta, t) = \frac{C_0(t)}{2} + \sum_{m=1}^{N/2} \left[b_m(t)\cos(m\theta - \phi_m(t))\right] \tag{4.42}
$$

where $b_m(t)$ and ϕ_m are defined as the corresponding modulus and phase of the m^{th} harmonic, which can be computed from:

$$
b_m(t) = \sqrt{C_m^2(t) + S_m^2(t)} \tag{4.43}
$$

$$
\phi_m(t) = \tan^{-1}\left(\frac{S_m(t)}{C_m(t)}\right) \tag{4.44}
$$

4.6 Singular Value Decomposition

Singular value decomposition (SVD) is a powerful linear algebra algorithm commonly used for matrix computations, harmonic analysis, statistics and signal processing. The SVD algorithm has the ability to extract the dominant features and coherent structures by calculating eigenvectors and eigenvalues of a covariance matrix for any data matrix. This technique can be also utilized to filter out the uncorrelated noisy data [77]. Any $M \times N$ matrix $\mathbf{A}$, where $M(\text{number of rows}) \geqslant$

N(number of columns), can be depicted as factorization of three matrices $\mathbf{A} = \mathbf{USV}^T$, where $\mathbf{U}$ is an $M \times N$ column-orthogonal matrix, $\mathbf{S}$ is an $N \times N$ diagonal matrix and $\mathbf{V}^T$ is the transpose of $\mathbf{V}$, an $N \times N$ orthogonal matrix. Hence, the matrix $\mathbf{A}$ can be expressed by [78]:

$$\mathbf{A} = \begin{pmatrix} a_{11} & \cdots & a_{1N} \\ a_{21} & \cdots & a_{2N} \\ \vdots & \ddots & \vdots \\ a_{M1} & \cdots & a_{MN} \end{pmatrix} = \begin{pmatrix} u_{11} & \cdots & u_{1N} \\ u_{21} & \cdots & u_{2N} \\ \vdots & \ddots & \vdots \\ u_{M1} & \cdots & u_{MN} \end{pmatrix} \cdot \begin{pmatrix} s_{11} & \cdots & 0 \\ \vdots & \ddots & \vdots \\ 0 & \cdots & s_{NN} \end{pmatrix} \cdot \begin{pmatrix} v_{11} & \cdots & v_{1N} \\ \vdots & \ddots & \vdots \\ v_{N1} & \cdots & v_{NN} \end{pmatrix}^T \tag{4.45}$$

This notation is called the reduced SVD. There is another widely applicable notation called the full SVD which decomposes the matrix $\mathbf{A}$ into the same matrix expression $\mathbf{USV}^T$ but with slightly different dimensions. The matrix $\mathbf{U}$ is produced as an $M \times M$ orthogonal matrix, the matrix $\mathbf{S}$ is defined as an $M \times N$ diagonal matrix, and the orthogonal matrix $\mathbf{V}^T$, the transpose matrix of $\mathbf{V}$, is an $N \times N$ matrix [79]. The full expansion of $\mathbf{A}$ is given by:

$$\mathbf{A} = \begin{pmatrix} a_{11} & \cdots & a_{1N} \\ a_{21} & \cdots & a_{2N} \\ \vdots & \ddots & \vdots \\ a_{M1} & \cdots & a_{MN} \end{pmatrix} = \begin{pmatrix} u_{11} & u_{12} & \cdots & u_{1M} \\ u_{21} & u_{22} & \cdots & u_{2M} \\ \vdots & \vdots & \ddots & \vdots \\ u_{M1} & u_{M2} & \cdots & u_{MM} \end{pmatrix} \cdot \begin{pmatrix} s_{11} & \cdots & 0 \\ \vdots & \ddots & \vdots \\ 0 & \cdots & s_{NN} \\ \vdots & \ddots & \vdots \\ 0 & \cdots & 0 \end{pmatrix} \cdot \begin{pmatrix} v_{11} & \cdots & v_{1N} \\ \vdots & \ddots & \vdots \\ v_{N1} & \cdots & v_{NN} \end{pmatrix}^T \tag{4.46}$$

Regardless of notations, the columns $u^{(j)}$ of $\mathbf{U}$ are computed by normalizing eigenvectors of matrix $\mathbf{AA}^T$ which is the time-covariance matrix of $\mathbf{A}$. The columns $v^{(j)}$ of $\mathbf{V}$ can be calculated similarly from the normalized eigenvectors of $\mathbf{A}^T\mathbf{A}$, the space-covariance of $\mathbf{A}$ [80]. Moreover, $\mathbf{U}$ and $\mathbf{V}$ have orthogonal columns, so that $\mathbf{U}^T\mathbf{U} = \mathbf{I}$ and $\mathbf{V}^T\mathbf{V} = \mathbf{I}$, where $\mathbf{I}$ is the unitary matrix.

For signal processing applications, the column vectors of $\mathbf{V}$ are called principal axes (PAs) or Topos which carry the spatial information about the signal components. The projections of $\mathbf{A}$ along $\mathbf{U}$ (the product of $\mathbf{US}$) is called the matrix of principal components (PCs) or Chronos [81], and its

columns give the time evolution of the corresponding principal axis. For the diagonal matrix **S**, its elements s_i, or singular values (SVs), represent the square root of non-zero eigenvalues obtained from solving $\mathbf{A}\mathbf{A}^T$ or $\mathbf{A}^T\mathbf{A}$ (they produce the same non-zero eigenvalues). The SVs are stored in descending order proportional to the amplitude of the components corresponding to both the temporal-column vectors of **U** and the spatial-column vectors of **V**.

After proposing the SVD algorithm for plasma data analysis [82], the algorithm was adopted in the early 90's as an alternative to the conventional Fourier-based techniques to analyze the features of MHD data in both the space and time domains. The time series of magnetic oscillations recorded by a set of magnetic probes or the signals collected by the SXR cameras at different locations can form the matrix **A** which can be analyzed by SVD [83]. The output of SVD analysis can be examined by assuming a simple sinusoidal signal representing a traveling wave in a form $x(\theta, t) = \cos(m\theta - 2\pi ft)$. If this wave $x(\theta, t)$ contains a spatial harmonic m and is detected at N equidistant angles (i.e. $\theta_j = \frac{2\pi(j-1)}{N}$), then the data matrix of $x(\theta, t)$ can be written in the form:

$$X_{ij} = \frac{1}{\sqrt{M}} \cos\left[\frac{2\pi m}{N}(j-1) - 2\pi f t_s(i-1)\right] \tag{4.47}$$

where the row index i denotes time series and the column index j corresponds to a specific observation angle. For practical purposes, the time series M is sampled every t_s with an additional normalization factor $\frac{1}{\sqrt{M}}$. Equation 4.47 generates a set of data arranged in the rectangular matrix **X** having dimensions $M \times N$:

$$\mathbf{X} = \frac{1}{\sqrt{M}} \begin{pmatrix} x_1(0) & \cdots & x_N(0) \\ \vdots & \ddots & \vdots \\ x_1((M-1)t_s) & \cdots & x_N((M-1)t_s) \end{pmatrix} \tag{4.48}$$

Factorizing **X** using SVD decomposes the spatial mode m into its cosine and sine bases which are illustrated by a dominant pair of SVs with equal values $\frac{\sqrt{N}}{2}$. The spatial structure of m is carried within the first two PAs which also correspond to the Fourier bases. Those PAs differ only in the

phase; one lags behind the other by an angle $\frac{\pi}{2}$, with degeneracy:

$$v_i^{(1)} = \sqrt{\frac{2}{N}} \cos\left[\frac{2\pi m}{N}(i-1)\right]$$
$$v_i^{(2)} = \sqrt{\frac{2}{N}} \sin\left[\frac{2\pi m}{N}(i-1)\right] \tag{4.49}$$

The corresponding PCs divided by their SVs behave similarly to PAs as the first two PCs degenerately lag each other due to the phase difference:

$$u_i^{(1)} = \sqrt{\frac{2}{M}} \cos\left[2\pi f t_s(i-1)\right]$$
$$u_i^{(2)} = \sqrt{\frac{2}{M}} \sin\left[2\pi f t_s(i-1)\right] \tag{4.50}$$

In the presence of two or more harmonic modes, the data matrix X_{ij} can be constructed similarly from Equation 4.47 with additional modes m_l, frequencies f_l and amplitude coefficients a_l:

$$X_{ij} = \frac{1}{\sqrt{M}} \sum_l a_l \cos\left[\frac{2\pi m_l}{N}(j-1) - 2\pi f_l t_s(i-1)\right] \tag{4.51}$$

Each mode m_l with frequency f_l contributes with a pair of SVs equal to $\frac{\sqrt{N}a_l}{2}$. The numerical factor $\sqrt{N}$ appears in SVs because Equation 4.51 is only normalized by $\frac{1}{\sqrt{M}}$. The amplitude coefficients a_l can be obtained directly from SVs by normalizing the wave equation over $\frac{1}{\sqrt{MN}}$. Most of the SVs are very small compared to a few dominant ones, hence can be regarded as noise. On that basis, SVD can be utilized for filtering out the undesirable noisy components from signals.

Chapter 5

Experimental Setup

5.1 Introduction

MHD instabilities are monitored in STOR-M using two main diagnostics, Mirnov coils and SXR cameras. Mirnov $m = 2$ and $m = 3$ coils have been used previously for measuring MHD magnetic fluctuations. Mirnov $m = 2$ and $m = 3$ coils measure only particular modes and each mode requires a set of coils distributed at various poloidal angles. In this research project, new external magnetic probes called discrete Mirnov coils were fabricated, calibrated, installed and used. This chapter depicts the configuration of Mirnov $m = 2$ and $m = 3$ coils and the new discrete Mirnov arrays. The general layout of the SXR system that has been installed on the STOR-M tokamak will also be described.

5.2 Mirnov Coils

In the early attempts to monitor MHD activities in STOR-M plasma, two sets of coils with a variable winding density n and flexible former were constructed. The coils were installed around the vacuum chamber in the poloidal direction. These coils, called Mirnov $m = 2$ and $m = 3$ coils, are used in STOR-M for MHD studies. Mirnov coils are essentially a magnetic pick-up loop with a specific spatial windings arrangement. The resulting output signal is sensitive predominantly to a

magnetic island with specific spatial mode structure.

As shown in Figure 5.1(a), the Mirnov $m = 2$ coil consists of four uniform coils arranged poloidally 90° apart and connected in series with different polarities. The Mirnov $m = 3$ coil has a slightly different windings arrangement as it consists of six coils poloidally separated by 60° with polarities shown in Figure 5.1(b). Each of the Mirnov $m = 2$ and $m = 3$ windings has 200 turns of 30 AWG magnet wire with dimensions of $4 \times 2.5 \times 0.25$ cm^3. Mirnov $m = 2$ and $m = 3$ coils are wound on an open-ended Teflon frame with a perimeter of 108 cm which provides good flexibility for easy mounting on the 0.5 mm stainless steel bellows (see Figure 5.4).

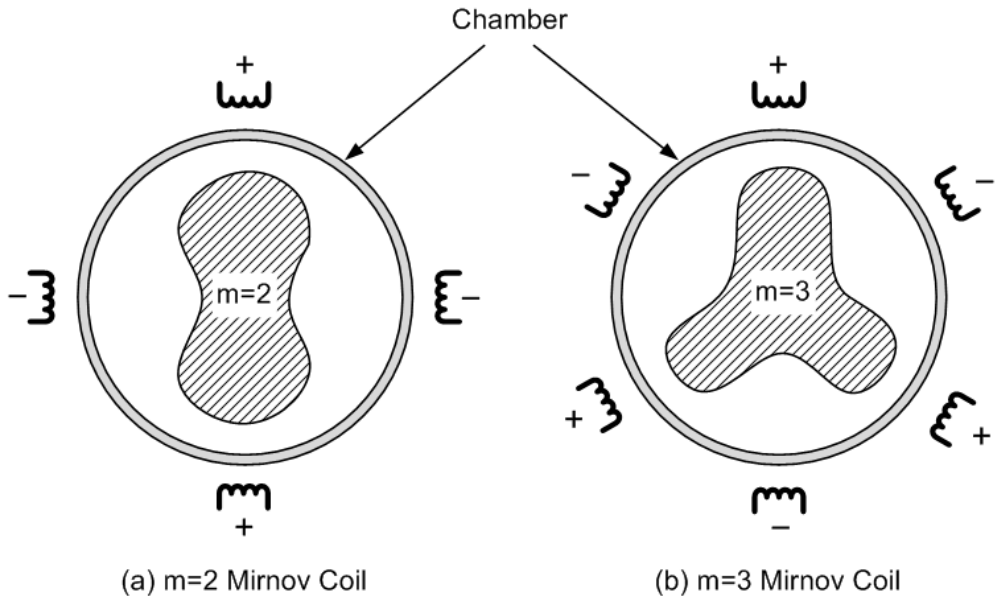

Figure 5.1: The schematic layout of Mirnov $m = 2$ and $m = 3$ coils. The boundary of the shaded area indicates the angular distribution of the fluctuating magnetic field at a particular time.

According to the windings distribution shown in Figure 5.2, it can be seen that Mirnov $m = 2$ and $m = 3$ coils are designed to respond mainly to the perturbations in the poloidal magnetic field B_θ which may be caused by the $m = 2$ and $m = 3$ oscillating modes. Recalling Equation 4.41 for the Fourier series expansion, the perturbed magnetic field $\tilde{B}_\theta(\theta, t)$ detected at N equidistant poloidal angles can be written as a sum of poloidal Fourier harmonics [84]:

$$\tilde{B}_\theta(\theta, t) = \frac{C_0(t)}{2} + \sum_{m=1}^{N/2} [C_m(t)\cos(m\theta) + S_m(t)\sin(m\theta)] \tag{5.1}$$

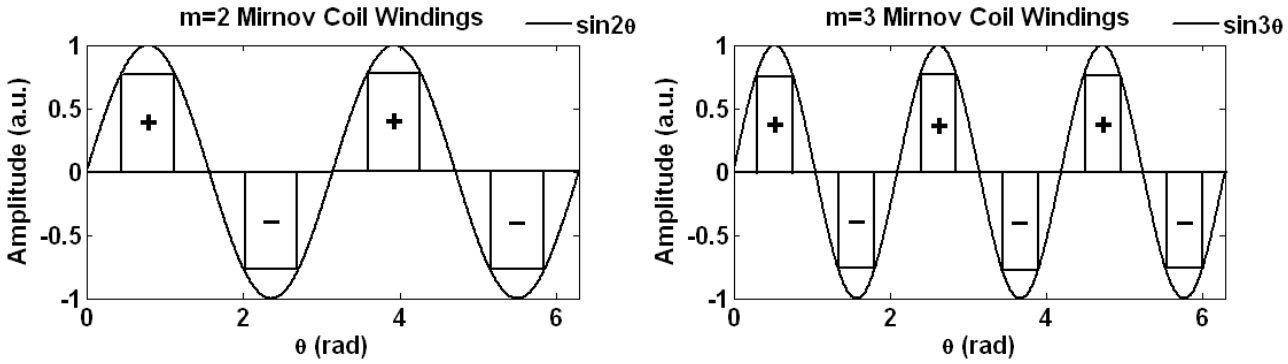

Figure 5.2: $\sin(m\theta)$ windings distribution of Mirnov $m = 2$ and $m = 3$ coils.

where the factor $\frac{C_0(t)}{2}$ associates with the magnetic field changing uniformly in all poloidal locations ($m = 0$ mode). In the case of the Mirnov $m = 2$ coil, the coefficients correspond to the following spatial Fourier components of the perturbed magnetic field $\tilde{B}_\theta(\theta, t)$:

$$C_{m=2}(t) = \frac{1}{\pi}\int_0^{2\pi} \tilde{B}_\theta(\theta, t)\cos(2\theta)d\theta$$
$$S_{m=2}(t) = \frac{1}{\pi}\int_0^{2\pi} \tilde{B}_\theta(\theta, t)\sin(2\theta)d\theta \tag{5.2}$$

Similarly, the Fourier coefficients of the Mirnov $m = 3$ coil are calculated with the following expressions:

$$C_{m=3}(t) = \frac{1}{\pi}\int_0^{2\pi} \tilde{B}_\theta(\theta, t)\cos(3\theta)d\theta$$
$$S_{m=3}(t) = \frac{1}{\pi}\int_0^{2\pi} \tilde{B}_\theta(\theta, t)\sin(3\theta)d\theta \tag{5.3}$$

The magnetic coils respond only to a time-varying magnetic field. If the winding density of an m coil is $n(\theta) = n_0\sin(m\theta)$ or $n(\theta) = n_0\cos(m\theta)$, the output voltage of either Mirnov $m = 2$ or $m = 3$ coils can be calculated from [85]:

$$V = \int \dot{\tilde{B}}_\theta An(\theta)r_s d\theta = An_0 r_s \int \dot{\tilde{B}}_\theta \begin{pmatrix}\cos(m\theta)\\ \sin(m\theta)\end{pmatrix} d\theta = An_0 r_s \begin{cases} \dot{C}_m & \cos(m\theta)\text{ Windings} \\ \dot{S}_m & \sin(m\theta)\text{ Windings}\end{cases} \tag{5.4}$$

where A is the winding surface, n is the winding density and r_s is the radial location where the Mirnov coils are placed. There are some drawbacks associated with these conventional Mirnov coils. For example, the windings configuration limits their measurements to detect only $m = 2$ or $m = 3$ modes. They can not sense any other modes with higher or lower numbers. Also, they can not detect non-rotating magnetic perturbation. In addition, the uniformity of the windings distribution of Mirnov $m = 2$ and $m = 3$ coils is meant for monitoring magnetic islands with symmetric and uncoupled spatial structures, which is not always the case for the magnetic islands observed in tokamaks particularly when the islands lock on the same frequency. Therefore, because of the drawbacks of measurements using Mirnov $m = 2$ and $m = 3$ coils, small winding sets called discrete Mirnov coils have been adopted as an alternative approach to study MHD mode numbers in the STOR-M tokamak.

5.3 Discrete Mirnov Coils

5.3.1 Coils Layout

To carry out MHD studies in the STOR-M tokamak, 32 discrete Mirnov coils were fabricated and divided to four arrays. The four arrays of Mirnov coils are located at four different toroidal locations on the STOR-M tokamak as illustrated in Figure 5.3(a). Each Mirnov coil consists of 200 turns (30 AWG magnet wire) wound on a teflon strip with a cross-section of 3 $\times$ 0.25 cm^2. The teflon strip is 108 cm long, corresponding to the circumference of a circle with a radius of 17.2 cm. Each Mirnov coil is approximately 1 cm long, corresponding to an angular spread of 3.3°. There are 12 coils for array 1 and array 2 as it is shown in Figure 5.3(b). The coils are distributed at the poloidal angles

$$\theta_{i+1} = 360^\circ - (2i + 1) \times 15^\circ, \quad i = 0, 1, \cdots, 11 \tag{5.5}$$

with $\theta = 0^\circ$ positioned at the outer mid-plane of the vacuum vessel. The poloidal arrays 1 and 2 are used for the poloidal mode identification. These two arrays are able to detect MHD poloidal

mode numbers up to 6 (total number of coils$/2$) since the maximum mode number detected by the arrays is bounded by the Nyquist criterion [86]. The criterion emphasizes that the maximum spatial resolution of a 12-coil array can only resolve the sine or cosine Fourier component of the $m = 6$ mode, depending on the waveform of the carrier signal.

The remaining 8 coils are wound on another two arrays, 4 coils for each array. The coils are poloidally separated by 90° and installed at the poloidal angles 75°, 165°, 255° and 345° as shown in Figure 5.3(c). Poloidal arrays 3 and 4 are capable of measuring poloidal mode numbers up to 2. The outboard coils (coil 1 in each of the poloidal arrays) are employed to form a 4-coil toroidal array for toroidal MHD measurements. The toroidal modes $n = 1$ and $n = 2$ are usually the dominant modes in STOR-M. These modes can be identified by the toroidal array at any fixed poloidal angle although the outboard coils of the poloidal arrays are more often used than others.

Arrays 1 and 2 are installed around the 0.5 mm stainless steel bellows which are located at the toroidal angles 0° and 180°. The arrays 3 and 4 are mounted on the thick wall of the vacuum chamber with a thickness of 4 mm and are 90° apart from the bellows. The collected signals are transmitted from the Mirnov arrays 1 and 2 to an aluminium break-out box via a 1.5 m flat-twisted ribbon cable. 34-pin connectors are used (only 24 pins are actually in use). From the break-out box, the Mirnov signals are sent across the tokamak room to a multichannel data acquisition system through 50 Ω coaxial cables which are $10 \sim 20$ m in length.

The data acquisition system (DAS) consists of 5 National Instruments digitizer cards (NI PXI-6133) each with 14-bit resolution. There are 8 analog input channels for each card. The maximum sampling rate is 3 MS$/$s per channel [87]. The output signals from arrays 3 and 4 are delivered similarly to the DAS except the arrays are connected directly to the coaxial cables without the break-out stage. Figure 5.4 shows the actual mount of the Mirnov arrays on the bellows and vacuum chamber of the STOR-M tokamak.

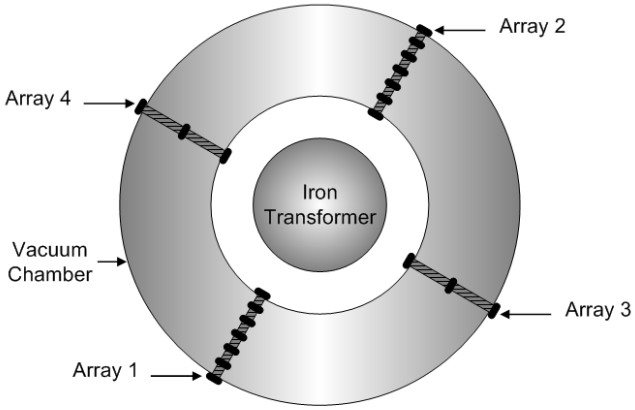

(a) Top view of the STOR-M tokamak showing the locations of Mirnov arrays.

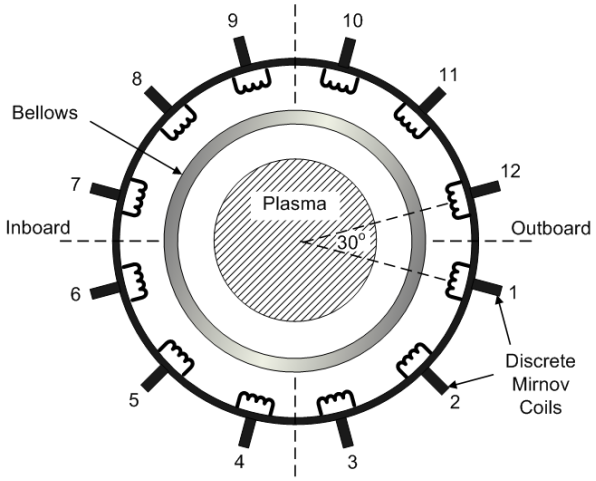

(b) Coils configuration of arrays 1 and 2.

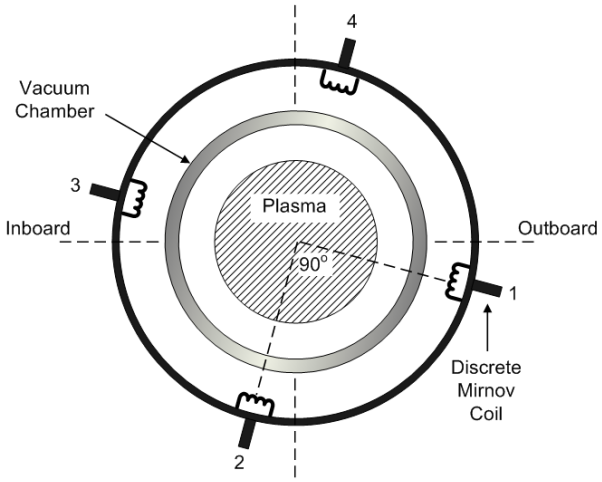

(c) Coils configuration of arrays 3 and 4.

Figure 5.3: The arrangement of discrete Mirnov coils in the STOR-M tokamak.

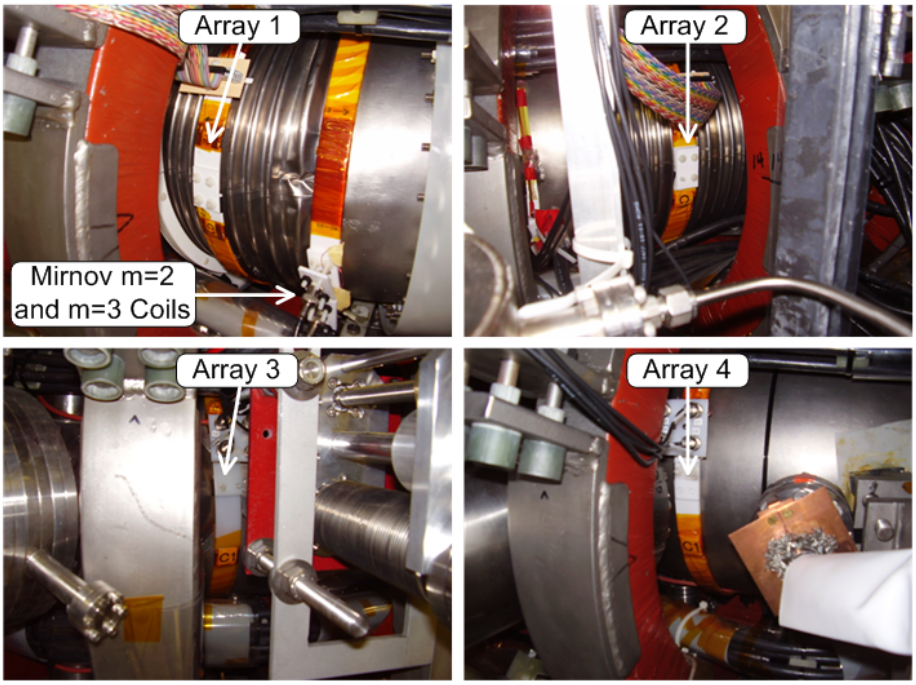

Figure 5.4: Photographs of the Mirnov arrays mount on the STOR-M tokamak.

5.3.2 Signal Transmission

To ensure a smooth transmission for the Mirnov signals from the coils to the digitizers, impedance matching between the Mirnov coils and the DAS is needed to avoid any reflection in the transmitted signals. The reflection can be minimized by soldering matching resistors in parallel at both ends of the transmission line (i.e. coaxial cable). The quality of the output signal was examined at the coil end by placing a resistor with resistance varying from 50 Ω to 1.2 kΩ parallel to the Mirnov coils. The signal was intact from any noticeable reflection while bench testing the coils. This result is expected since the coil itself has a low impedance. Finally, a set of 50 Ω resistors were soldered on the outlet BNC connectors at the Mirnov coils side. However, because the DAS has relatively high resistance ($\sim$ 1 MΩ), it was necessary to terminate the signals by 50 Ω resistors installed parallel to the digitizers to avoid any potential reflection in the signals. The importance of terminating the signals at the DAS side is illustrated in Figure 5.5. In this figure, the top Mirnov signal is terminated by a 50 Ω resistor while the bottom signal is connected to the digitizers without any termination stage. The WT spectrum of the first signal indicates no reflection in the signal.

However, a significant reflection is inflicted on the second signal which can be identified by the distortion of the signal and the presence of frequency noise in the WT spectrum. The circuit used for achieving the required impedance matching between the discrete Mirnov coils and the digitizers is shown in Figure 5.6.

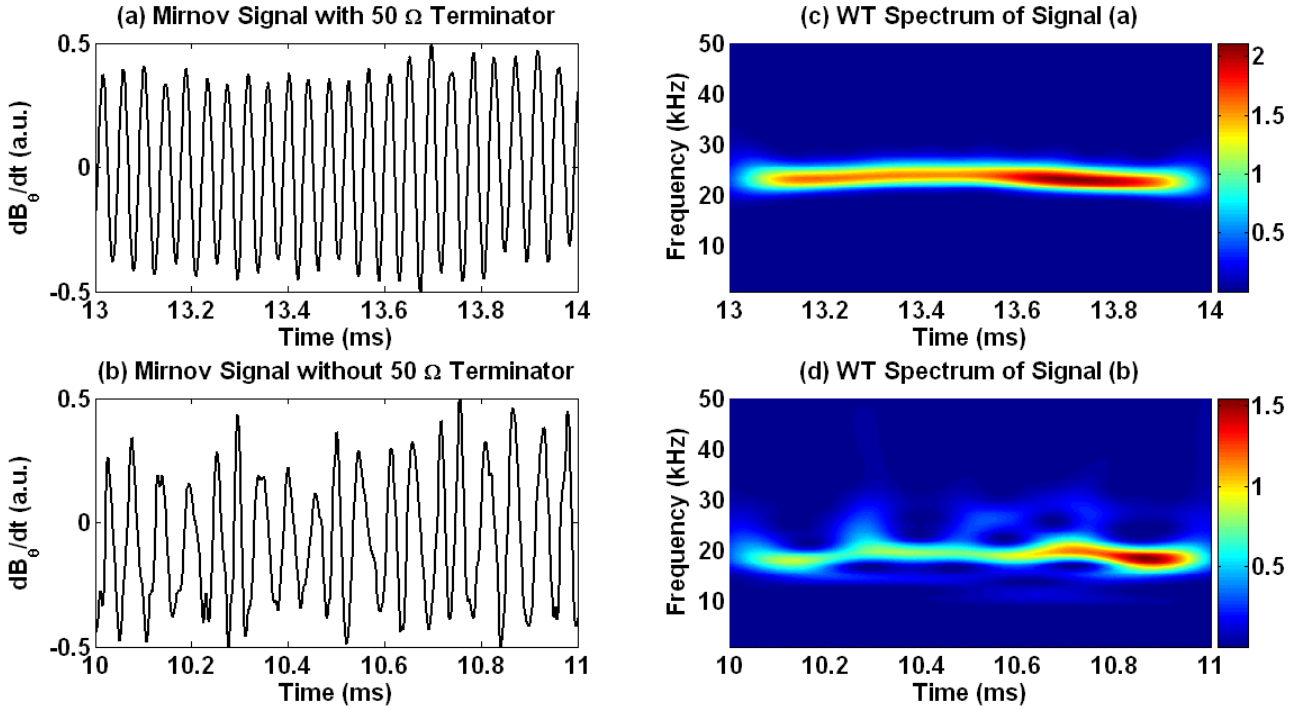

Figure 5.5: WT analysis of two Mirnov signals with and without a 50 Ω terminator installed parallel to the digitizer. The signals were collected by the same Mirnov coil (i.e. coil 1-12) during the normal discharges #200790 and #200796.

A side attempt was carried out to measure the impedance for one of the Mirnov arrays. The impedance can be calculated by knowing the real-valued resistance R and the imaginary-valued reactance X of the Mirnov coil. Since the Mirnov coil can be simulated by an LCR circuit, each of the circuit components, which are resistance R, inductance L and capacitance C, had to be measured independently. Also, the corresponding net reactance X, which is defined by the difference between inductive X_L and capacitive X_C reactance, had to be evaluated at certain AC frequency. Therefore, the coils of Mirnov array 1 were gauged using a BK Precision LCR meter (Model 879) equipped with a variable frequency bandwidth 100 Hz-10 kHz $\pm$ 0.1% [88], allowing the measurement of R, L and C at any desirable test frequency. The inductive and capacitive reactance can be

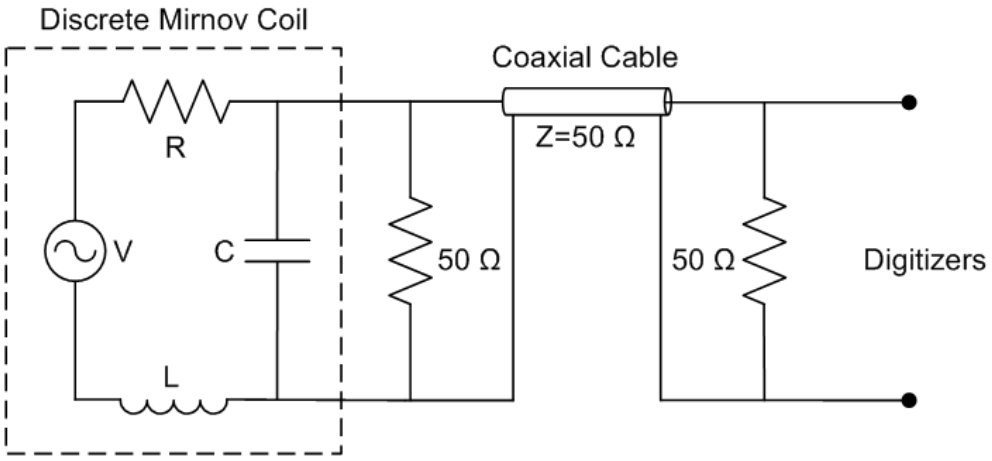

Figure 5.6: A diagram of the impedance matching circuit. The inductance, the resistance, and the stray capacitance of the coil are drawn within the broken-line box.

calculated from their relationship with the frequency f as [89]:

$$X_L = 2\pi f L \qquad \text{Inductive Reactance} \tag{5.6}$$

$$X_C = \frac{1}{2\pi f C} \qquad \text{Capacitive Reactance} \tag{5.7}$$

The vector relationship shown in Figure 5.7 implies that the magnitude and phase of impedance Z can be directly computed from the resistance R and the net reactance X using the following relations:

$$|Z| = \sqrt{R^2 + (X_L - X_C)^2} \tag{5.8}$$

$$\theta = \tan^{-1}\left(\frac{X_L - X_C}{R}\right) \tag{5.9}$$

where the factor $X_L - X_C$ was used for X. The results of impedance calculations for Mirnov array 1 are listed in Table 5.1. The negative value of reactance X indicates that the Mirnov coils have capacitive reactance as a result of $X_C > X_L$. The table also shows that the resistance and the absolute value of the impedance of the coils are smaller than 50 Ω. Therefore, connecting resistors with value larger than 50 Ω in parallel with the coils does not affect the total impedance too much. In the transmission line, impedance matching must be made at least on one end of the long cable.

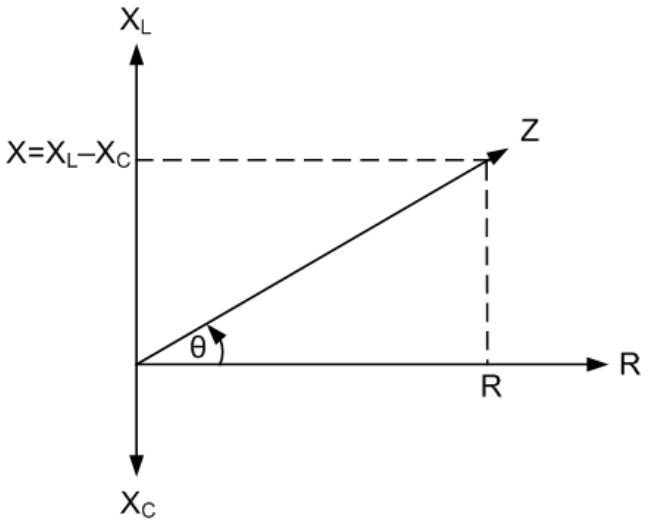

Figure 5.7: A vector diagram illustrating the relationship between the resistance R, the reactance X, and the impedance Z.

Coil No.	R (Ω)	L (μH)	C (nF)	X_L (Ω)	X_C (Ω)	X (Ω)	$\lvert Z \rvert$ (Ω)	θ (rad)
1-1	29.02	186.3	1217.5	11.70	13.07	-1.37	29.05	6.23
1-2	27.36	177.3	1272.7	11.14	12.50	-1.36	27.39	6.23
1-3	30.66	191.2	1204.5	12.01	13.21	-1.20	30.68	6.24
1-4	27.74	176.4	1291.4	11.08	12.32	-1.24	27.76	6.23
1-5	27.73	173.9	1304.5	10.92	12.20	-1.28	27.75	6.23
1-6	27.98	176.4	1298.9	11.08	12.25	-1.17	28.00	6.24
1-7	25.48	162.1	1407.2	10.18	11.31	-1.13	25.50	6.23
1-8	25.18	160.6	1418.7	10.09	11.21	-1.12	25.20	6.23
1-9	27.28	169.8	1360.3	10.66	11.69	-1.03	27.29	6.24
1-10	26.68	164.2	1412.9	10.31	11.26	-0.95	26.69	6.24
1-11	28.93	172.0	1369.5	10.80	11.62	-0.82	28.94	6.25
1-12	27.81	168.6	1386.3	10.59	11.48	-0.89	27.82	6.25

Table 5.1: Impedance calculations for the Mirnov array 1 at test frequency 10 ± 0.01 kHz.

5.3.3 System Calibration

For a multichannel diagnostic system, it is very important to calibrate the system using a fixed source to eliminate any inconsistence associated with the fabrication of each individual channel. The fabricated coils, along with their transmission line and other components, were calibrated against each other using an existing Helmholtz coil power supply. The current through the Helmholtz coil is measured by a resistor with a calibrated output $I/V = 115.8 \pm 0.9$ (A/V). At the center of the Helmholtz coil, the magnetic field is nearly uniform with the following calibration: $B(\text{Gauss}) = (0.59 \pm 0.01)I(\text{A})$. In this calibration, the Helmholtz coil system was used only as a power supply to provide a time-varying current. A schematic of the calibration circuit is illustrated in Figure 5.8.

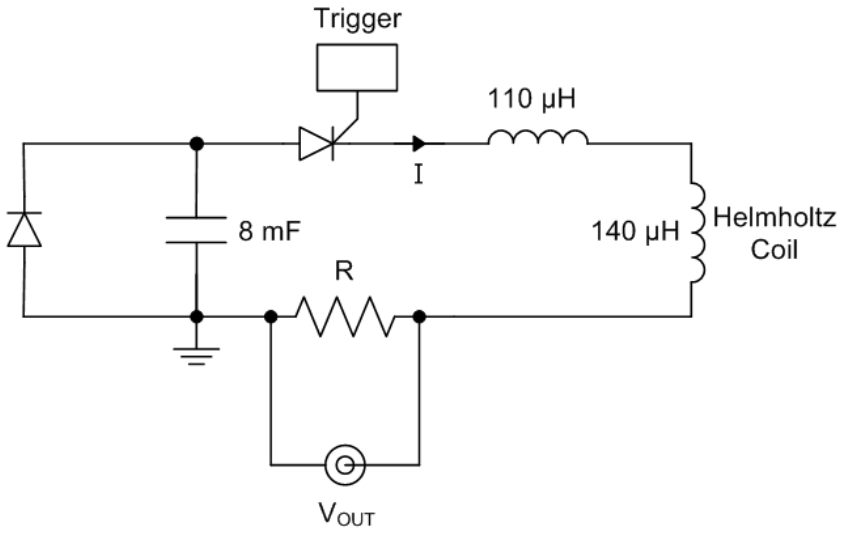

Figure 5.8: The calibration circuit of the discrete Mirnov coils.

During the calibration, the Mirnov arrays were mounted around four Styrofoam disks each with a thickness of 5 cm and radius of 17 cm, simulating the radius of the vacuum chamber wall of STOR-M. A 4 m aluminium rod with a radius of 0.5 cm passes through the center of the disks. The rod was placed horizontally and the disks vertically. A current through the rod introduced a poloidal magnetic field on all Mirnov coils with the same amplitude. The Helmholtz power supply provided the needed current passing through the long aluminium rod. Those signals were collected simultaneously using DAS. The waveforms of the source current and the signal from Mirnov coil

1-1 (the first number denotes the array index and the second one the coil index in the array) are displayed in Figure 5.9. Similar calibration discharges were repeated to average out random errors and the noises.

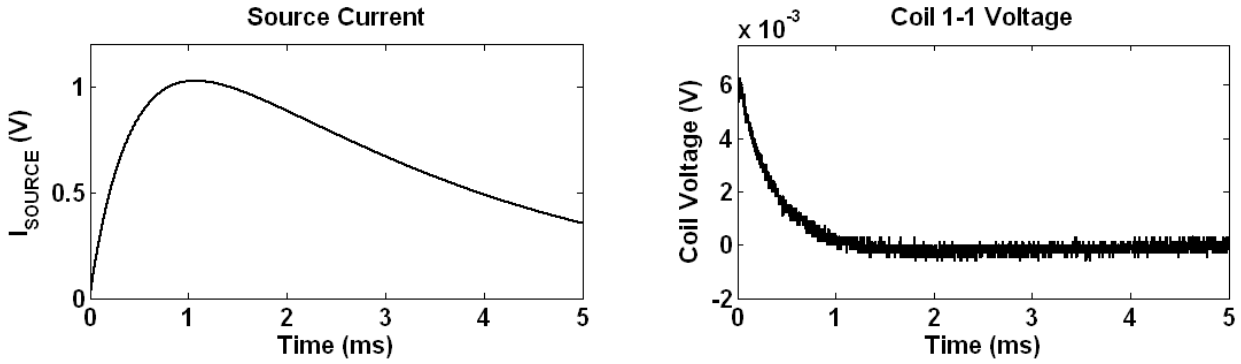

Figure 5.9: Unprocessed waveforms of the source current and the signal from Mirnov coil 1-1.

In order to count for systematic errors of the calibration system, e.g., caused by the return current path and by the inaccuracy of the fabrication of the styrofoam disks and Mirnov coils, the Mirnov arrays were rotated by 180°. The purpose of rotating the arrays at different orientations is to average out the magnetic field induced in the coils. It has been noticed that the lower coils were detecting a magnetic field stronger than the upper ones. This up-down asymmetry of the magnetic field may be caused by the magnetic noises near the calibration setup. Again, DAS was used to store the power supply current and the output signals from the Mirnov coils. The peak voltages of Mirnov coils at 0° and 180° orientations are shown in Figure 5.10(a).

After collecting the calibration data, the average of peak voltages was calculated by averaging the peak voltage of each coil collected at both orientations. The average of peak voltages is plotted in Figure 5.10(b). The calibration factors were calculated from the average of peak voltages with respect to the coil with the highest peak voltage (i.e. coil 2-3). The source current was also taken into account by calculating calibration factors for several discharges with source currents having a minimum error margin. The calibration factors of Mirnov coils are listed in Table 5.2.

There is a variation in the calibration factors up to 40% particularly from the arrays 1 and 3 because the magnet wire that is used for winding these arrays has a thicker insolation compared to the one

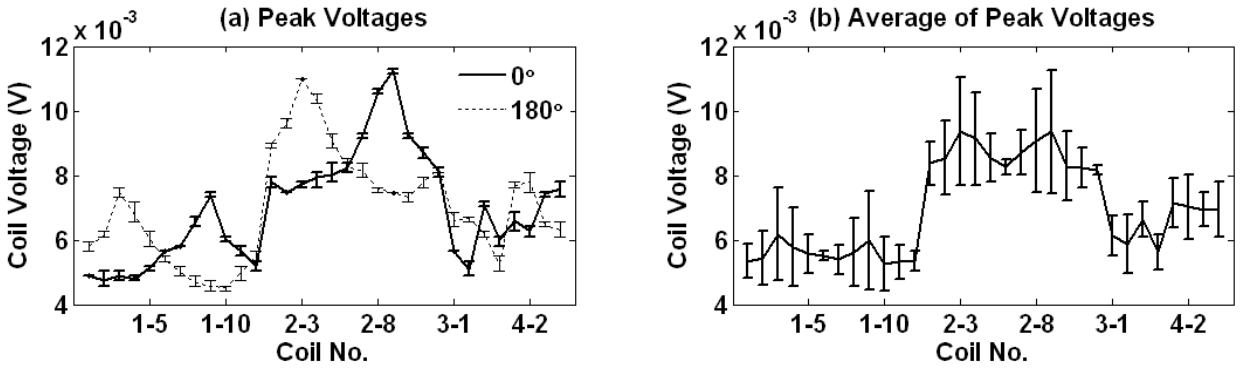

Figure 5.10: Experimental readings of (a) peak voltages of Mirnov coils at the positions 0° and 180° (b) the averaged peak voltages of Mirnov coils.

used for arrays 2 and 4. Also, since the exact installation setup of Mirnov arrays on STOR-M was used in this calibration, the coaxial cables connected to array 3 are much longer which means more attenuation in the transmitted signals. However, this is not a obstacle since those variations can be counted for during data processing. In addition, some numerical techniques (e.g. SVD) require normalization of the signals within a certain range of amplitudes (to be discussed in the next subsection).

5.3.4 Initial Test

The preliminary analysis of the Mirnov signals during an experimental test revealed some issues related to the signal quality. The first problem is related to the inconsistency between the amplitude of the inward and outward signals which may be a result due to the Shafranov shift of magnetic surfaces [90], the ballooning effects on the outboard side, or the shape of the plasma column during tokamak discharge. This issue can be easily solved by normalizing all the signals within an arbitrary numerical range (e.g. -0.5-0.5) for some signal processing techniques.

The other issue originates from the toroidal locations of the Mirnov arrays. As mentioned earlier in Subsection 5.3.1, arrays 1 and 2 are installed on bellows with a thickness of 0.5 mm, while the arrays 3 and 4 are placed on the 4 mm stainless steel-304L wall. In addition to the expected signal attenuation through the wall, there is also a significant phase delay between the signals obtained through the bellows and the wall. A simplified study was conducted to correct this phase delay by

Array-Coil	**Calibration Factor** (A/V)	**Array-Coil**	**Calibration Factor** (A/V)
1-1	1.75 ± 0.17	2-5	1.09 ± 0.09
1-2	1.72 ± 0.26	2-6	1.13 ± 0.03
1-3	1.51 ± 0.35	2-7	1.07 ± 0.08
1-4	1.62 ± 0.34	2-8	1.03 ± 0.18
1-5	1.68 ± 0.18	2-9	1.00 ± 0.20
1-6	1.69 ± 0.04	2-10	1.13 ± 0.14
1-7	1.73 ± 0.14	2-11	1.13 ± 0.08
1-8	1.66 ± 0.31	2-12	1.14 ± 0.02
1-9	1.56 ± 0.40	3-1	1.52 ± 0.15
1-10	1.77 ± 0.28	3-2	1.59 ± 0.24
1-11	1.76 ± 0.17	3-3	1.41 ± 0.11
1-12	1.75 ± 0.10	3-4	1.66 ± 0.15
2-1	1.11 ± 0.09	4-1	1.31 ± 0.14
2-2	1.09 ± 0.14	4-2	1.33 ± 0.18
2-3	1.00 ± 0.18	4-3	1.34 ± 0.10
2-4	1.02 ± 0.16	4-4	1.34 ± 0.16

Table 5.2: Calibration factors of the discrete Mirnov coils.

compensating the affected signals with the proper phase angle.

The phase correction is applied only to the signals of Mirnov coils propagated through the chamber wall. Theoretically speaking, by adding the difference in calculated phase delay between the bellows and the wall to the phase-delayed signals through the wall or bellows, the phase-corrected signals will have the proper phase angles when the coils are used to form a toroidal array for analysis of toroidal mode numbers. The phase correction can be calculated based on the skin depth δ defined for a good conductor by [91]:

$$\delta = \frac{1}{\sqrt{\pi f \mu \sigma}} \tag{5.10}$$

where μ is the absolute magnetic permeability and σ is the conductivity of the conductor. Figure 5.11 shows the time and phase delay of a signal traveling through the relative thickness between

the bellows and the chamber wall. The time and phase delay are related to the skin depth by:

$$t = \frac{\Delta d}{2\pi f \delta} \qquad \text{Time Delay} \tag{5.11}$$

$$\phi = \frac{\Delta d}{\delta} \qquad \text{Phase Delay} \tag{5.12}$$

where Δd is the difference in thickness between the bellows and the wall, which is 3.5 mm. The delay in time and phase was calculated for a stainless steel-304L wall with permeability $\mu \simeq \mu_0 = 4\pi \times 10^{-7}$ H/m and conductivity $\sigma = 1.45 \times 10^6\ \Omega^{-1} \cdot \text{m}^{-1}$.

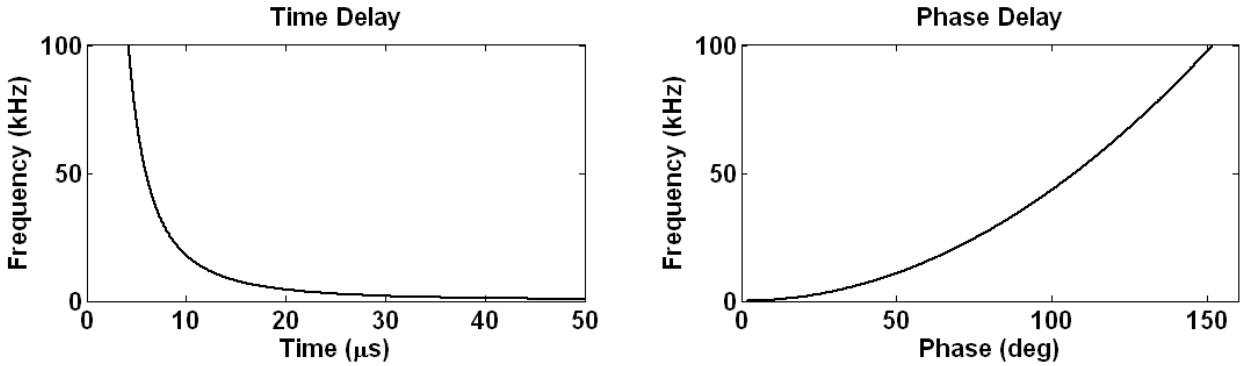

Figure 5.11: Time and phase delay in the relative thickness between the bellows and the chamber wall.

The procedures of correcting any signal phase are outlined below:

1. Fourier transforming the target signal $x(t)$ and extracting the dominant frequency f.

2. Calculating the skin depth δ at the frequency f from Equation 5.10.

3. Finding the amount of the phase delay ϕ (in rad) for the thickness $\Delta d = d_{\text{wall}} - d_{\text{bellows}}$ using Equation 5.12.

4. Defining the required number of sampling points for the phase correction, so that:

$$\hat{\phi} = \frac{M}{f}\frac{\phi}{2\pi} \tag{5.13}$$

where $\hat{\phi}$ is a phase corrector and M is the total number of samples in $x(t)$.

5. Rounding the phase corrector $\hat{\phi}$ towards the closest integer number since the sampling system is discrete.

6. Constructing a phase operator denoted by Γ:

$$\Gamma = e^{i\left(\frac{2\pi\hat{\phi}}{M}\right)z}, \quad z = 0, 1, \cdots, M-1 \tag{5.14}$$

   which generates an array with length of M.

7. Imposing the new phase to the signal by multiplying the FT of $x(t)$ by Γ.

8. Recovering the phase-corrected signal $x(t)$ by inverting the new FT back to the time domain.

Figure 5.12 is contour plots of four Mirnov signals before and after applying the phase correction. The Mirnov signals were collected during the normal discharge #203890 using the outboard toroidal array. The contour plot in Figure 5.12(a) displays two Mirnov signals with a phase lag caused by the chamber wall. The affected signals were collected by coils 3-1 and 4-1 which are located on the contour plot respectively at toroidal angles 270° and 0°. The phase correction was carried out for the phase-delayed signals with the procedures described earlier. The amount of phase compensated for the signals is about 1.3 rad ($\sim 75°$) which was calculated at the dominant frequency 24 kHz. Figure 5.12(b) is a contour representation of the Mirnov signals after applying the phase correction, all with the proper phase angle.

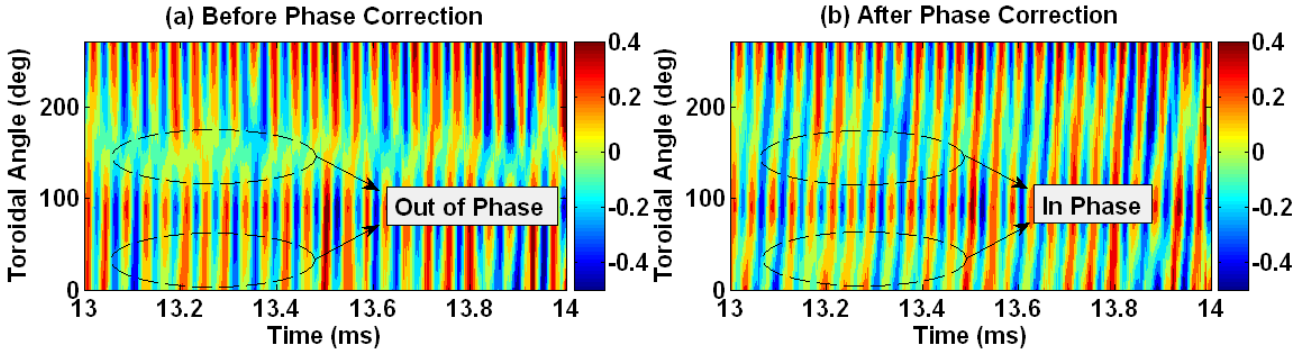

Figure 5.12: Phase correction for the signals transmitted through the chamber wall. The Mirnov signals were collected by the toroidal array during the normal discharge #203890.

5.4 Soft X-Ray System

A new SXR system consisting of two miniature pinhole camera arrays has been assembled and installed on STOR-M [92]. The SXR cameras are designed to be inserted through a port with an inner diameter of 4.8 cm. Each SXR array consists of a 20-channel photodiode linear array (IRD AXUV-20EL) and a rectangular pinhole with a size of 1×4 mm^2. The array of photodiodes is located 1 cm away from the pinhole. The size and location of the pinhole is optimized to avoid any overlapping with nearby channels and to provide a good spatial resolution. Figure 5.13 shows the lines of sight of SXR arrays over the plasma cross-section through horizontal and vertical ports separated by 90°.

The diode current is preamplified using a set of IRD AMP16 preamplifiers with fixed gains of 10^5 V/A. The diodes are connected in a biased common anode configuration. The preamplifiers are connected to the diodes using coaxial cables with an approximated length of 1 m. The preamplified SXR signals are transmitted to the home-made amplifiers with variable gains. DAS is used for acquiring the signals. A photograph of the SXR system and the box for preamplifiers is presented in Figure 5.14.

The SXR system has been preliminarily tested during STOR-M normal operation. Precursor oscillations superimposed on sawtooth crashes have been identified, which are also detected by discrete Mirnov coils. However, an in-depth analysis for SXR signals can not be performed within the time frame of this research. A short correlative study between Mirnov and SXR signals was carried out, the results are discussed in Section 6.6.

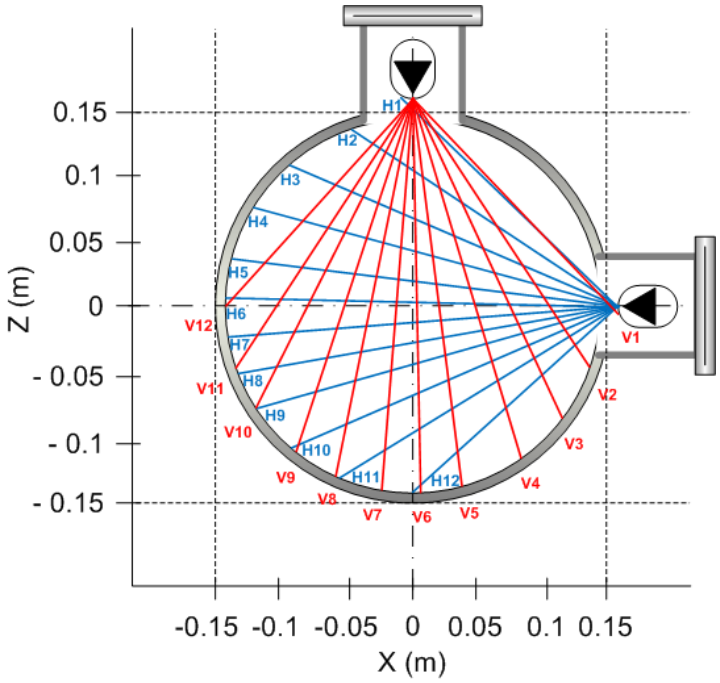

Figure 5.13: Lines of sight of the SXR detector arrays across the STOR-M tokamak cross-section.

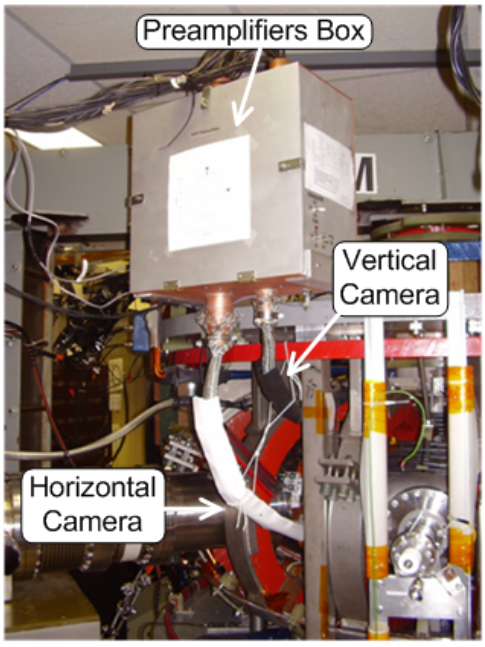

Figure 5.14: A photograph of the SXR system and the preamplifier shielding box mounted on the STOR-M tokamak.

Chapter 6

Data Analysis and Results

6.1 Introduction

The MHD fluctuation signals recorded by the discrete Mirnov coils were analyzed carefully using the signal processing techniques discussed in Chapter 4. Before proceeding to the experimental results, the numerical techniques were tested with an artificial data to determine their ability to deal with real Mirnov signals. Experimentally, the results of MHD analysis during STOR-M ohmic discharge and CT injection are discussed in this chapter. Amplitude modulations of the Mirnov oscillations and the correlation between the Mirnov and SXR signals are presented as well.

6.2 MHD Modes Simulation

Before applying the numerical analysis on experimental data, simulated MHD signals for various modes were created as input data to elucidate the meaning of the output. In addition, a more complicated scenario involving several mixed MHD modes was also considered to simulate mode coupling between magnetic islands. A customized version of the numerical test detailed in the paper [83] was used for this simulation. A set of artificial samples was generated using the

following wave equation:

$$X_{ij} = \frac{1}{\sqrt{M}} \sum_{l} a_l \cos\left[\frac{2\pi m_l}{N}(j-1) + \phi_l - 2\pi f_l t_s (i-1)\right] + a_{\text{noise}}\sigma_{ij}, \tag{6.1}$$

where the indices i and j are respectively designated for the time series and channel number. The given wave equation produces a cosine wave with the superposition of l number of modes m_l having amplitudes a_l, phase angles ϕ_l and rotating frequencies f_l. A white noise σ_{ij} with amplitude of a_{noise} was integrated into the wave to emulate the real Mirnov signals. The wave signal was calculated at N different poloidal positions and sampled every t_s in time. Two data matrices were assembled using Equation 6.1. The first matrix contained a chain of 3 independent modes with distinct frequencies to simulate an uncoupled mode scenario. The other matrix simulated 3 modes with two modes locked on the same frequency for a mode coupling scenario. The two scenarios are discussed in the following two subsections.

6.2.1 Decoupled Mode Scenario

The complex Mirnov signals can be simplified by the superposition of multiple MHD modes. In this sense, a set of Mirnov oscillations presented by an $M \times N$ data matrix was generated using the Equation 6.1 and the wave parameters listed in Table 6.1. In this scenario, the data matrix consists of $N = 8$ channels with $M = 1001$ samples per channel sampled every $t_s = 1$ μs at total duration $t = 1$ ms $(= (i-1) \times t_s, i = 1, 2, \cdots, M)$. The signals oscillated at three distinct frequencies slowly drifting in time. The embedded white noise was generated randomly between -1 and 1 and multiplied by the amplitude $a_{\text{noise}} = 0.001$. The frequencies of the bulk wave were extracted using WT analysis. The phase correlation, spatial structure and time evolution of the superimposed MHD modes were decomposed by performing FCC, FCD and SVD analyses on the data matrix.

WT analysis was carried out for the first channel of the data matrix corresponding to the time series of a particular Mirnov coil. The WT power spectrum shown in Figure 6.1 displays the frequencies

Mode Number (m_l)	**Amplitude** (a_l)	**Frequency** (f_l)	**Phase** (ϕ_l)
1	1.00	$20.0 + 6.0t$	0.00
2	0.60	$50.0 - 1.2t$	0.50
3	0.30	$90.0 - 7.6t$	0.33

Table 6.1: List of parameters used to simulate the decoupled mode scenario.

of the three MHD modes contained in the data set. The first mode $m = 1$ propagates in space with starting frequency $f_1 = 20$ kHz growing slowly in time. WT analysis also extracted the corresponding frequency of the $m = 2$ mode which is labeled by f_2 and bandlimited between 50 and 48.8 kHz. The low fluctuation energy of $m = 2$ results from the fact that the mode was assumed to have a slightly lower amplitude ($a_2 = 0.6$) compared to the $m = 1$ amplitude ($a_1 = 1$). The energy content of the third mode ($m = 3$) is barely visible on the WT spectrum as it oscillates with the lowest amplitude ($a_3 = 0.3$). The initial rotating frequency of $m = 3$ was identified by WT as $f_3 = 90$ kHz with a decay rate of 7.6 kHz/ms.

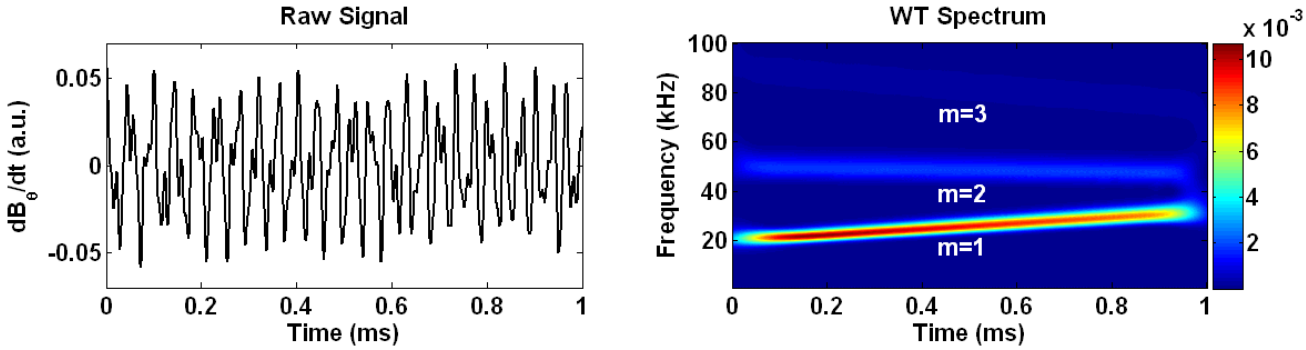

Figure 6.1: WT analysis for the first channel of the artificial signals.

Using the first channel of the data set as a reference, the FCC analysis was applied on the data matrix in an attempt to find any correlation between the data channels. The FCC analysis was performed on a time window containing the first $\frac{M}{2}$ sample points, then the window was swept 1 sample per FCC computation until the entire data were analyzed. Afterward, FCC power, coherence and phase spectra were averaged over the total number of computations $\frac{M}{2}$. Figure 6.2(a) indicates that the auto-power spectrum of the first channel is well coherent at three frequencies $f_1 = 26$ kHz, $f_2 =$

48 kHz and $f_3 = 82$ kHz which are located somewhere within the frequency bandwidths presumed initially. The FCC cross-power spectrum between signals 1 and 2, shown in Figure 6.2(b), also peaks at the same frequencies indicating the presence of three modes with strong correlation. The correlated MHD modes have maximum coherence values ($\gamma \sim 1$) on the coherence spectrum. The coherent frequencies are clearly visible in Figure 6.2(c). FCC was able to distinguish the superimposed MHD modes by comparing the baseline phase of MHD modes and the phase at the coherent frequencies computed from Equation 4.33. By calculating the FCC phase at the coherent frequencies, the mode numbers can be obtained by plotting the phase angle versus the channel location. Figure 6.2(d) demonstrates the phase comparison between the baseline slopes of modes (dotted lines) and the calculated phase slopes at the coherent frequencies (solid lines). In order to obtain the phase slope for modes higher than 1, the calculated phase angles have to be wrapped to $360^\circ \times m$, where m is the mode number. For instance, since the phase angles of $m = 3$ are folded twice at 360°, the phase slope of $m = 3$ is plotted after extending the phase angles to $360^\circ \times 3 = 1080^\circ$. Hence, the correlated MHD modes were identified by FCC as $m = 1$ at $f_1 = 26$ kHz, $m = 2$ at $f_2 = 48$ kHz and $m = 3$ at $f_3 = 82$ kHz.

The FCD analysis was also performed on the numerical data set. Although no spatial information can be directly derived from FCD calculations, it is very useful to preliminarily utilize FCD analysis for mapping a swift pattern of the MHD mode propagation in space. Another merit of using FCD for mode analysis is that the mode number is assigned before carrying out the FCD calculations. For instance, if the FCD calculations are meant for a certain mode number m, the Fourier coefficients can be computed exclusively for that mode, thus the number of computations can be greatly reduced as there is no need to carry out unnecessary calculations for other modes. Using the formulae set 4.40, the Fourier sine and cosine coefficients of $m = 1$, $m = 2$ and $m = 3$ were computed by FCD. The Fourier coefficients of each mode were calculated firstly by breaking down the data matrix channels into Fourier sine and cosine series. The substitution for the desired mode number and the associated angular location of channels (in rad) was made before taking the sum of the Fourier series over the total number of channels. The FCD computations can be repeated for any other

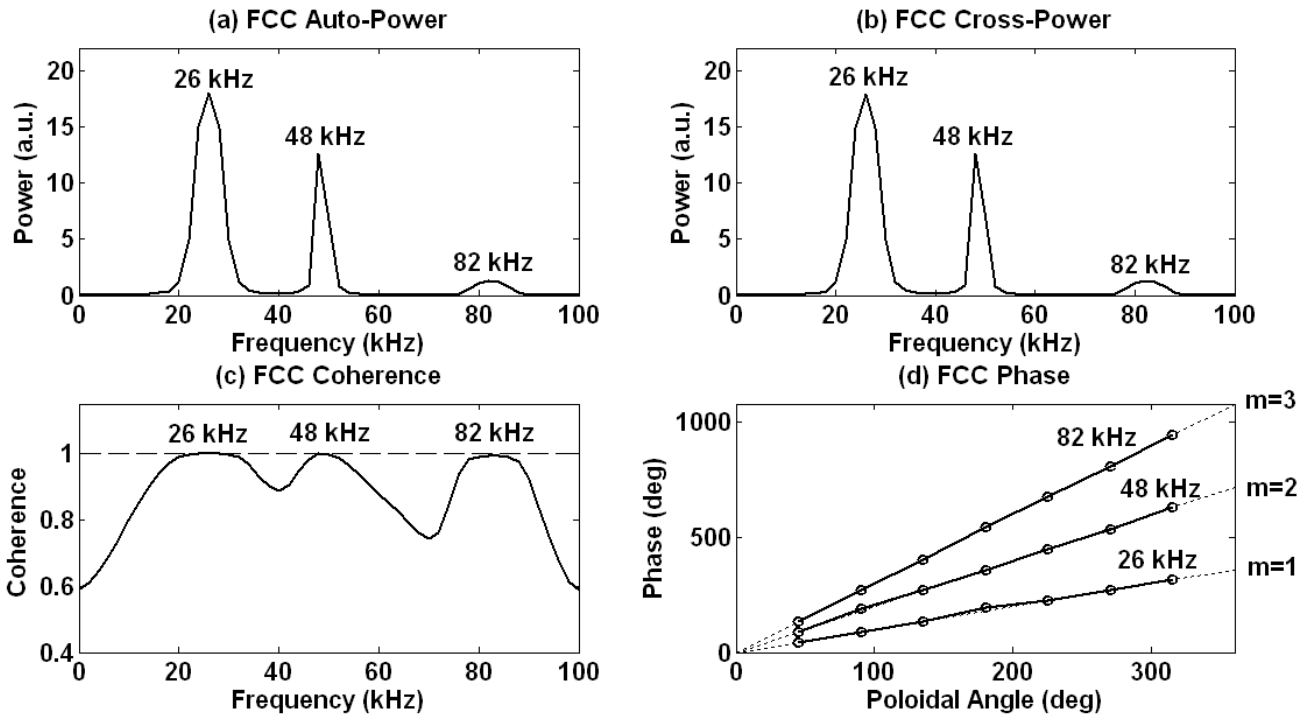

Figure 6.2: The results of FCC analysis for the numerical data.

MHD mode if desired. The sine and cosine coefficients of $m = 1$, $m = 2$ and $m = 3$ are plotted in Figure 6.3(a), (b) and (c). Judging from the FCD magnitudes in Figure 6.3(d), the dominant $m = 1$ mode is readily determined since it has the highest energy content among all three modes.

Finally, the data matrix was decomposed into the time and space-covariance bases using the SVD algorithm. The SV spectrum shown in Figure 6.4 is formed by a set of SV pairs representing the MHD modes subsumed in the raw data. As documented, the SVs are automatically sorted in descending order relative to the mode amplitude. Each pair is composed of one sine and one cosine Fourier component of the same mode. The spatial structure of the MHD mode can be well identified by plotting a polar representation of the corresponding PAs versus the angular location of channels. For better representation, a shape-preserving spline interpolation is used for smooth polar plots. As it is seen from the polar plots in Figure 6.5, SVD analysis was able to extract the modes $m = 1$, $m = 2$ and $m = 3$ with apparent spatial features. Although the last pair may be formally characterized as an $m = 4$ mode based on the interpretation of the polar plot, the mode is actually associated with the white noise that was artificially added to the data set as indicated by a noisy

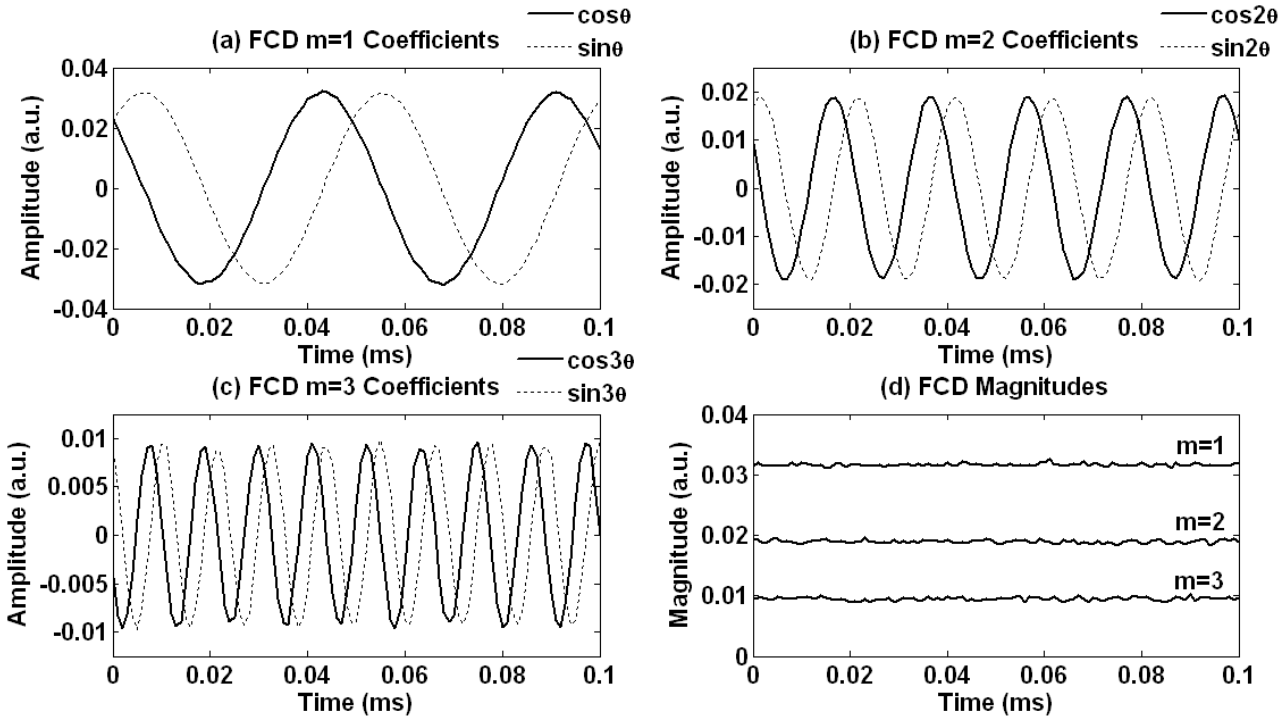

Figure 6.3: The results of FCD analysis for the numerical data.

waveform of PCs. Examination of the waveform of PCs is helpful to identify whether a real mode is extracted or not, and to understand the variation in frequency behavior of magnetic islands in space. The temporal evolution of each mode can be revealed by plotting the corresponding columns of the matrix of PCs along the time axis. The temporal evolution of MHD modes are shown in Figure 6.5 in the panels on the right. Each PC pair is plotted on the same diagram for comparison purposes. PCs associated with the same pair oscillate sinusoidally at the same frequency, but maintain a fixed phase difference of 90°. The PCs associated with $m = 4$ are simply noise artificially added. If the mode amplitude is smaller than the noise, it is difficult to separate it from noise as expected.

The SVD results obtained in this simulation agree with the results reported in the reference numerical test despite the few modifications made in wave parameters. Additionally, to confirm the exact numbers and frequencies of MHD modes, FT can be performed on PAs to extract the mode numbers as well on PCs for the corresponding frequencies. Implementing the spatial and temporal FTs with the SVD technique is a very useful approach to handle some of the complicated Mirnov signals involving MHD mode coupling.

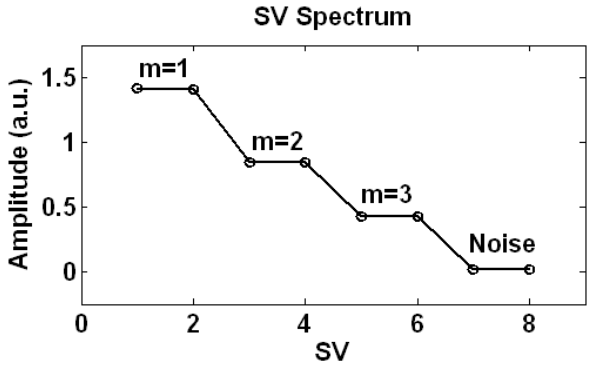

Figure 6.4: SV spectrum of the numerical data.

6.2.2 Mode Coupling Scenario

The typical nature of mode coupling is defined by two or more MHD modes oscillating at the same frequency [93]. This definition coincides with the fact that tokamak toroidicity deforms the poloidal geometry of the magnetic islands. The toroidicity and shape of the magnetic surfaces may avert the MHD modes from possessing pure Fourier coefficients which leads to coupling between Fourier harmonics on different rational surfaces [94]. The latter case can be numerically examined by generating a new set of artificial data that contains two modes with different numbers rotating at the same frequency. The wave parameters listed in Table 6.2 were substituted in Equation 6.1 to create a mode coupling scenario.

Mode Number (m_l)	**Amplitude** (a_l)	**Frequency** (f_l)	**Phase** (ϕ_l)
1	1.00	$20.0 + 6.0t$	0.00
2	1.00	$20.0 + 6.0t$	0.50
3	0.30	$90.0 - 7.6t$	0.33

Number of Channels: $N = 8$, Samples per Channel: $M = 1001$, Sampling Time: $t_s = 10^{-3}$ ms, Noise Amplitude: $a_{\text{noise}} = 0.001$, Signal Duration: $t = (i-1) \times t_s, i = 1, 2, \cdots, M$.

Table 6.2: List of parameters used to simulate the mode coupling scenario.

In this scenario, the $m = 1$ and $m = 2$ modes were set to have the same frequencies, initial at $f =$ 20 kHz and drifting slowly in time. The data set was analyzed by FCC which failed to decouple the modes. The slope of the FCC phase given in Figure 6.6(a) is located exactly between $m = 1$

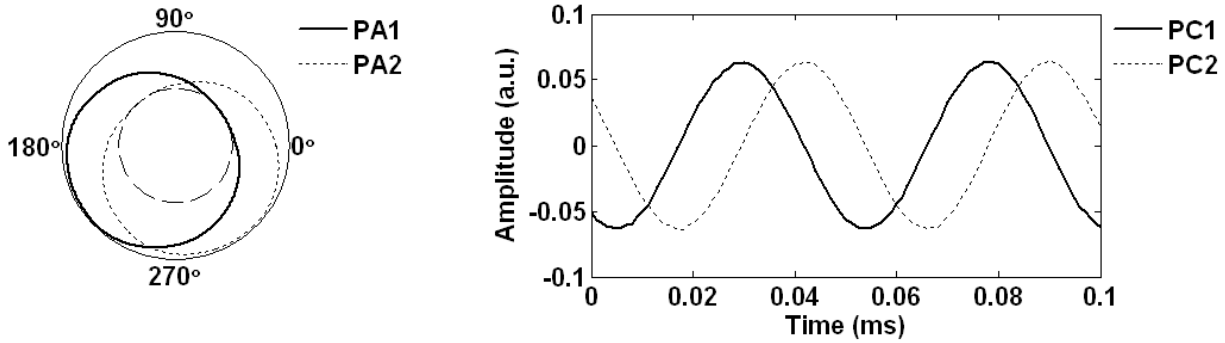

(a) Spatial structure and temporal evolution of the $m = 1$ mode.

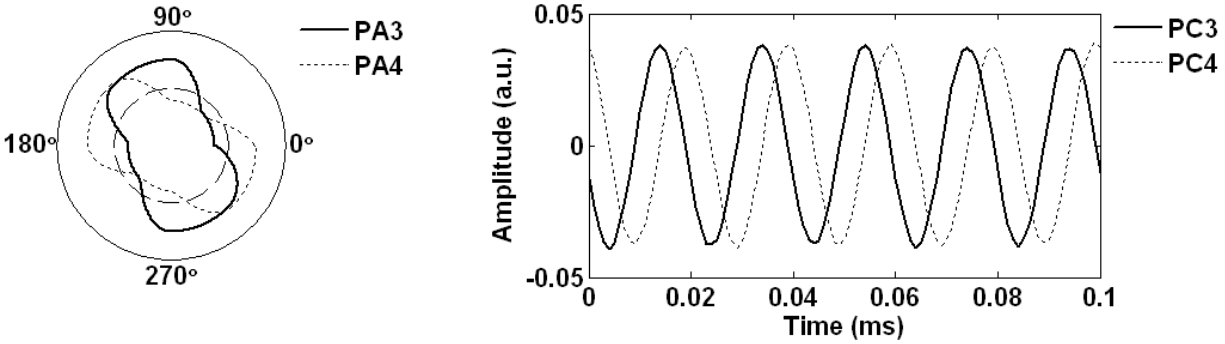

(b) Spatial structure and temporal evolution of the $m = 2$ mode.

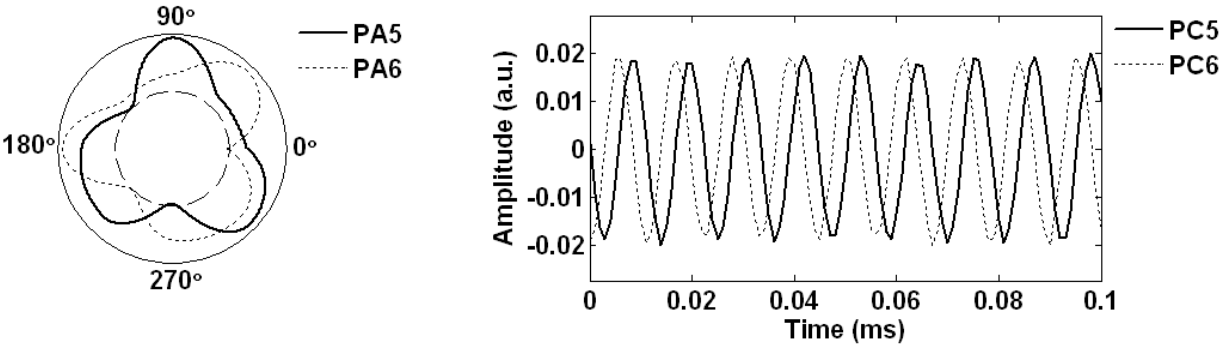

(c) Spatial structure and temporal evolution of the $m = 3$ mode.

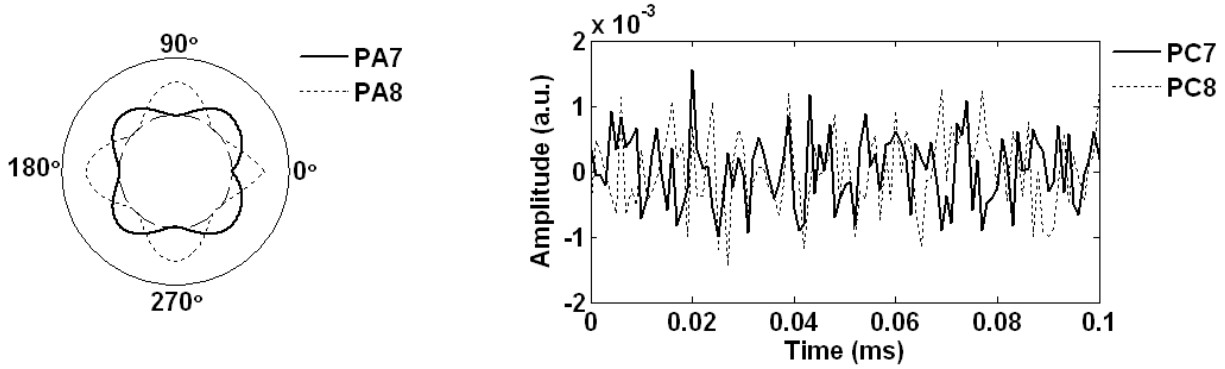

(d) Spatial structure and temporal evolution of white noise.

Figure 6.5: The results of SVD analysis for the numerical data.

and $m = 2$ baseline slopes. The FCC slope is averaged out to 1.5 since the coupled modes oscillate at the same frequency and amplitude. The apparent slope may vary with the relative amplitudes of the coupled modes, leading to a faulty interpretation in mode numbers. Therefore, it is advisable to avoid using FCC for Mirnov signals when strong mode coupling exists. In contrast, the mode coupling can be treated easily by FCD as it has the ability to perform computations for each mode separately. The Fourier coefficients of the coupled modes are found to be at equal magnitudes as it is seen in Figure 6.6(b). The same magnitudes for the $m = 1$ and $m = 2$ modes are obtained, but are not distinguishable in the diagram. This is an expected result due to the equal amplitude assumed for the $m = 1$ and $m = 2$ modes.

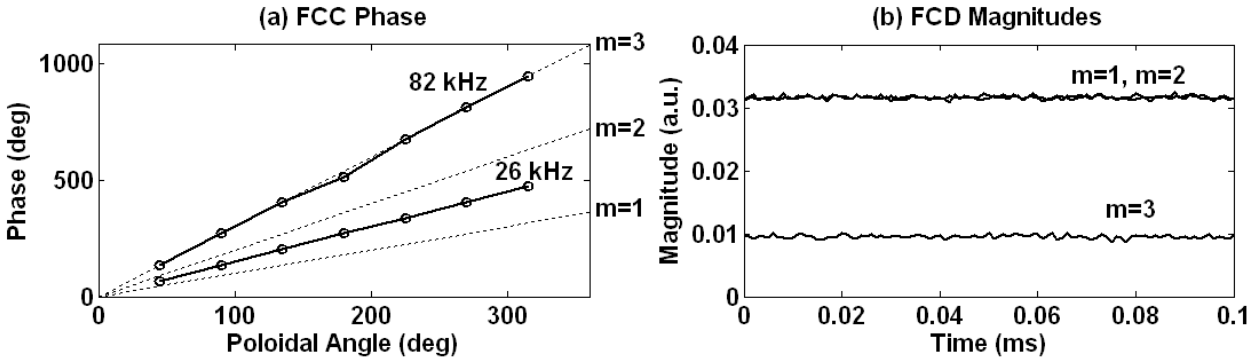

Figure 6.6: FCC and FCD analyses for the coupled $m = 1$ and $m = 2$ modes and the decoupled $m = 3$ mode.

SVD is a very powerful technique in terms of dealing with mode coupling since it was introduced in the first place for this purpose. SVD can identify the mode coupling between two or more MHD modes oscillating at the same frequency. The SV spectrum shown in Figure 6.7 contains only two significant SV pairs. The first pair represents the Fourier components of the coupled modes $m = 1$ and $m = 2$ while the second pair belongs to the $m = 3$ mode. The coupled modes were identified by SVD as a sole, non-sinusoidal mode (not shown) with distorted spatial structure. The polar plot of PAs shown in Figure 6.8 does not appear to correspond to a mode number. Therefore, the spatial FT was performed for PAs for better interpretation of the mode structure. FT was able to decouple PAs and extract the coupled modes. The spatial Fourier spectrum shown in the diagram on the right panel in Figure 6.8 reveals two peaks at $m = 1$ and $m = 2$ along the mode number axis with the

same amplitude as expected.

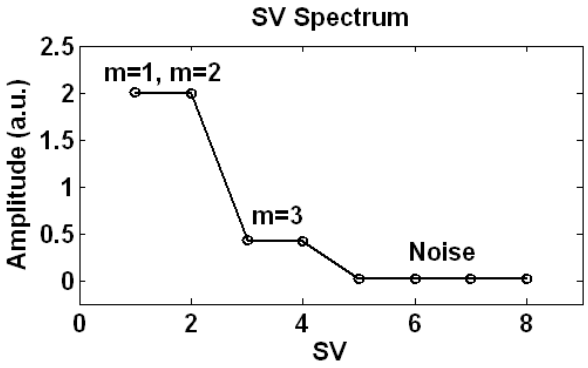

Figure 6.7: SV spectrum of the numerical data for the coupled modes.

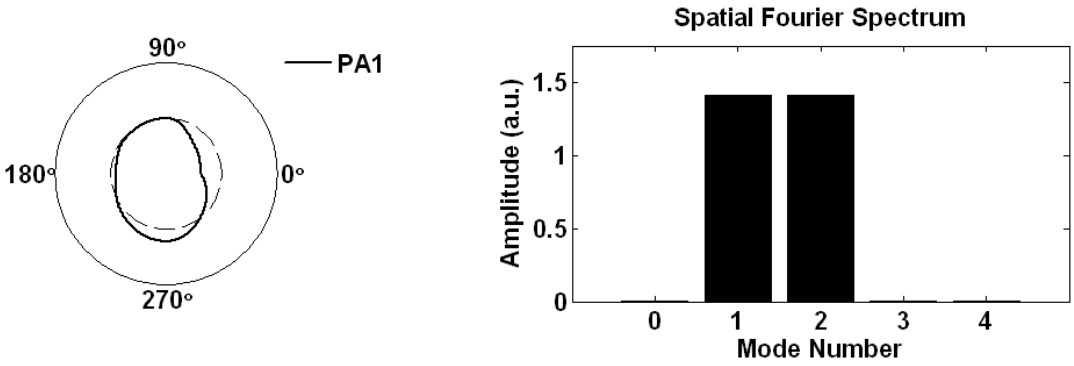

Figure 6.8: Spatial FT for one of the coupled PAs.

The mode coupling scenario simulated in this test was induced between two MHD modes locked on the same frequency with the same amplitude. However, since mode coupling is frequently present in real experimental signals in many tokamaks including STOR-M, mode coupling may occur on the frequency while the amplitudes of coupled modes vary autonomously with time. Therefore, the spatial Fourier spectrum has to be interpreted cautiously as the spectrum varies itself with the varying ratio between the amplitudes of the coupled modes. It is important to consider finite time windows during the analysis in order to intercept the rapidly changing magnetic islands in tokamaks.

6.3 Normal Ohmic Discharge

FCC, FCD and SVD analyses on experimental data can be carried out in a manner similar to that for the artificial data. However, some procedures have to be taken before proceeding any further. Firstly, removing, or at least minimizing, the contribution of background noise from the data signal is priority. The electronic noise may interfere with the signal processing and distort the spatial and temporal features of MHD modes. The unwanted noisy components can be filtered out numerically using special algorithms (e.g. SVD), or by using some low-pass filters to improve the quality of data. Secondly, any significant DC offset should be eliminated. DC offset may appear in SVD output as a single $m = 0$ mode with a noisy PC which may be misinterpreted as an unpaired MHD mode. Finally, normalizing each data channel between -0.5 and 0.5 is a standard procedure, particularly for SVD analysis for the reasons mentioned earlier. Absence of normalization may lead to uncertainty in interpreting SVD results.

SVD analysis may behave unexpectedly in tokamaks with different geometries and operational conditions. In some tokamaks (e.g. the DIII-D tokamak), SVD analysis succeeded in extracting the coherent MHD modes as distinct pairs [95], while it failed to arrange MHD modes as separate pairs in studies conducted in other tokamaks. For example, in the ADITYA tokamak, the coherent modes were identified as unpaired modes with prominent distortion in spatial structures and temporal evolutions [96]. In the STOR-M tokamak, SVD analysis has shown that MHD modes can be paired or unpaired depending on the discharge conditions. The SVD algorithm is now the main technique employed in STOR-M for processing the Mirnov signals. FCC and FCD analyses are occasionally implemented to validate and confirm the results of the MHD modes extracted by SVD analysis.

A typical normal ohmic discharge #204615 was selected to study the coherent structures of MHD activities that exist during STOR-M normal operation. The key discharge parameters are listed as follows: a duration of 33 ms, plasma current $I_p = 18$ kA, toroidal field $B_\phi \leqslant 0.7$ T, loop voltage $V_p \sim 3.5$ V and calculated edge safety factor $q(a) \sim 5$. The waveforms of this discharge are shown in Figure 6.9. Shown in the diagram are: plasma current I_p, loop voltage V_p, line-averaged electron

density n_e, horizontal plasma displacement ΔH, safety factor at the plasma edge $q(a)$, Mirnov oscillations and SXR emission. In this diagram, three time windows with 1 ms duration are marked as (1) 13-14 ms, (2) 21-22 ms and (3) 29-30 ms during the early, middle, and later parts of the plasma current plateau phase. The behaviors of the MHD fluctuations during those 1 ms time spans were analyzed by SVD and the results are presented. The Mirnov signals were collected at different poloidal and toroidal locations via Mirnov arrays. Two data matrices were assembled, one obtained by the poloidal Mirnov array 1 for poloidal SVD analysis, and another by the toroidal array for the toroidal analysis. Similar analyses were also performed for each 1 ms time span during the plasma current plateau phase (10-32 ms) and the results are tabulated.

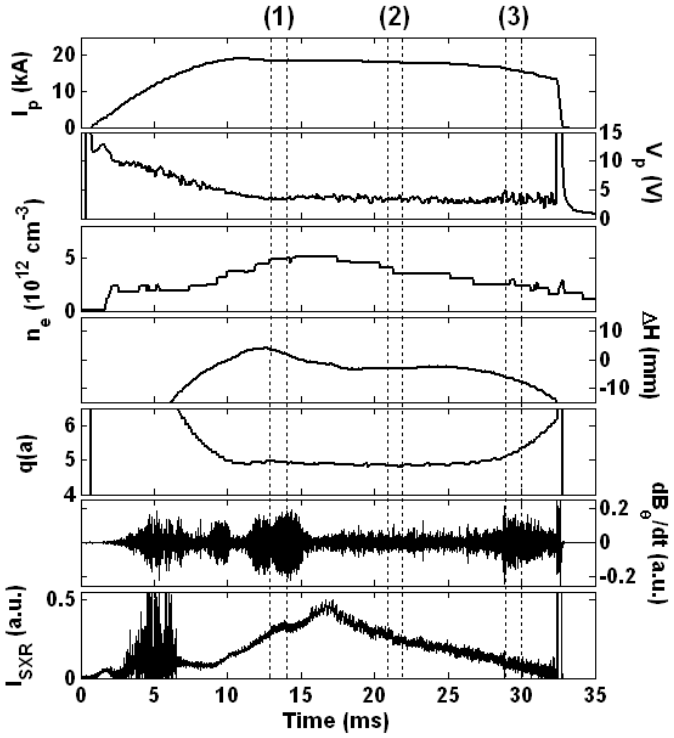

Figure 6.9: Waveforms of plasma parameters during the normal discharge #204615.

The first detailed SVD analysis was carried out for the time segment 13-14 ms immediately after plasma current reached the plateau phase. The panel on the left in Figure 6.10(a) shows the SV spectrum with two paired modes for the poloidal array and the corresponding PA and PC are shown in Figure 6.10(b). The paired modes can be identified as an $m = 2$ mode as shown in the spatial structure represented by the principle axis. The PC evolution shows that the mode oscillates rather

uniformly at a frequency of 23 kHz. The mode increases slightly in amplitude at the first 200 ms and then reaches a relatively stable amplitude. The oscillation can be viewed as the mode observed by one of the coils at a fixed poloidal location while the MHD perturbation structure rotates in the poloidal direction. If the MHD perturbation associated with the $m = 2$ mode is adhered to the rigid plasma column, the observed poloidal mode rotation frequency (23 kHz) would be twice the poloidal rotation frequency of the plasma column (only 12,500 rotations per second).

The panel on the right in Figure 6.10(a) shows the SV spectrum for the toroidal array and the corresponding PA and PC are shown in Figure 6.10(c). SVD extracted a pair of toroidal modes although one of the modes fluctuates with a 25% lower amplitude. The diagram shows that the dominant toroidal mode is $n = 1$ which oscillates at the same frequency as the poloidal mode (23 kHz). This is a clear indication that the dominant poloidal and toroidal modes during this time span are in fact one magnetic island (2, 1). The amplitude of the $n = 1$ oscillations behaves similarly to that of the poloidal oscillations since the MHD activities are global in nature.

The second analysis window (21-22 ms) was chosen at the middle of plasma current plateau. The poloidal and toroidal SVD analyses revealed a thread of unpaired MHD modes as depicted in Figure 6.11(a). The unpaired poloidal mode is spatially and temporally presented in Figure 6.11(b). The poloidal mode is readily identified as an $m = 4$ mode. The frequency of the $m = 4$ mode can be extracted by performing a WT analysis on the PC waveform. Figure 6.12(a) shows the WT spectrum of the corresponding PC which peaks at multiple frequencies. The $m = 4$ mode appears on the spectrum between $t = 21.2$ ms and $t = 21.6$ ms with a substantial increase in frequency from 33 kHz to 43 kHz. The peak frequency of a mode can be defined as the frequency at which the mode oscillates with the highest amplitude and for the longest duration [97]. In that regard, the peak frequency of the $m = 4$ mode is about 33 kHz.

The SVD analysis encountered a difficulty in extracting the dominant toroidal mode since it has noisy features. The dominant toroidal mode was identified by the SVD analysis as an unpaired $n = 2$ mode. Figure 6.11(c) displays the spatial and temporal structures of the $n = 2$ mode. The WT analysis was also carried out for the time evolution of the $n = 2$ mode. As shown in Figure 6.12(b),

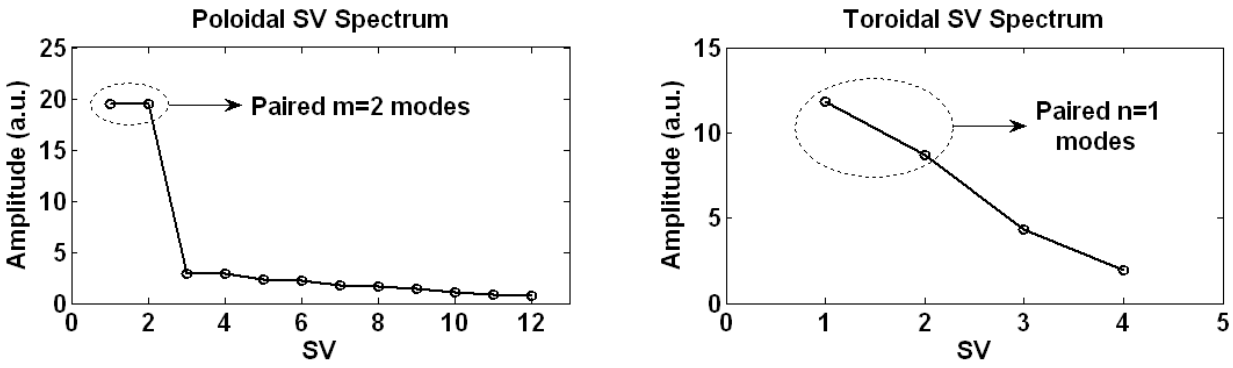

(a) Poloidal and toroidal SV spectra.

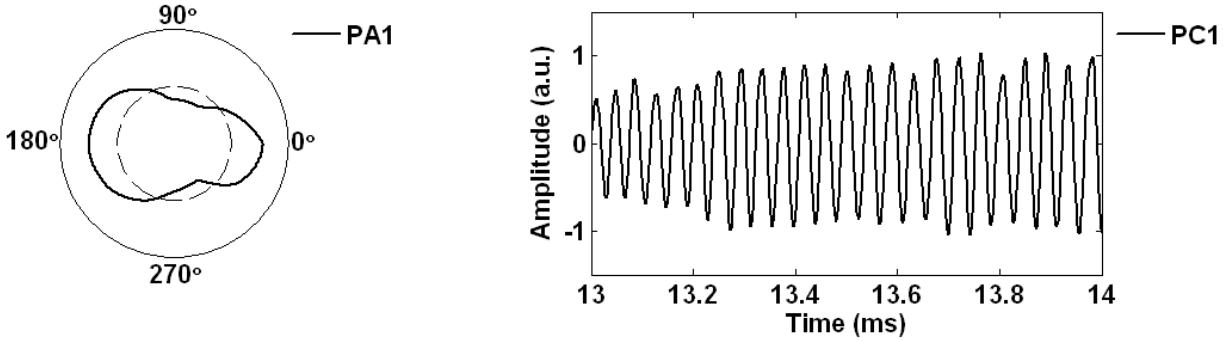

(b) Spatial and temporal structures of the dominant poloidal mode.

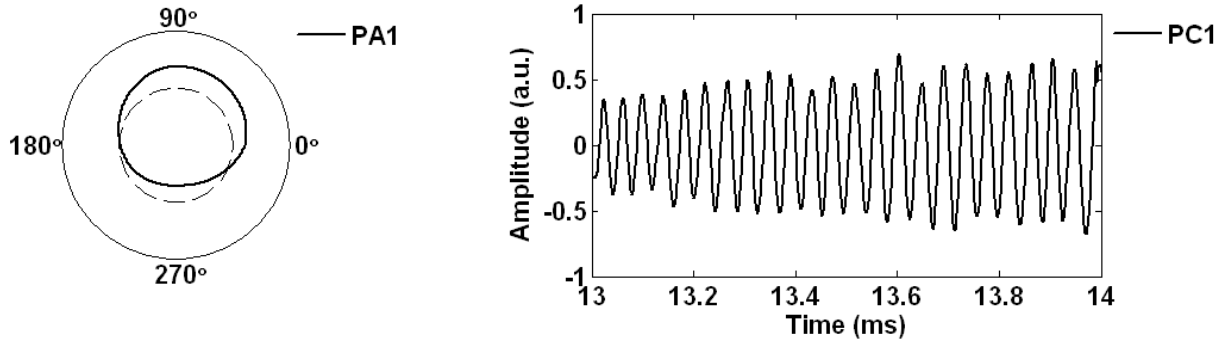

(c) Spatial and temporal structures of the dominant toroidal mode.

Figure 6.10: SVD analysis for the time segment 13-14 ms.

the WT spectrum suggests that the toroidal mode rotates irregularly at peak frequency $\sim$ 18 kHz. It is evident from the frequency difference between the $m = 4$ and $n = 2$ modes that they associate with different magnetic surfaces.

A possible explanation for extracting dominant poloidal and toroidal modes located on different surfaces is owing to how the SVD algorithm decomposes the MHD modes. As pointed out before, SVD arranges the modes on the SV spectrum in descending order relative to their amplitudes, so that the dominant mode has the highest amplitude. However, the poloidal and toroidal modes oscillating at the same frequency on the same surface does not necessarily mean that they are both dominant as one mode may oscillate with a higher amplitude than the other [98]. In this time segment (21-22 ms), it is likely that the toroidal mode accompanying the dominant poloidal mode (i.e. $m = 4$) may have a relatively lower amplitude than the dominant toroidal mode (i.e. $n = 2$) and vice versa. The structures of the dominant modes are deformed due to the fact that the amplitude of MHD oscillations is not significantly larger than the noise.

The last detailed SVD analysis was performed during the period 29-30 ms before the plasma ramp-down phase. SVD analysis identified a paired poloidal mode $m = 2$ and unpaired toroidal mode $n = 1$ according to SV spectra shown in Figure 6.13(a). The PA and PC plots of the dominant poloidal mode are illustrated in Figure 6.13(b). The poloidal mode seems to have a complicated $m = 2$ structure. As shown in Figure 6.14, the spatial Fourier spectrum of the PA justifies the distortion of $m = 2$ mode as a weak coupling with $m = 1$ and $m = 3$ modes. The $m = 2$ pair oscillates at a prominent frequency of 34 kHz. The panels in Figure 6.13(c) display the eigenvectors of $n = 1$ mode in both space (PA) and time (PC). The unpaired $n = 1$ mode oscillates at a frequency of 34 kHz, similar to that of the poloidal pair. This (2, 1) magnetic island corresponds to those on the $q = 2$ surface. Clear modulations in both amplitude and frequency occurring in PCs may be attributed to the mode coupling.

Table 6.3 lists the results of SVD analysis for Mirnov signals for every 1 ms time window during the plasma current plateau. The parameters listed in the table are: time window, poloidal mode number and poloidal peak frequency, as well as toroidal mode number and toroidal peak frequency.

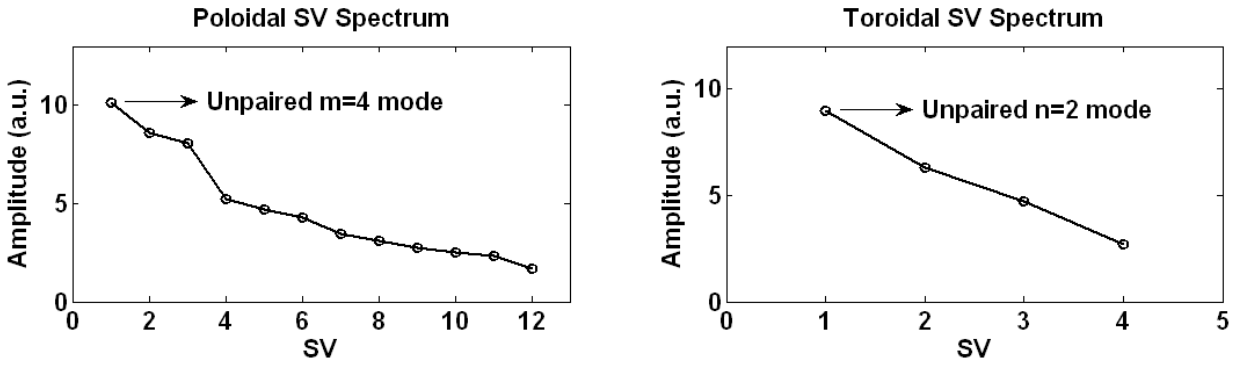

(a) Poloidal and toroidal SV spectra.

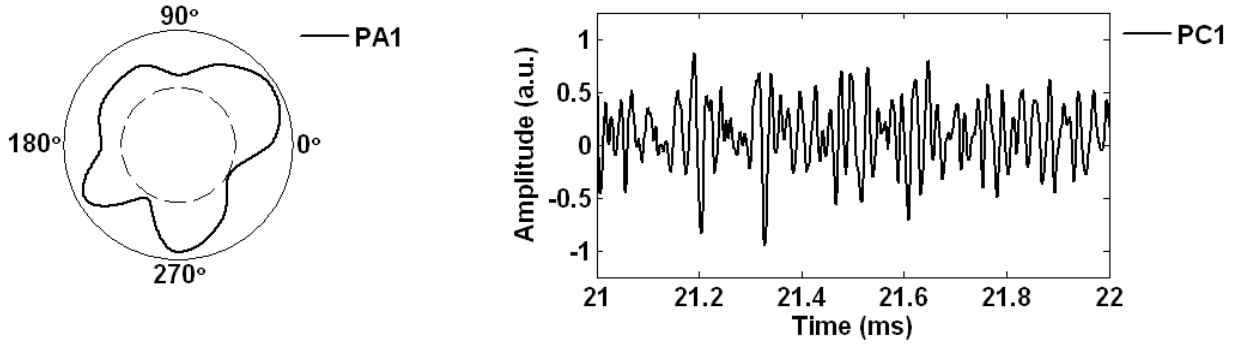

(b) Spatial and temporal structures of the dominant poloidal mode.

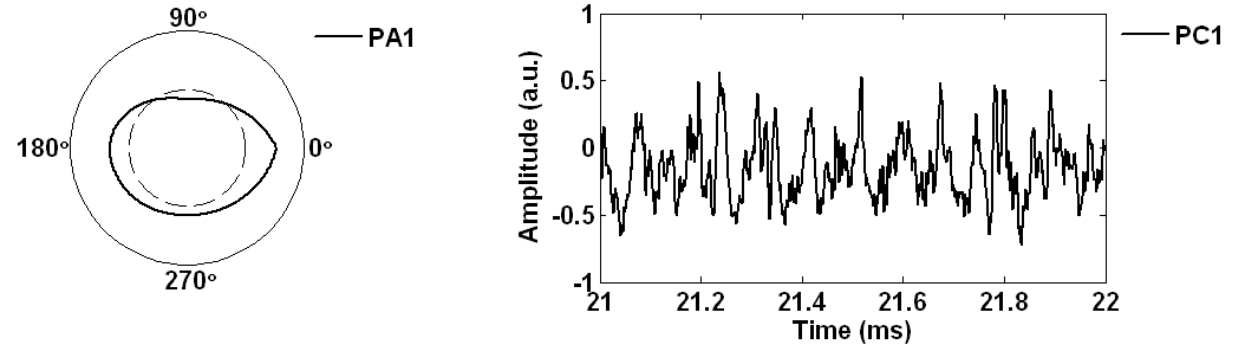

(c) Spatial and temporal structures of the dominant toroidal mode.

Figure 6.11: SVD analysis for the time segment 21-22 ms.

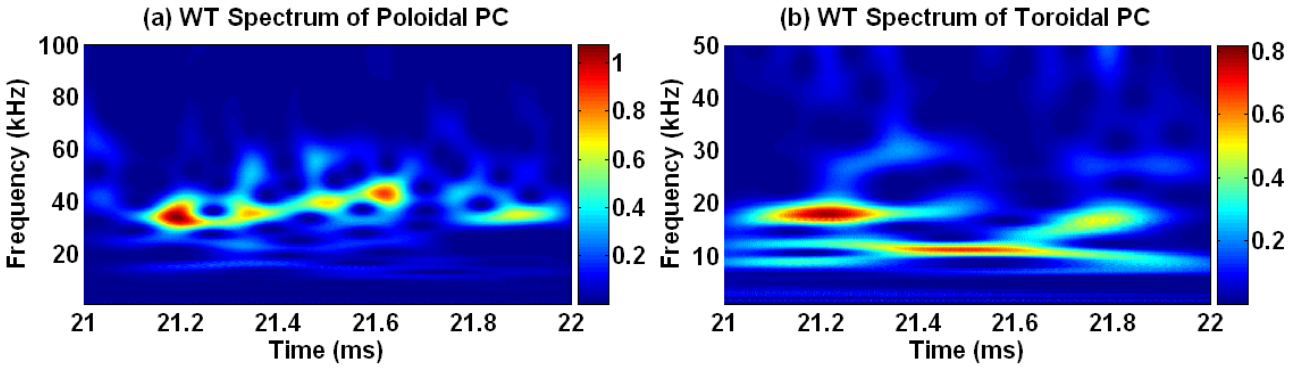

Figure 6.12: WT spectra of the dominant PCs in the time segment 21-22 ms.

Immediately after the formation of the plasma current plateau (10-11 ms), two uncorrelated modes, $m = 3$ and $n = 2$, emerge with peak frequencies of $f_m = 25$ kHz for the poloidal mode and $f_n = 14$ kHz for the toroidal mode. At the beginning of plasma plateau (11-15 ms), the poloidal mode $m = 3$ makes a structural transition to the $m = 2$ mode while its frequency remains almost intact. However, the toroidal mode number is reduced from $n = 2$ to $n = 1$ with a much higher frequency ($f_n = 24$ kHz). In this regime, the magnetic islands tend to resonate on the $q = 2$ magnetic surface where the poloidal and toroidal modes oscillate at the same frequency.

The MHD modes located in the middle of the plasma flat-top (15-23 ms) are characterized by low fluctuations and high rotating frequency in the poloidal direction. As discussed earlier, it was a challenge for the SVD analysis to extract usable information about the dominant modes because of the low signal-to-noise ratio. The dominant modes extracted in this time regime are unrelated as they oscillate at different frequencies, therefore they correspond to different magnetic surfaces. During the plasma flat-top phase, the dominant modes are verified as a poloidal $m = 4$ mode and a toroidal $n = 2$ mode. The modes oscillate at maximum frequencies $f_m = 39$ kHz and $f_n = 25$ kHz. In the time segment 23-24 ms, the SVD analysis revealed an $m = 1$ mode which is located near the $q = 1$ core region. This mode lasts for a short time before it is subsided by the fluctuations induced by the $m = 2$ and $m = 3$ modes.

Before the plasma termination (28-32 ms), the localized poloidal MHD structure is sustained at $m = 2$, while the toroidal structure n alternates between 1 and 2. The highest poloidal and toroidal

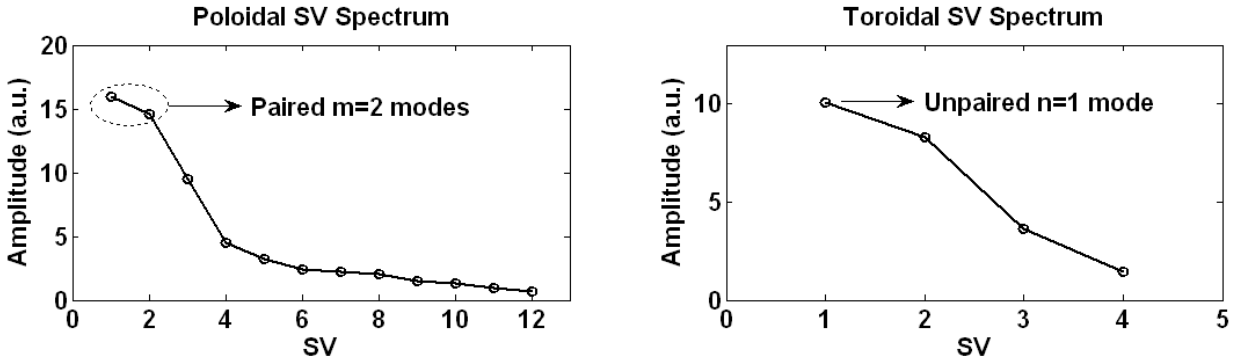

(a) Poloidal and toroidal SV spectra.

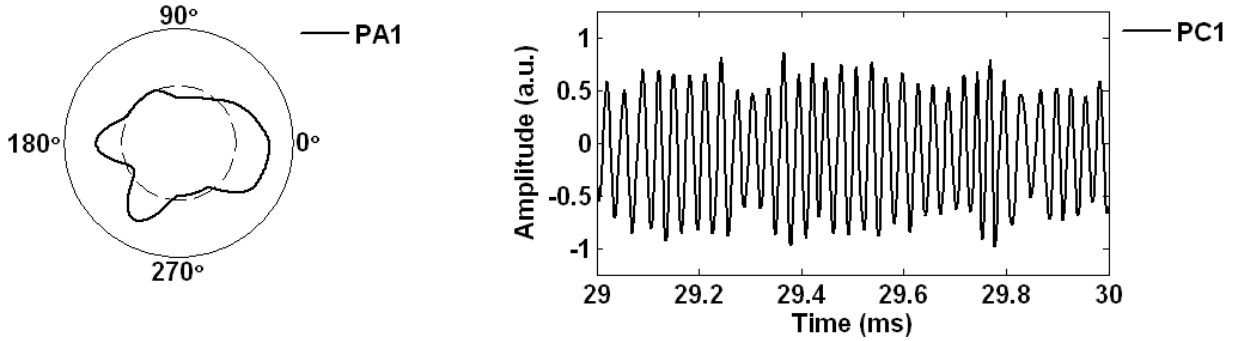

(b) Spatial and temporal structures of the dominant poloidal mode.

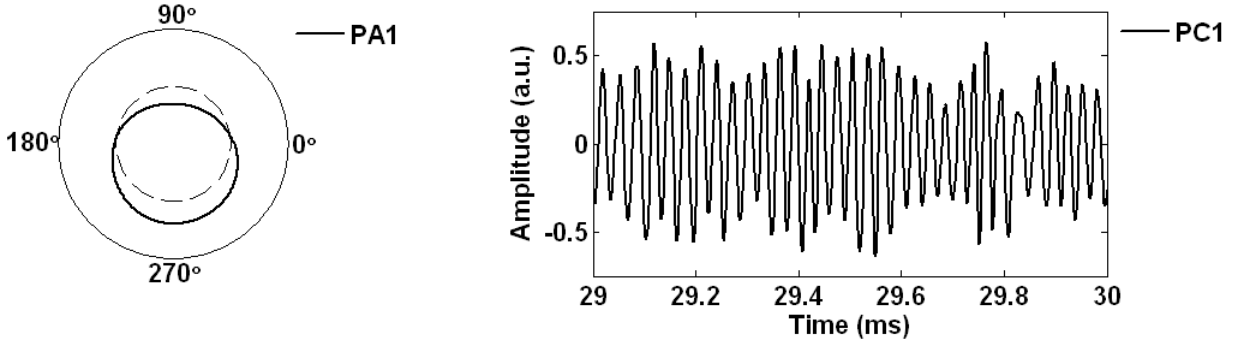

(c) Spatial and temporal structures of the dominant toroidal mode.

Figure 6.13: SVD analysis for the time segment 29-30 ms.

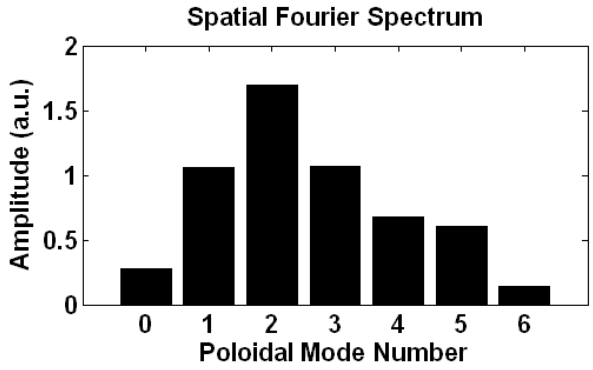

Figure 6.14: Spatial Fourier spectrum of the coupled poloidal mode in the time segment 29-30 ms.

peak frequencies observed during the whole discharge, being $f_m = 40$ kHz and $f_n = 36$ kHz, respectively, are recorded prior to the plasma ramp-down phase. The q-value of perturbed magnetic surfaces in this regime is reported between 1 and 2.

Window (ms)	m	f_m (kHz)	n	f_n (kHz)	**Window** (ms)	m	f_m (kHz)	n	f_n (kHz)
10-11	3	25	2	14	21-22	4	33	2	18
11-12	2	24	1	24	22-23	4	39	2	25
12-13	2	24	1	24	23-24	1	15	2	29
13-14	2	23	1	23	24-25	2	33	2	15
14-15	2	22	1	22	25-26	3	34	2	19
15-16	2	25	2	17	26-27	2	34	2	17
16-17	4	25	2	13	27-28	3	37	2	20
17-18	4	37	2	16	28-29	2	34	2	33
18-19	4	32	2	13	29-30	2	34	1	34
19-20	4	39	2	14	30-31	2	32	2	32
20-21	4	36	1	14	31-32	2	40	1	36

Table 6.3: Complete SVD diagnosis for the plasma plateau regime (10-32 ms) during the normal discharge #204615.

6.4 Compact Torus Injection

It has been reported in early experiments that after using tangential CT injection into STOR-M, $m = 2$ oscillations were suppressed while $m = 3$ oscillations remained unaffected during the H-mode-like discharges [99]. The improved confinement phase (H-mode) is labeled by an increase in electron density n_e, suppression in radiation intensity H_α, increase in the global confinement time τ_E and reduction in the floating potential fluctuations $\tilde{V}_f$ [100]. High SXR emission from the hot plasma core has been observed during the H-mode induced by vertical CT injection [101].
In recent CT studies, an increase has been noticed in both $m = 2$ and $m = 3$ oscillations before the termination of the transient improved confinement, raising a question whether the high amplitude of Mirnov oscillations is a direct or indirect precursor for the H-L back transition in STOR-M [102]. Figure 6.15 shows the waveforms of STOR-M discharge #182960 with a CT injected at 15.25 ms during the plasma flat-top phase. CT injection did not cause any visible changes in plasma current I_p and loop voltage V_p as the plasma position ΔH shifted outward.

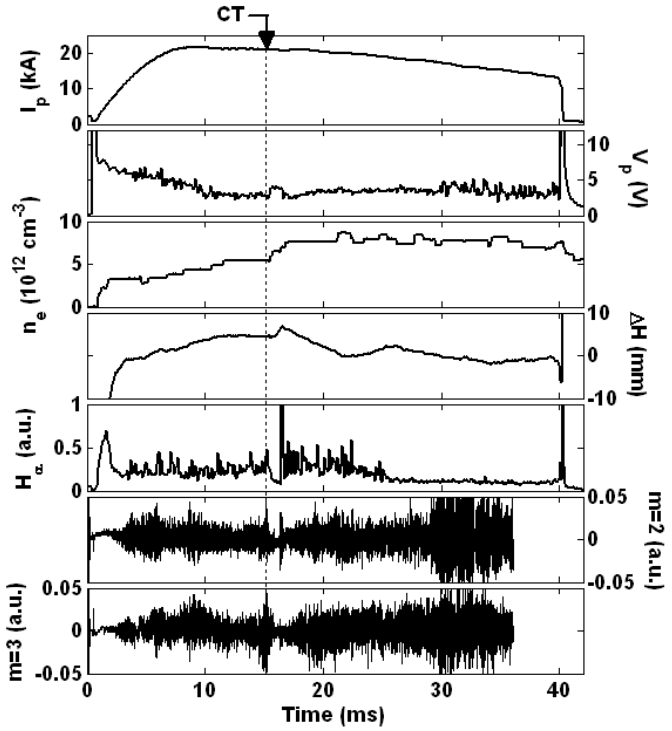

Figure 6.15: Waveforms of plasma parameters during the normal discharge #182960 with a CT injection at 15.25 ms.

Figure 6.16 shows the time evolution of the Mirnov signal (inboard coil 1-7) and the corresponding WT spectrum. The noise spike marked on the Mirnov signal at 15.25 ms indicates the exact firing instance of the compact toroid into the tokamak discharge. The WT spectrum depicts the magnetic fluctuation characteristics on the time-frequency plane. CT injection caused a phase of suppressed MHD oscillations between 15.6 ms and 16.2 ms as a result of inducing an H-mode-like phase. However, the suppression phase was terminated by a spike in the Mirnov signal (appears as a hot spot on the WT spectrum) followed by coherent oscillations which lasted for 0.4 ms between 16.2 ms and 16.6 ms. Three time segments were chosen for analysis which are tagged by (1), (2) and (3) on the Mirnov trace. SVD analysis was performed on the first and second time segments, which are orderly located before CT injection and during the H-mode-like phase. The reoccurrence of Mirnov oscillations, appearing in the third time segment, was investigated in more detail using the poloidal FCD and SVD analyses.

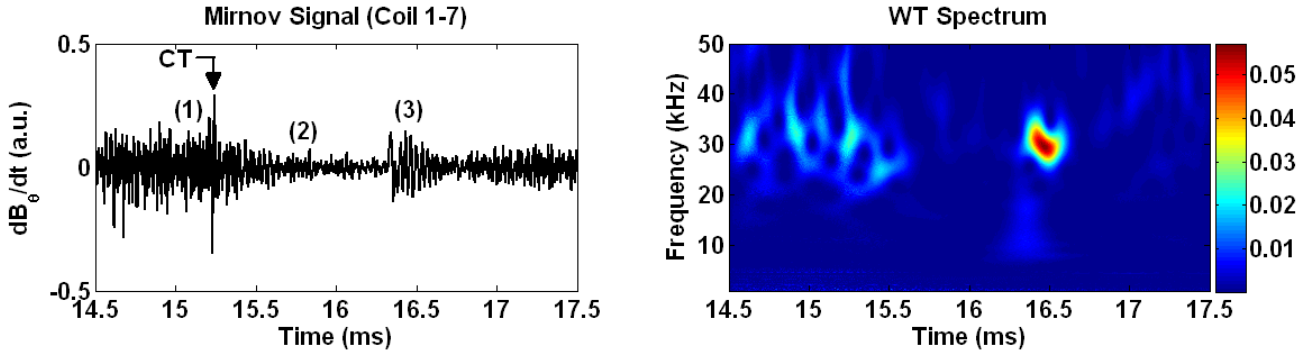

Figure 6.16: Mirnov oscillations and WT power spectrum immediately before and after the CT injection.

Before the CT injection, the dominant poloidal mode in the time window 14.8-15.2 ms was verified by SVD as $m = 4$. The diagram on the left hand side of Figure 6.17 is a polar plot of the dominant $m = 4$ mode. The temporal evolution of the $m = 4$ mode, shown in the right hand side panel in Figure 6.17, has a noisy waveform with a peak frequency of 32.5 kHz.

After the CT injection, the MHD oscillations were suppressed nearly to the noise level during the H-mode-like phase. Interestingly, the poloidal SVD analysis was able to extract a distorted pair of $m = 3$ modes which dominates during the entire time window 15.6-16 ms. The spatial and

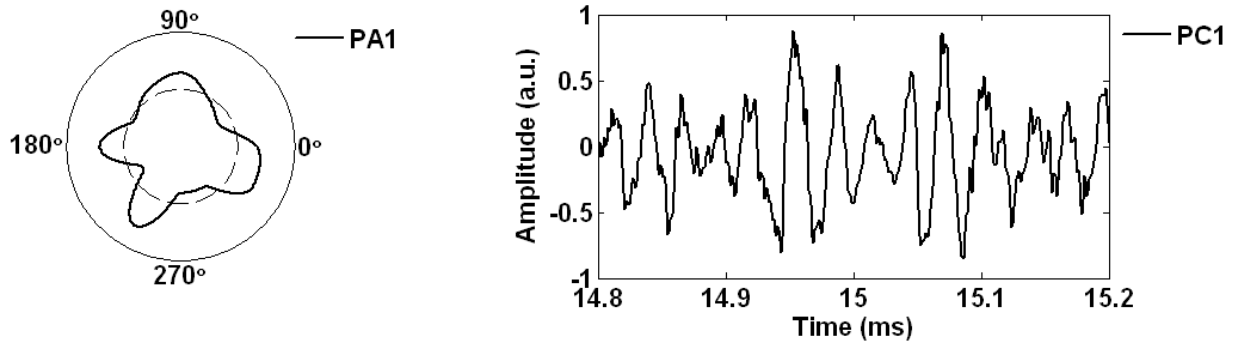

Figure 6.17: Spatial and temporal structures of the dominant poloidal mode in time segment 14.8-15.2 ms.

temporal information of $m = 3$ mode is presented in Figure 6.18. The $m = 3$ pair oscillates at a peak frequency of 25 kHz.

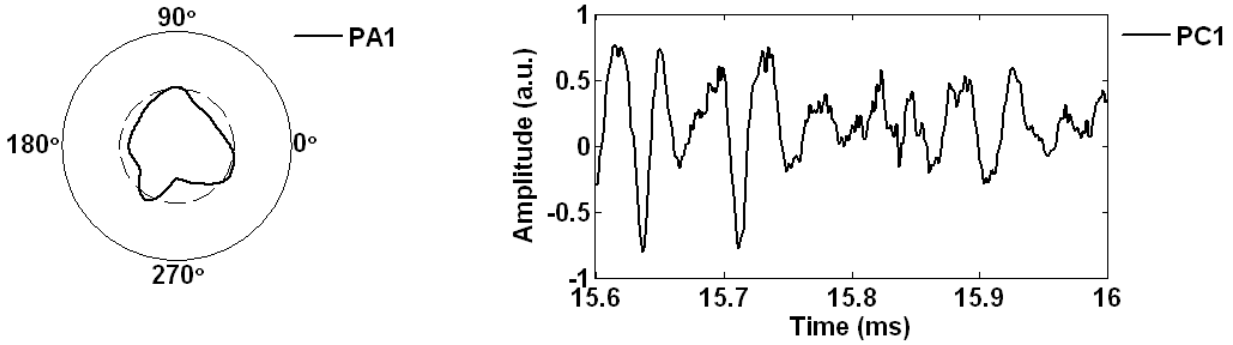

Figure 6.18: Spatial and temporal structures of the dominant poloidal mode in time segment 15.6-16 ms.

1 ms after injecting the CT, the Mirnov fluctuation level returned to the original level prior to the CT injection. The left diagram in Figure 6.19 is a color-coded contour plot of the raw Mirnov signals near the time when the MHD oscillations reappear (16.2-16.6 ms). The panel on the right is a screw-like 3D representation (azimuthal coordinate (θ): poloidal angle, radial coordinate (color bar): signal amplitude) suggesting helical motion of a certain magnetic island. Both plots point to a rotating structure of coherent oscillations.

To study the details of the MHD oscillations during the reappearance phase, FCD analysis was performed on the Mirnov signals collected by the poloidal array 1 for the time window between 16.2 ms and 16.6 ms. FCD identified two dominant modes in this time segment, $m = 1$ and $m =$

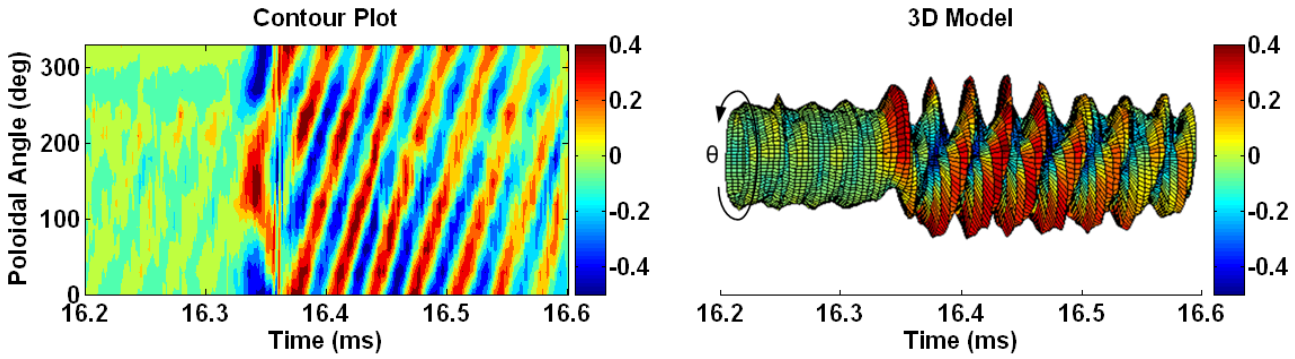

Figure 6.19: Contour plot and 3D representation of the Mirnov oscillations within the time segment 16.2-16.6 ms.

2. The FCD magnitudes of $m = 1$ and $m = 2$ modes are shown in Figure 6.20. The FCD spectrum shows a jump in $m = 1$ magnitude between 16.32 ms and 16.35 ms followed by the $m = 2$ mode.

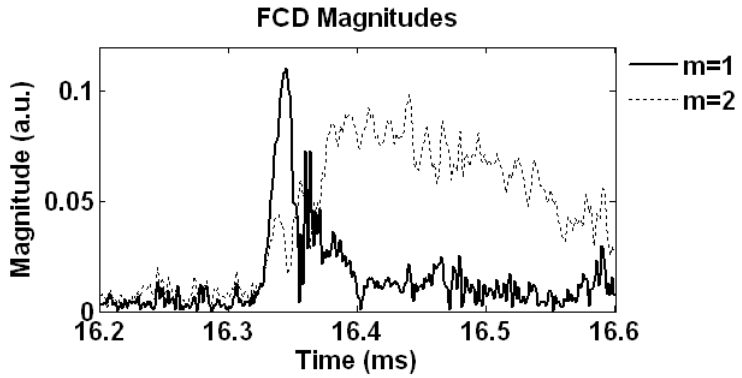

Figure 6.20: FCD analysis for the time segment 16.2-16.6 ms.

The poloidal SVD analysis was also used to examine the reappearance phase which revealed 3 significant modes on the SV spectrum as shown in Figure 6.21(a). The first two SVs represent a paired magnetic structure $m = 2$ with high coherent oscillations starting at $t = 16.35$ ms. The sine and cosine components of the $m = 2$ mode are plotted on the same polar diagram in Figure 6.21(b) to demonstrate the phase difference of the $m = 2$ pair. The corresponding PCs of the $m = 2$ pair shown in the right panel of Figure 6.21(b) also exhibit the same intrinsic phase shift. The frequency of the coherent oscillations is around 30 kHz. The third unpaired dominant mode is spatially identified as an $m = 1$ mode as is shown in the polar plot of Figure 6.21(c). This mode does not have the usual properties of a traveling wave because it appears and vanishes within a

short period of time ($\sim$ 30 μs).

This kink-like instability shown in Figure 6.21(c) is similar to the gong mode, analogous with a gong being hit in its center by a hammer, which has been studied previously in the Joint European Torus (JET) and the TCA tokamaks [103]. The gong mode may rotate in poloidal and toroidal directions like any other MHD mode. However, its actual lifespan is shorter than the rotation period which explains the unpaired behavior of the gong mode in the SV spectrum. It is interesting that the magnetic activity equivalent to the gong mode had not been reported earlier in small tokamaks until recently in STOR-M [104, 105]. The gong mode can be easily observed in tokamaks with an inverse aspect ratio $\epsilon = \frac{a}{R} \sim 0.3$ ($\epsilon = 0.27$ in STOR-M) as the mode coupling in these machines may be responsible for detecting the gongs at the plasma edge. In an experimental environment, the gong mode appears at the edge as an asymmetric bursting perturbation in the poloidal magnetic field that usually accompanies the sawtooth crash phenomenon.

Although the toroidal structure of the gong perturbation was constantly measured as $n = 1$, its poloidal topology was found to be equal to the integer part of the safety factor at the last enclosed surface $q(a)$. In the JET tokamak, the maximum m value of the gong mode was found to be 4 for $q(a) = 4.2$, though low values of m between 1 and 3 have been transiently observed [76]. The poloidal gong structure was also reported as $m = 3$ in the Tore Supra tokamak which is reasonably consistent with $q(a)$ measured at the plasma edge ($= 3.4$) [106]. In the STOR-M tokamak, the q-value calculated at the plasma periphery was reported as $q(a) = 4.5$ [107]. The measured gong mode $m = 1$ is located near the $q = 1$ surface indicating that in some cases the inner gongs might be stronger than the ones at the outer q surfaces.

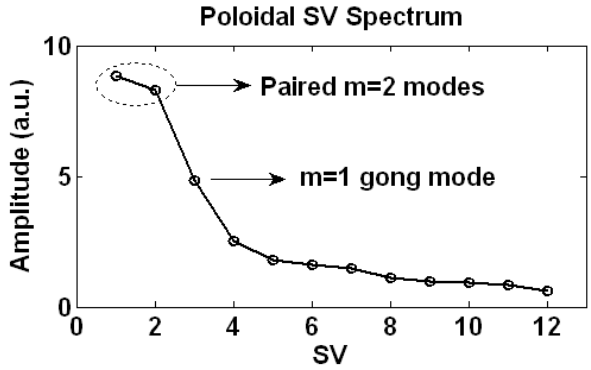

(a) Poloidal SV spectrum.

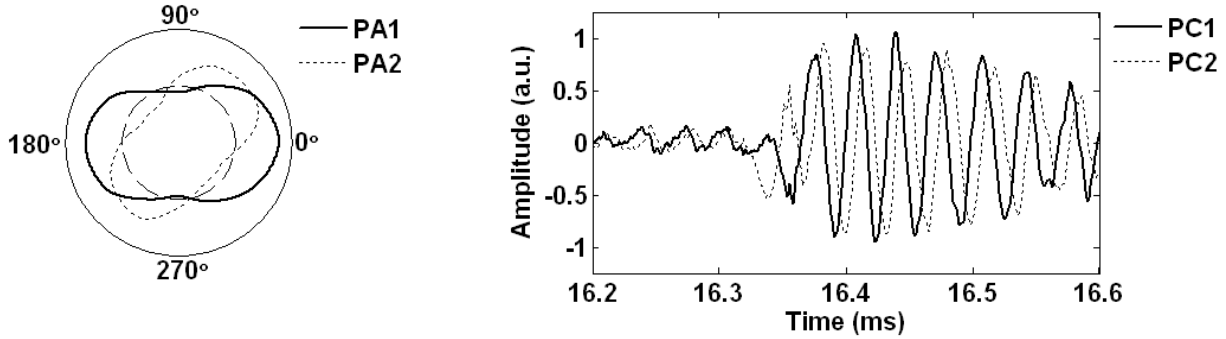

(b) Spatial and temporal structures of the dominant $m = 2$ poloidal mode.

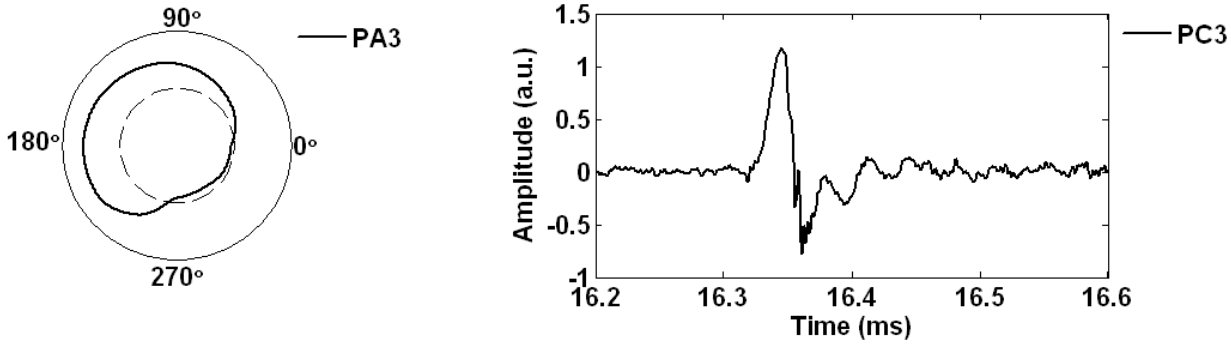

(c) Spatial and temporal structures of the $m = 1$ gong mode.

Figure 6.21: SVD analysis for the time segment 16.2-16.6 ms.

6.5 Mode Amplitude Modulations

The MHD fluctuations are by no means stationary. For example, the (1, 1) magnetic island on the $q = 1$ surface grows with time. Once the accumulated energy in the island is large enough, a minor internal disruption occurs causing a sudden outward heat flow and the termination of the (1, 1) island. As the plasma core is heated again and the current density steepens, the island reappears and grows until it crashes again. The amplitude modulation accompanying the sawtooth oscillations is a well-known phenomenon [108]. Similar phenomenon happens also to the (2, 1) island in the example to be analyzed. In this section, it will be shown that the SVD and FCC analyses can still be utilized to extract the basic spatial and temporal structures of the MHD fluctuations in the STOR-M tokamak. Figure 6.22 shows a modulated Mirnov oscillation signal and the corresponding WT spectrum for the STOR-M discharge #203932. The WT plot shows that the oscillation frequency is relatively stable although the amplitude changes drastically.

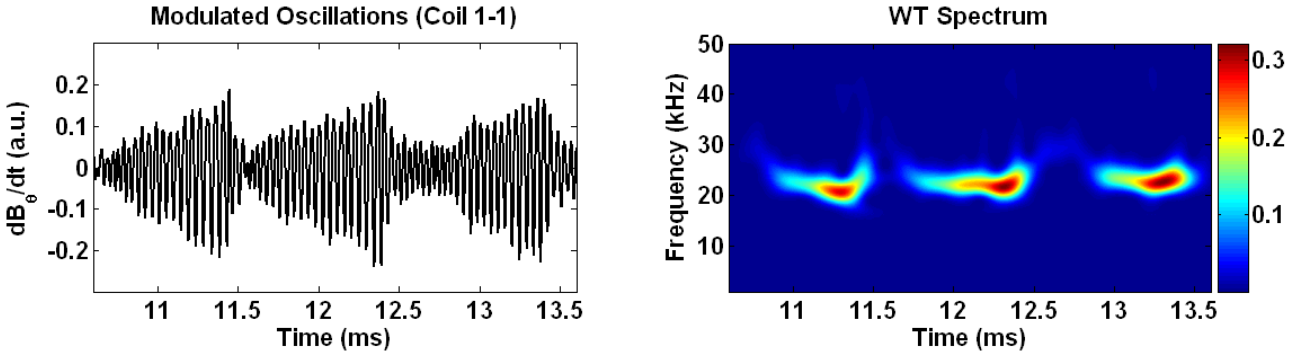

Figure 6.22: WT power spectrum of the modulated Mirnov oscillations during the normal discharge #203932.

The modulated Mirnov oscillations during the time interval 10.6-13.6 ms were studied using FCC analysis. Figure 6.23(a) illustrates the phase difference of Mirnov oscillations at a coherent frequency of 22 kHz for the coils at various poloidal locations. This diagram states that the phase increases nearly linearly with the poloidal angle where the Mirnov coils are located. It also shows that the phase changes by approximately 4π as the poloidal angle advances 2π, indicating that the mode is $m = 2$ in nature. Likewise from Figure 6.23(b), the toroidal FCC phase at the coherent frequency 22 kHz suggests that the toroidal mode number is $n = 1$. The phases slightly deviate

from the ideal straight line (dotted line). The deviations are likely caused by Mirnov coils 3-1 ($\pm 62^{\circ}$) and 4-1 ($\pm 50^{\circ}$) on the thick wall since the numerical phase delay correction discussed in Subsection 5.3.4 may be inaccurate.

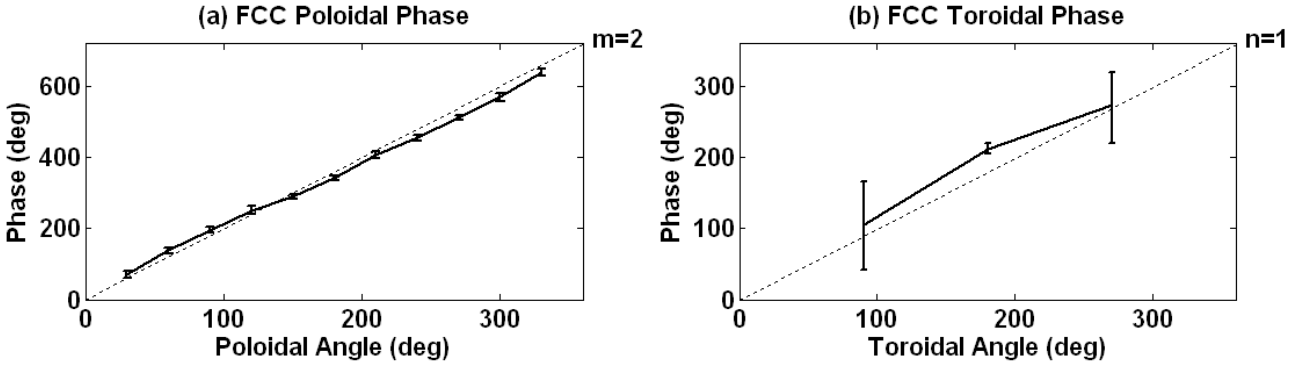

Figure 6.23: FCC analysis for the modulated Mirnov oscillations.

The SVD analysis was also performed on the same time window 10.6-13.6 ms to obtain the exact spatial structure of the modulated Mirnov oscillations. The SVD analysis revealed paired $m = 2$ modes for the poloidal array (Figure 6.24(a)) and paired $n = 1$ modes for the toroidal array (Figure 6.24(b)). The mode numbers suggest that the observed MHD modes correspond to a (2, 1) magnetic island propagating on the $q = 2$ surface. The PC plots for the dominant MHD modes show that the island grows gradually for about 1 ms and diminishes suddenly. The FT analysis of PCs identified the same frequency (23 kHz) for both poloidal and toroidal modes, coinciding with the FCC results within the error bars.

6.6 Mirnov-SXR Correlation Analysis

The central channels (V5, V6 and V7 in Figure 5.13) in the SXR arrays recorded clear sawtooth oscillations. Figure 6.25 shows the expanded traces of the SXR signals from two channels near the plasma center. The signal from the V5 channel shows clear sawtooth oscillations associated with the (1, 1) magnetic perturbations. The V7 channel shows inverted sawtooth oscillations, indicating that the $q = 1$ surface is located somewhere between the V5 and V7 channels.

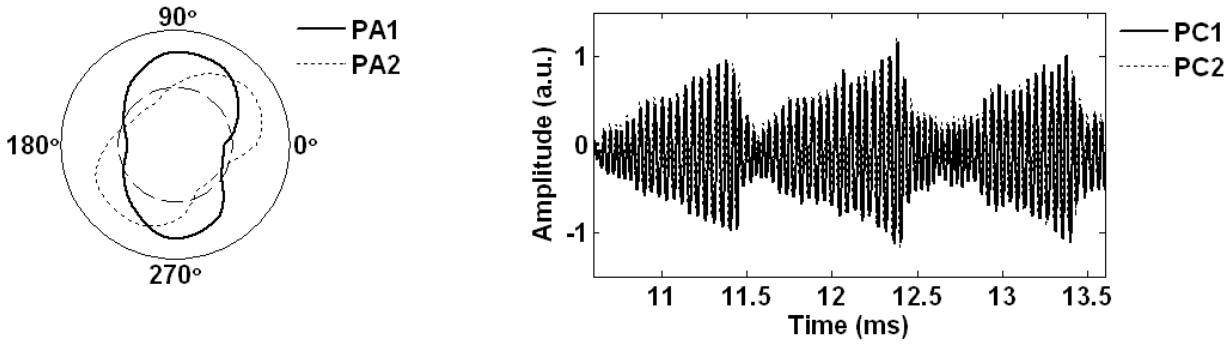

(a) Spatial and temporal structures of the poloidal pair.

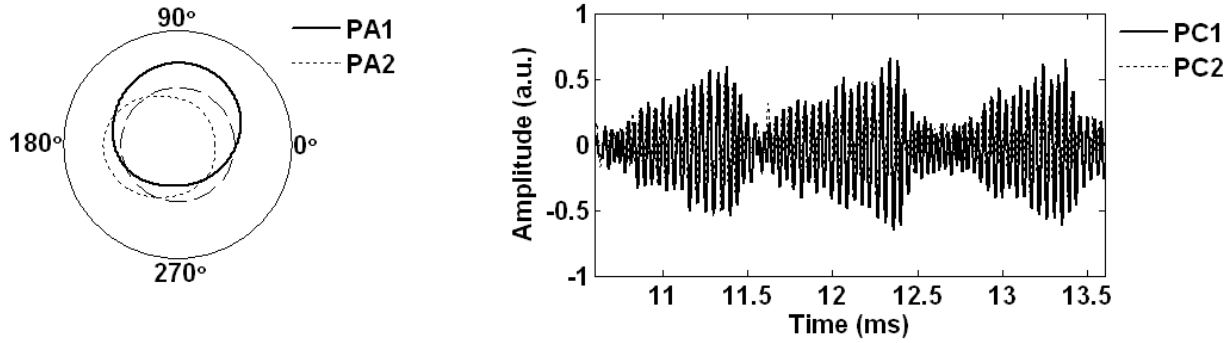

(b) Spatial and temporal structures of the toroidal pair.

Figure 6.24: SVD analysis for the modulated Mirnov oscillations.

It was observed that high frequency oscillations are superimposed on sawtooth oscillations. Those oscillations are highly correlated with the magnetic fluctuations detected by the Mirnov coils. It was also observed that clear sawtooth oscillations occur only when the magnetic fluctuations are relatively weak. Figure 6.26 displays the waveforms and WT power spectra of the magnetic fluctuations and high frequency SXR oscillations during the sawtooth-free phase. Both fluctuations have the same stable frequency of about 23 kHz. The relative intensity of the high frequency SXR oscillations decreases as the relative intensity of the magnetic fluctuations increases and vise versa. According to the SVD analysis, the spatial structure of the magnetic fluctuations corresponds to the (2, 1) magnetic island (the same discharge was analyzed earlier in Section 6.3).

Figure 6.27 shows the auto-power and the coherence spectra of the Mirnov and SXR oscillations which are calculated by FCC analysis. The auto-power spectra peak at the same frequency (23 kHz) and the coherence coefficient near that frequency peaks to a value of 0.99. The high coherence of

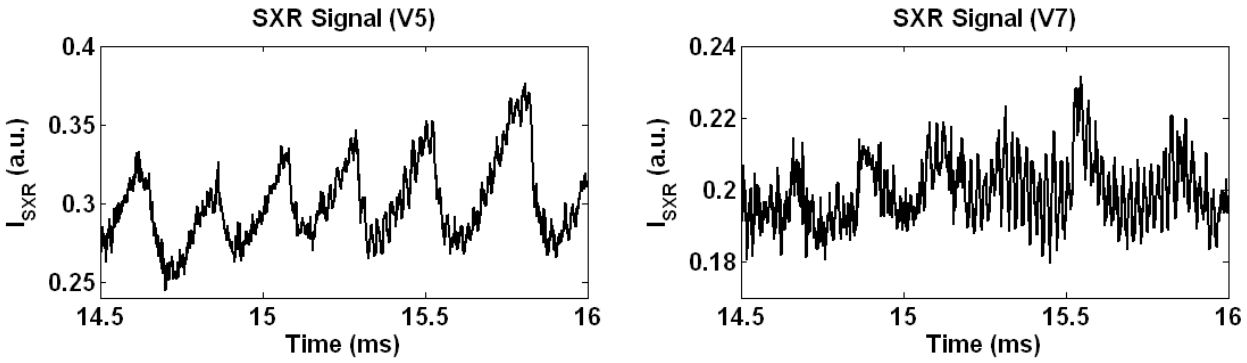

Figure 6.25: SXR emissions measured through two chords near the STOR-M center during the normal discharge #204428.

the Mirnov oscillations and SXR emission oscillations suggests that the plasma temperature and/or density within the magnetic islands are quite different from that outside the island because the SXR detector is sensitive primarily to electron temperature and density.

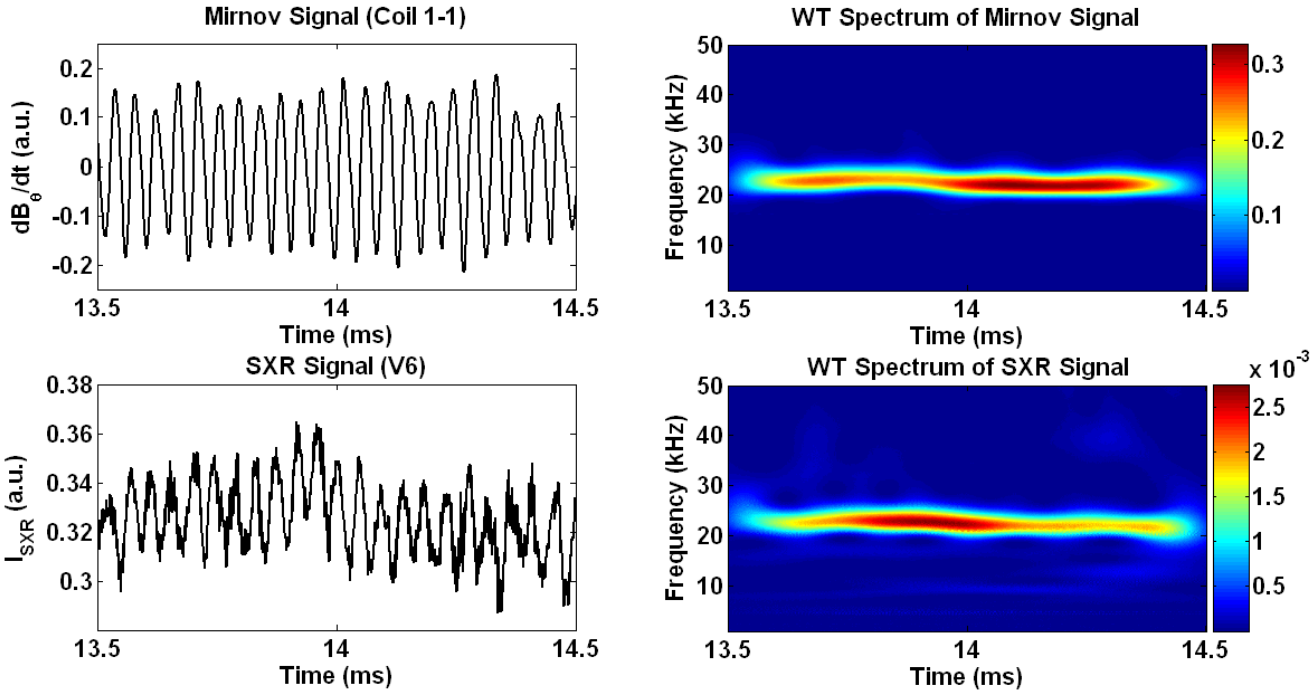

Figure 6.26: WT spectra of Mirnov and SXR signals recorded during the normal discharge #204615.

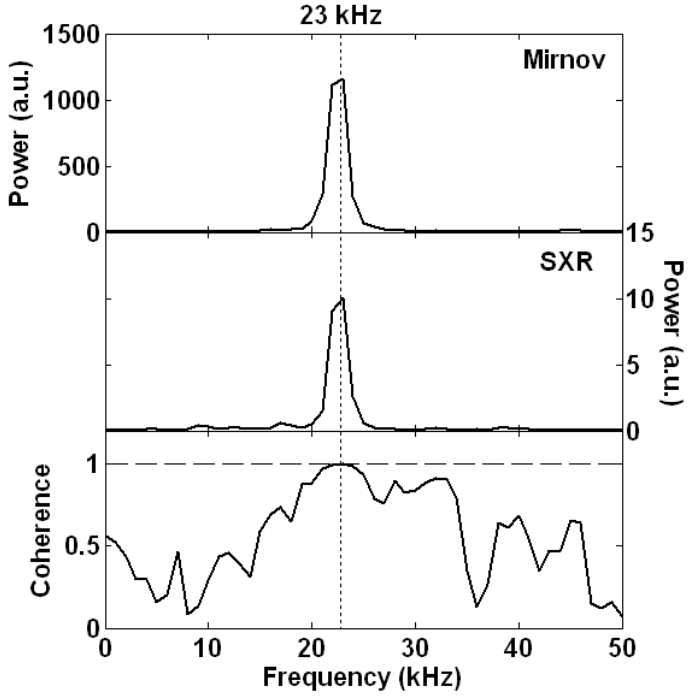

Figure 6.27: Auto-power spectra and coherence spectrum of the Mirnov and SXR signals.

Chapter 7

Summary and Future Work

7.1 Summary

MHD instabilities have unfavorable effects on particle and energy confinement in tokamaks and, under extreme conditions, may terminate the discharges. They usually grow along the helical magnetic field lines on the rational magnetic surfaces and are usually associated with magnetic islands. The non-ergodic configuration of magnetic field lines is characterized by the m and n mode numbers which specify the number of turns that a particular magnetic line has to make in the toroidal and poloidal directions before it closes onto itself. The result is a rational magnetic surface on which the (m, n) magnetic islands grow. The ratio $\frac{m}{n}$ corresponds to the rational order of the safety factor q.

In the STOR-M tokamak, the magnetic field oscillations and SXR emission fluctuations associated with MHD instabilities are monitored by Mirnov coils mounted on the exterior chamber wall and SXR cameras monitor line-integrated SXR emission intensity. STOR-M is equipped with two types of Mirnov coils, the pre-configured $m = 2$ and $m = 3$ coils and the discrete coils. The latter type consists of 32 coils arranged into four poloidal arrays. Two of these arrays (12 coils each) are installed at toroidal angles 0° and 180° on the thin bellows. They have spatial resolution for m mode numbers up to 6. The other two arrays are mounted on the thick wall of the vacuum chamber at toroidal angles 90° and 270°. The 4-coil toroidal array, which is composed of the outboard coil

of each poloidal array, can resolve toroidal mode numbers $n = 1$ and $n = 2$. The SXR system consists of two pinhole cameras, each camera contains 12 photodiodes. The cameras are inserted into STOR-M through horizontal and vertical ports separated by 90°.

A collection of signal processing techniques was utilized to analyze MHD signals recorded by the Mirnov coils and SXR detectors. Fourier analysis was employed to perform a basic time-to-frequency conversion. However, for some non-stationary signals, STFT or WT analyses were implemented to obtain a power spectrum resolved in both time and frequency domains. For the harmonic analysis, a combination of some modified Fourier analyses, such as FCC and FCD, was used. The SVD algorithm was used to reveal the spatial structure and the temporal evolution of the MHD perturbations. Before carrying out the analyses, Mirnov signals were digitally treated to remove any DC offset and to normalize the signals for SVD analysis. A technique was developed to apply phase corrections to the Mirnov signals recorded by the coils mounted on the thick chamber wall. Extracting the MHD harmonics from Mirnov signals was firstly done by either FCC or FCD before performing more complex analysis using SVD.

In order to bench mark the processing techniques, analyses were applied to artificial data series with known parameters. Two scenarios were considered in the simulations, decoupled MHD modes with distinct frequencies and coupled MHD modes. While FCC analysis failed to identify the coupled modes, SVD successfully decoupled individual mode with some spatial distortion. Furthermore, the numerical analyses were applied to a data set collected during normal STOR-M discharge. The data during the entire plasma current plateau phase were scanned by moving a 1 ms time window using SVD. The spatial structure of the dominant modes corresponded to poloidal mode numbers between 2 and 4 and toroidal mode numbers between 1 and 2. The temporal analysis also revealed that the poloidal modes were characterized by oscillations in the frequency range between 20 kHz and 40 kHz, while the toroidal modes oscillated at a frequency around $15 \sim 35$ kHz.

In the CT injection experiment, analysis of Mirnov signals revealed some interesting MHD features. The CT injection played an important role for suppressing $m = 4$ to $m = 3$ MHD modes during the induced H-mode-like phase. During the suppression phase, the MHD fluctuations were greatly

reduced to near the noise level and the rotating frequency was also reduced from 32.5 kHz to 25 kHz. However, at 1 ms after CT injection, the suppression phase was terminated by a non-traveling $m = 1$ gong mode followed by a propagating $m = 2$ mode. It is not completely understood if the gong mode is a precursor for H-L back transition. Nevertheless, it is well documented that the gong mode is the magnetic signature of sawtooth crashes observed outside the plasma. In the Tore Supra tokamak, the spatial structure of the gong burst was reported at values consistent with the integer of the q-factor in the plasma edge region. In STOR-M, the gong is expected to exist near the $q = 1$ surface, similar to some gongs observed in the JET tokamak.

Another type of magnetic perturbation with strong amplitude modifications was observed during a normal discharge in STOR-M. This magnetic perturbation was identified as a (2, 1) island oscillating at a frequency about 23 kHz. In addition, sawtooth oscillations associated with the (1, 1) magnetic island on the $q = 1$ surface were observed by SXR arrays. During the sawtooth-free phase the fluctuations in Mirnov signals and the SXR emission intensity were highly coherent at a dominant frequency of 23 kHz.

7.2 Future Work

The STOR-M tokamak is now equipped with Mirnov coil arrays and SXR detector arrays that will facilitate the investigation of MHD instabilities in future experiments. The data processing techniques were tested on artificial data set and successfully applied to the experimental data. It is planned to install supplementary Mirnov arrays inside the vacuum chamber to avoid phase distortion caused by the chamber wall. More toroidal coils may be required to enhance the spatial resolution for the toroidal mode. Also, further studies are planned to use SXR system to study the radial structure of magnetic islands using some tomographic reconstruction algorithms and other techniques.

The gong mode was studied using a single poloidal array in an early experiment. Its behavior along the toroidal direction can now be investigated by all four poloidal arrays at four toroidal locations

at the same time. It is important to integrate the SXR system into any further study since some localized perturbations near (1, 1) surface, known as the snake-like instability [109], can be observed. Features of MHD fluctuations under various experimental conditions, such as CT injection, TH current pulse, and electrode biasing, should be carried out to reveal the relationships between the MHD instabilities and various improved confinement regimes. Finally, a current through a set of helical coils with a selected (m, n) rotation will be used to induce an externally applied magnetic field. This additional magnetic field will interact with the magnetic islands with the same (m, n) structure in the plasma. It is possible that this resonant interaction will suppress the target MHD instabilities and improve the confinement [110]. The MHD monitoring hardware and analysis techniques developed during this M.Sc. research project will be very useful for this planned helical coil experiment.

Appendix A - SVD Example

The following example shows how the SVD algorithm decomposes any data matrix $\mathbf{A}_{MN}$ into three matrices $\mathbf{U}_{MM}\mathbf{S}_{MN}\mathbf{V}^T_{NN}$ by calculating the corresponding eigenvalues and eigenvectors of $\mathbf{A}\mathbf{A}^T$ and $\mathbf{A}^T\mathbf{A}$. Starting from a small matrix $\mathbf{A}$ and its transpose $\mathbf{A}^T$

$$\mathbf{A} = \begin{pmatrix} 3 & 1 & 1 \\ -1 & 3 & 1 \end{pmatrix} \qquad \mathbf{A}^T = \begin{pmatrix} 3 & -1 \\ 1 & 3 \\ 1 & 1 \end{pmatrix}$$

the elements of matrix $\mathbf{U}$ can be evaluated from solving the eigenspace of $\mathbf{A}\mathbf{A}^T$:

$$\mathbf{A}\mathbf{A}^T = \begin{pmatrix} 3 & 1 & 1 \\ -1 & 3 & 1 \end{pmatrix} \cdot \begin{pmatrix} 3 & -1 \\ 1 & 3 \\ 1 & 1 \end{pmatrix} = \begin{pmatrix} 11 & 1 \\ 1 & 11 \end{pmatrix}$$

The eigenvalues λ of $\mathbf{A}\mathbf{A}^T$ are calculated from solving the general eigenvector equation:

$$\left(\mathbf{A}\mathbf{A}^T\right)\mathbf{x} = \lambda\mathbf{x} \quad \Longrightarrow \quad \begin{pmatrix} 11 & 1 \\ 1 & 11 \end{pmatrix} \cdot \begin{pmatrix} x_1 \\ x_2 \end{pmatrix} = \lambda \begin{pmatrix} x_1 \\ x_2 \end{pmatrix}$$

which gives a set of eigenvector equations:

$$(11 - \lambda)x_1 + x_2 = 0$$

$$x_1 + (11 - \lambda)x_2 = 0$$

Setting the determinant of the coefficient matrix to 0

$$\begin{vmatrix} (11-\lambda) & 1 \\ 1 & (11-\lambda) \end{vmatrix} = 0$$

yields two solutions for λ, 12 and 10. Substituting the eigenvalue $\lambda = 12$ back into the eigenvector equations and solving for $x_1 = 1$ produces the first eigenvector $\boldsymbol{a}_1 = [1, 1]$. The second eigenvector $\boldsymbol{a}_2 = [1, -1]$ is evaluated similarly from the eigenvalue $\lambda = 10$ and unitary value $x_1 = 1$. The column vectors of the $\mathbf{U}$ matrix are simply the normalized eigenvectors of $\mathbf{A}\mathbf{A}^T$:

$$\mathbf{U} = \begin{pmatrix} \frac{\boldsymbol{a}_1}{|\boldsymbol{a}_1|} & \frac{\boldsymbol{a}_2}{|\boldsymbol{a}_2|} \end{pmatrix} = \begin{pmatrix} \frac{1}{\sqrt{2}} & \frac{1}{\sqrt{2}} \\ \frac{1}{\sqrt{2}} & -\frac{1}{\sqrt{2}} \end{pmatrix}$$

The $\mathbf{V}$ matrix can be constructed by solving the eigenspace of $\mathbf{A}^T\mathbf{A}$:

$$\mathbf{A}^T\mathbf{A} = \begin{pmatrix} 3 & -1 \\ 1 & 3 \\ 1 & 1 \end{pmatrix} \cdot \begin{pmatrix} 3 & 1 & 1 \\ -1 & 3 & 1 \end{pmatrix} = \begin{pmatrix} 10 & 0 & 2 \\ 0 & 10 & 4 \\ 2 & 4 & 2 \end{pmatrix}$$

The following eigenvector equation

$$\left(\mathbf{A}^T\mathbf{A}\right)\mathbf{x} = \lambda\mathbf{x} \quad \Longrightarrow \quad \begin{pmatrix} 10 & 0 & 2 \\ 0 & 10 & 4 \\ 2 & 4 & 2 \end{pmatrix} \cdot \begin{pmatrix} x_1 \\ x_2 \\ x_3 \end{pmatrix} = \lambda \begin{pmatrix} x_1 \\ x_2 \\ x_3 \end{pmatrix}$$

generates a system of equations with three variables x_1, x_2 and x_3:

$$(10-\lambda)x_1 + 2x_3 = 0$$

$$(10-\lambda)x_2 + 2x_3 = 0$$

$$2x_1 + 4x_2 + (2-\lambda)x_3 = 0$$

Setting the determinant to 0 and solving for λ

$$\begin{vmatrix} (10-\lambda) & 0 & 2 \\ 0 & (10-\lambda) & 4 \\ 2 & 4 & (2-\lambda) \end{vmatrix} = 0$$

provides three eigenvalues with values of 12, 10 and 0. The eigenvectors of $\mathbf{A}^T\mathbf{A}$, $\boldsymbol{b}_1 = [1, 2, 1]$, $\boldsymbol{b}_2 = [2, -1, 0]$ and $\boldsymbol{b}_3 = [1, 2, -5]$, are computed respectively from the eigenvalues $\lambda = 12$, 10 and 0. The column vectors of the $\mathbf{V}$ matrix are the normalized eigenvectors of $\mathbf{A}^T\mathbf{A}$ which are arranged relative to the eigenvalues from the largest to the smallest:

$$\mathbf{V} = \begin{pmatrix} \frac{\boldsymbol{b}_1}{|\boldsymbol{b}_1|} & \frac{\boldsymbol{b}_2}{|\boldsymbol{b}_2|} & \frac{\boldsymbol{b}_3}{|\boldsymbol{b}_3|} \end{pmatrix} = \begin{pmatrix} \frac{1}{\sqrt{6}} & \frac{2}{\sqrt{5}} & \frac{1}{\sqrt{30}} \\ \frac{2}{\sqrt{6}} & -\frac{1}{\sqrt{5}} & \frac{2}{\sqrt{30}} \\ \frac{1}{\sqrt{6}} & 0 & -\frac{5}{\sqrt{30}} \end{pmatrix}$$

The matrix $\mathbf{S}$ is constructed by taking the square root of non-zero eigenvalues of $\mathbf{A}\mathbf{A}^T$ and $\mathbf{A}^T\mathbf{A}$ ($\lambda = 12$ and 10) and arranging them along the diagonal in descending order. Note that the matrix $\mathbf{S}$ has the same size of matrix $\mathbf{A}$:

$$\mathbf{S} = \begin{pmatrix} \sqrt{12} & 0 & 0 \\ 0 & \sqrt{10} & 0 \end{pmatrix}$$

The original matrix $\mathbf{A}$ can be recovered by multiplying the $\mathbf{U}$, $\mathbf{S}$ and $\mathbf{V}^T$ matrices:

$$\begin{pmatrix} \frac{1}{\sqrt{2}} & \frac{1}{\sqrt{2}} \\ \frac{1}{\sqrt{2}} & -\frac{1}{\sqrt{2}} \end{pmatrix} \cdot \begin{pmatrix} \sqrt{12} & 0 & 0 \\ 0 & \sqrt{10} & 0 \end{pmatrix} \cdot \begin{pmatrix} \frac{1}{\sqrt{6}} & \frac{2}{\sqrt{6}} & \frac{1}{\sqrt{6}} \\ \frac{2}{\sqrt{5}} & -\frac{1}{\sqrt{5}} & 0 \\ \frac{1}{\sqrt{30}} & \frac{2}{\sqrt{30}} & -\frac{5}{\sqrt{30}} \end{pmatrix} = \begin{pmatrix} 3 & 1 & 1 \\ -1 & 3 & 1 \end{pmatrix} = \mathbf{A}$$

Appendix B - Useful MATLAB Commands

Command	Description
`abs`	Absolute value and complex magnitude
`angle`	Phase angle of complex number
`atan`	Inverse tangent
`atan2`	Four-quadrant inverse tangent
`axis`	Axis scaling and limiting
`bar`	Plots bar chart (vertical and horizontal)
`centfrq`	Wavelet central frequency
`chirp`	Generates swept-frequency cosine (chirp) signal
`cmor`	Complex Morlet wavelet
`colorbar`	Colorbar showing color scale
`colormap`	Sets and recalls current colormap
`conj`	Complex conjugate
`contour`	Contour plot of matrix
`contourf`	Filled 2-D contour plot
`cross`	Vector cross product
`cwt`	Real or complex continuous 1-D wavelet coefficient
`cyl3d` [111]	Plots 3-D data on cylindrical surface
`deg2rad`	Converts angle from degrees to radians
`det`	Matrix determinant
`diag`	Main diagonal of matrix
`dot`	Vector dot product
`eig`	Computes eigenvalues and eigenvectors of matrix
`errorbar`	Plots error bars along curve
`exp`	Exponential function
`eye`	Identity matrix
`fft`	1-D fast Fourier transform
`ifft`	1-D inverse fast Fourier transform

`imag`	Imaginary part of complex number
`imagesc`	Scales data and displays image object
`lighting`	Specifies lighting algorithm
`log`	Natural logarithm
`log10`	Common (base 10) logarithm
`loglog`	Log-log scale plot
`max`	Largest elements in matrix
`mean`	Average or mean value of matrix
`min`	Smallest elements in matrix
`morl`	Morlet wavelet
`pcolor`	Pseudo-color plot
`plot`	2-D line plot
`plotyy`	2-D line plots with y-axes on both left and right side
`polar`	Polar coordinate plot
`rad2deg`	Converts angle from radians to degrees
`rand`	Generates uniformly distributed random numbers in the interval (0, 1)
`real`	Real part of complex number
`reshape`	Changes size of matrix
`round`	Rounds towards the nearest integer
`sawtooth`	Generates sawtooth or triangle wave
`scal2frq`	Converts wavelet scale to frequency
`shading`	Sets color shading properties
`size`	Returns the dimensions of matrix
`spectrogram`	Spectrogram using short-time Fourier transform
`sqrt`	Square root
`stem`	Plots discrete sequence data
`subplot`	Creates plots in subwindows
`sum`	Sum of matrix elements
`surf`	3-D shaded surface plot
`surfc`	3-D shaded surface plot with contour plot underneath
`svd`	Singular value decomposition
`transpose`	Interchanges the rows and columns of matrix
`waveinfo`	Wavelets information
`wrapTo360`	Wraps angle in degrees to [0 360]
`wrapTo2Pi`	Wraps angle in radians to [0 2π]
`xcorr`	Computes cross-correlation and auto-correlation

Bibliography

[1] Christof Rühl, *Energy in Perspective*, BP Statistical Review of World Energy (2007).

[2] R. A. Gross, *Fusion Energy*, A Wiley-Interscience Publication (1984).

[3] J. Freidberg, *Plasma Physics and Fusion Energy*, MIT Press, Cambridge, MA (2007).

[4] A. Dinklage, T. Klinger, G. Marx and L. Schweikhard, *Plasma Physics: Confinment, Transport and Collective Effects*, Springer, Heidelberg (2005).

[5] F. F. Cap, *Handbook on Plasma Instabilities: Volume 1*, Academic Press (1976).

[6] K. Miyamoto, *Controlled Fusion and Plasma Physics*, Tylor and Francis (2007).

[7] K. Niu, *Nuclear Fusion*, Cambridge University Press (1979).

[8] J. G. Cordey, R. J. Goldston and R. R. Parker, *Magnetic Fusion Progress Toward a Tokamak Fusion Reactor*, Physics Today, 22 (1992).

[9] J. k. Leung, *Star Makers*, Department of Physics, University of Hong Kong, http://resources.edb.gov.hk/physics/articleIE/starmaker/starMaker_e.htm.

[10] J. D. Lawson, Proc. Phys. Soc. **B70**, 6 (1957).

[11] J. Wesson, *Tokamaks 3rd Ed*, Clarendon Press (2004).

[12] A. A. Harms, K. F. Schoept, G. H. Miley and D. R. Kingdon, *Principles of Fusion Energy*, World Scientific Publishing (2000).

[13] D. G. Lominadze, *Cyclotron Waves in Plasma*, Pergamon Press (1981).

[14] F. F. Chen, *Introduction to Plasma Physics and Controlled Fusion 2nd Ed*, Plenum Press (1984).

[15] A. L. Bezbatchenko, I. N. Golovin, P. I. Kozlov, A. S. Strelkov and I. Yavlinsky, *Plasma Physics and Problems of Controlled Fusion 1*, 116 (1955).

[16] K. Miyamoto, *Fundamentals of Plasma Physics and Controlled Fusion*, Iwanami Book Service Center, Tokyo (1997).

[17] F. F. Chen, *Plasma Physics and Controlled Fusion 1st Ed*, Plenum Press (1974).

[18] O. Mitarai, S. W. Wolfe, A. Hirose and H. M. Skarsgard, Plasma Phys. Controlled Fusion **27**, 395 (1985).

[19] *Progress Report 1995/96*, Plasma Physics Laboratory, University of Saskatchewan, Saskatoon.

[20] W. Zhang, C. Xiao, G. G. Conway, O. Mitarai, A. Sarkissian, H. M. Skarsgard, L. Zhang and A. Hirose, Phys. Fluids **B4**, 3277 (1992).

[21] W. Zhang, C. Xiao and A. Hirose, Phys. Fluids **B5**, 3961 (1993).

[22] O. Mitarai, H. M. Skarsgard and A. Hirose, Fusion Tech **20**, 285 (1991).

[23] S. Sen, C. Xiao, A. Hirose and R.A. Cairns, Phys. Rev. Lett. **88**, 185001 (2002).

[24] D. Liu, *Ph.D. Thesis*, University of Saskatchewan, Saskatoon (2006).

[25] A. Hirose, C. Xiao, O. Mitarai, J. E. Morelli and H. Skarsgard, Physics in Canada (2006).

[26] *TMP/NT 1000 Turbomolecular Pump and Frequency Converter Manual*, Leybold-Heraeus Vacuum Products Inc., Part No. 722-78-018 Edition C, 313B.

[27] *Precision Leak Valve PV-10 Operation and Maintenance*, Veeco Instruments Inc., 287.

[28] *Automatic Pressure Controllers APC-1000 APC-2000 Operation and Maintenance Manual*, Veeco Instruments Inc., Part No. 8290-800, 287.

[29] J. B. Taylor, Rev. Mod. Phys **58-3**, 741 (1986).

[30] W. Zhang, *Ph.D. Thesis*, University of Saskatchewan, Saskatoon (1993).

[31] J. D. Jackson, *Classical Electrodynamics 3rd Ed*, John Wiley and Sons Inc. (1999).

[32] S. J. Livingstone, *M.Sc. Thesis*, University of Saskatchewan, Saskatoon (2005).

[33] J. E. Morelli, *Ph.D. Thesis*, University of Saskatchewan, Saskatoon (2003).

[34] E. Teller, *Fusion, Magnetic Confinement: Volume 1*, Academic Press, New York (1981).

[35] L. Spitzer Jr., *Physics of Fully Ionized Gases*, Interscience, New York (1956).

[36] M. E. Khonsaari, *Ph.D. Thesis*, University of Saskatchewan, Saskatoon (1990).

[37] G. St. Germaine, *M.Sc. Thesis*, University of Saskatchewan, Saskatoon (2006).

[38] V. S. Mukhovatov and V. D. Shafranov, Nuclear Fusion **11**, 605 (1971).

[39] H. Ninomiya and N. Suzuki, Japanese Journal of Applied Physics **21-9**, 1323 (1982).

[40] K. A. Razumova, Atomn. Energ. **20**, 459 (1966).

[41] M. Haegi and F. Sand. Plasma Physics **17**, 997 (1975).

[42] B. D. Scott, *An Introduction to Magnetohydrodynamics (MHD), or Magnetic Fluid Dynamics*, Lect. Notes Phys. **670**, 51 (2005).

[43] R. J. Goldston and P. H. Rutherford, *Introduction to Plasma Physics*, IOP Publishing Ltd. (1995).

[44] A. Fridman and L. A. Kennedy, *Plasma Physics and Engineering*, Tylor and Francis (2004).

[45] P. M. Bellan, *Fundamentals of Plasma Physics*, Cambridge University Press (2006).

[46] D. A. Gurnett and A. Bhattacharjee, *Introduction to Plasma Physics with Space and Laboratory Applications*, Cambridge University Press (2005).

[47] A. Hirose, *Plasma Waves 1*, Lecture Notes, University of Saskatchewan, Saskatoon (2007).

[48] K. Miyamoto, *Plasma Physics for Nuclear Fusion*, MIT Press (1987).

[49] A. I. Morozov and L. S. Solovev, *The Structure of Magnetic Fields, In Reviews of Plasma Physics 2*, Consultants Bureau New York (1966).

[50] G. Bateman, *MHD Instabilities*, MIT Press, Cambridge, MA (1978).

[51] H. Zohm, Conference Digest of the 2004 Joint 29th International Conference on Infrared and Millimeter Waves and 12th International Conference on Terahertz Electronics **Tu3.1**, 217 (2004).

[52] A. Jeffrey and T. Taniuti, *Magnetohydrodynamic Stability and Thermonuclear Containment*, Academic Press (1966).

[53] V. E. Golant, A. P. Zhilinsky and I. E. Sakharov, *Fundamentals of Plasma Physics*, John Wiley and Sons Inc. (1980).

[54] A. Sarkissian, A. Hirose, W. Zhang *et al.*, Can. J. Phys. **68**, 369 (1990).

[55] R. D. Hazeltine and J. D. Meiss, *Plasma Confinement*, Addison-Wesley Publishing Company (1992).

[56] S. V. Mirnov and I. B. Semenov, At. Energ., USSR **30**, 20 (1971).

[57] W. M. Manheimer and C. N. Lashmore-Davies, *MHD and Microinstabilities in Confined Plasma*, IOP Publishing Ltd. (1989).

[58] S. Von Goeler, W. Stodiek and N. Sauthoff, Phys. Rev. Lett. **33**, 1201 (1974).

[59] D. Biskamp, *Nonlinear Magnetohydrondynamics*, Cambridge University Press (1993).

[60] P. V. Savrukhin, N. L. Vasin, A. A. Bagdasarov and K. N. Tarasyan, Plasma Physics and Controlled Fusion **33-11**, 1341 (1991).

[61] E. Oran Brigham, *Fast Fourier Transform and Its Applications*, Prentice Hall Signal Processing Series (1988).

[62] D. C. Champeney, *Fourier Transforms and Their Physical Applications*, Academic Press (1973).

[63] A. D. Poularikas, *The Transforms and Applications Handbook 2nd Ed*, CRC and IEEE Press (2000).

[64] J. O. Smith III, *Mathematics of the Discrete Fourier Transform: with Audio Applications 2nd Ed*, BookSurge Publishing (2007).

[65] J. W. Cooley and J. W. Tukey, Math. Comput. **19**, 297 (1965).

[66] M. Akay, *Time Frequency and Wavelets in Biomedical Signal Processing*, IEEE Press (1998).

[67] A. V. Oppenheim and R. W. Schafer, *Discrete-Time Signal Processing*, Prentice-Hall Inc. (1989).

[68] S. M. Kuo and W. Gan, *Digital Signal Processors: Architectures, Implementations and Applications*, Pearson Prentice Hall (2005).

[69] B. Vidakovic, *Statistical Modeling by Wavelets*, John Wiley and Sons Inc. (1999).

[70] A. Teolis, *Computational Signal Processing with Wavelets*, Birkhäuser, Boston (1998).

[71] P. Goupillaud, A. Grossmann and J. Morlet, Geoexploration **23**, 85 (1984).

[72] R. Polikar, *The Enginner's Ultimate Guide to Wavelet Analysis: The Wavelet Tutorial*, Rowan University, College of Engineering (2001).

[73] J. S. Bendat and A. G. Piersol, *Engineering Applications of Correlation and Spectral Analysis 2nd Ed*, John Wiley and Sons Inc. (1993).

[74] D. E. Smith, E. J. Powers and G. S. Caldwell, IEEE Transactions on Plasma Science **PS-2**, 261 (1974).

[75] G. Bachman, L. Narici and E. Beckenstein, *Fourier and Wavelet Analysis*, Springer-Verlag New York Inc. (2000).

[76] P. A. Duperrex, A. Pochelon, A. W. Edwards and J. A. Snipes, Nuclear Fusion **32**, 1161 (1992).

[77] D. Del-Castillo-Negrete, S. P. Hirshman, D. A. Spong and E. F. D'Azevedo, Journal of Computational Physics **222**, 265 (2007).

[78] W. H. Press, B. P. Flannery, S. A. Teukolsky and W. T. Vetterling, *Numerical Recipes in C: The Art of Scientific Computing 2nd Ed*, Cambridge University Press (1993).

[79] P. O. Persson, *Introduction to Numerical Methods*, Lecture Notes, MIT (2006).

[80] J. S. Kim, D. H. Edgell, J. M. Greene, E. J. Strait and M. S. Chance, Plasma Phys. Control. Fusion **41**, 1399 (1999).

[81] S. Ohdachi, K. Toi, G. Fuchs and LHD Experimental Group, 30th EPS Conference on Controlled Fusion and Plasma Physics, St. Petersburg, Russia (2003).

[82] D. S. Broomhead and G. P. King, Physica D **20**, 217 (1986).

[83] C. Nardone, Plasma Phys. Control. Fusion **34**, 1447 (1992).

[84] I. H. Hutchinson, *Principles of Plasma Diagnostics 2nd Ed*, Cambridge University Press (2002).

[85] C. Xiao, *Plasma Transport and Diagnostic Techniques*, Lecture Notes, University of Saskatchewan, Saskatoon (2007).

[86] W. E. Han, A. Thyagaraja, S. J. Fielding and M. Valovic, Plasma Phys. Control. Fusion **42**, 181 (2000).

[87] *Data Sheet of National Instuments Digitizer Card*, Model No. NI PXI-6133, http://sine.ni.com/nips/cds/view/p/lang/en/nid/14110.

[88] *Data Sheet of BK Precision LCR meter*, Model No. 879, http://www.testequipmentdepot.com/bk-precision/lcr/879.htm.

[89] N. Ida, *Engineering Electromagetics 2nd Ed*, Springer-Verlag New York, LLC (2004).

[90] H. L. Berk, J. W. Van Dam, Z. Guo and D. M. Lindberg, Phys. Fluids **B4**, 1806 (1992).

[91] D. Griffiths, *Introduction to Electrodynamics 3rd Ed*, Prentice-Hall Inc. (1999).

[92] C. Xiao, T. Niu, J. E. Morelli, C. Paz-Soldan, M. Dreval, S. Elgriw, A. Pant, D. Rohraff, D. Trembach and A. Hirose, Rev. Sci. Instrum. **79**, 10E926 (2008).

[93] O. Kluber, H. Zohm, H. Bruhns, J. Gernhardt, K. Kallenbach and H. P. Zehrfeld, Nuclear Fusion **31**, 907 (1991).

[94] M. N. Bussac, D. Edery, R. Pellat and J. L. Soule, IAEA Vienna **1**, 607 (1977).

[95] H. Zohm, J. Greene, L. Lao and E. Strait, *General Atomic Report*, GA-A20886 (1992).

[96] D. Raju, R. Jha, P. K. Kaw, S. K. Mattoo, Y. C. Saxena and Aditya Team, Pramana **55**, 5 (2000).

[97] D. W. Guillaume, Rev. Sci. Instrum. **73**, 98 (2002).

[98] J. S. Kim, M. S. Chance, D. H. Edgell, J. M. Greene, E. J. Strait and A. D. Turnbull, Plasma Phys. Control. Fusion **43**, 1593 (2001).

[99] C. Xiao, A. Hirose and S. Sen, Phys. Plasmas **11**, 4041 (2004).

[100] F. Wagner, G. Becker, K. Behringer *et al.*, Phys. Rev. Lett. **49**, 1408 (1982).

[101] D. Liu, C. Xiao, A. Singh and A. Hirose, 20th IAEA Fusion Energy Conference, FT/**P6-38** (2004).

[102] C. Xiao, S. J. Livingstone, A. K. Singh, D. Raju, G. St. Germaine, D. Liu, C. Boucher and A. Hirose, 21st IAEA Fusion Energy Conference, EX/**P4-31** (2006).

[103] P. A. Duperrex, R. Keller, A. Pochelon and G. Tonetti, Helv. Phys. Acta **58**, 85 (1985).

[104] A. Hirose, M. Dreval, S. Elgriw, O. Mitarai, A. Pant, M. Peng, D. Rohraff, A. K. Singh, D. Trembach and C. Xiao, 17th IAEA Technical Meeting on Research Using Small Fusion Devices, AIP Conference Proceedings Series **996**, 14 (2008).

[105] C. Xiao, S. Elgriw, M. Dreval, T. Niu, A. Pant, D. Rohraff, A. Singh, D. Trembach, A. Hirose, 22nd IAEA Fusion Energy Conference, EX/**P9-3** (2008).

[106] T. Dudok de Wit, R. Lima, A. L. Pecquet and J. C. Vallet, Phys. Plasmas **1**, 3288 (1994).

[107] M. Dreval, C. Xiao, D. Trembach, A. Hirose, S. Elgriw, A. Pant, D. Rohraff and T. Niu, Plasma Phys. Control. Fusion **50**, 095014 (2008).

[108] V. A. Kornev, L. G. Askinazi, M. I. Vildzhyunas *et al.*, Plasma Physics Reports **31**, 803 (2005).

[109] Y. B. Dong, C. H. Pan, Y. Liu and B. Z. Fu, Plasma Sci. Technol. **6**, 2307 (2004).

[110] F. Karger, H. Wobig, S. Corti *et al.*, IAEA Proc. 5th Int. Conf. on Plasma Physics and Controlled Nuclear Fusion Energy Research **1**, 207 (1974).

[111] J. M. De Freitas, QinetiQ Ltd, Winfrith Technology Centre, Winfrith, Dorchester, UK (2005).